SAPIENZA
UNIVERSITÀ DI ROMA

Fundamental Physics with the Galileo FOC satellites and the G4S_2.0 project

Physics Department
PhD in Astronomy, Astrophysics and Space Science (XXXVI cycle)

Feliciana Sapio
ID number 1949483

Advisor
Dr. David Lucchesi

Co-Advisor
Dr. Massimo Visco
Prof. Giuseppe Pucacco

Academic Year 2022/2023

Thesis defended on 5 April 2024
in front of a Board of Examiners composed by:

Prof. Francesco Piacentini, University of Roma Sapienza (chairman)

Prof. Stefano Borgani, University of Trieste

Prof. Salvatore Capozziello, University of Napoli Federico II

Prof. Francesco Rosario Ferraro, University of Bologna

Fundamental Physics with the Galileo FOC satellites and the G4S_2.0 project
Sapienza University of Rome

This thesis has been typeset by LaTeX and the Sapthesis class.

Author's email: feliciana.sapio@uniroma1.it, feliciana.sapio@inaf.it

Abstract

This Thesis has been developed within the Galileo for Science Project (G4S_2.0) since its beginning in 2021. The G4S_2.0 is an ongoing project developed under the auspices of the Italian Space Agency (ASI) in collaboration with the National Institute for Astrophysics (INAF) and Politecnico di Torino. The project has several goals in the field of Fundamental Physics by exploiting the Global Navigation Satellite System (GNSS) Galileo, in particular the Full Operational Capability (FOC) Constellation.

The relatively high eccentricity ($\simeq 0.16$) of the two FOC in elliptical orbits, GSAT0201 and GSAT0202, and the accuracy of their atomic clocks allow to measure the gravitational redshift and the relativistic precessions of the orbits. Furthermore, the analysis of the atomic clock data of the entire Galileo FOC constellation also allows us to probe the presence of Domain Wall (DW) Dark matter in the Milky Way and to place severe constraints on their interaction with ordinary matter.

This work outlines the state of the art of the G4S_2.0 activities necessary for the gravitational redshift and the relativistic precessions measurements and for Dark Matter constraints. For all these measurements, a fundamental point is to obtain a suitable satellite orbit solution by performing an accurate Precise Orbit Determination (POD) with a reliable estimate of the clock-bias of the on board atomic clocks. This work presents the efforts to achieve this, starting with the development of a dynamical model to account for the complex effects of the non-gravitational perturbations, in particular those related to the direct solar radiation pressure, and performing dedicated PODs to test our results. Based on the PODs results, we requested a dedicated Satellite Laser Ranging campaign to the International Laser Ranging Service to improve the available number of laser observations, given their importance for some of the G4S_2.0 measurements. Regarding Dark Matter constraints, this work describes the strategy adopted to analyse the on-board atomic clock data, stressing the original statistical approach: a physical simulation pipeline is developed to simulate the interaction between a set of Galileo FOC satellites and a DW, allowing the study of the detection efficiency of the considered clock-network.

Finally, we present our reflections and prospects for the future.

Acknowledgments

This work is part of the G4S_2.0 project, developed under the auspices of the Italian Space Agency (ASI) within the frame of the Bando Premiale CI-COT-2018-085 with the co-participation of the Italian Institute for Astrophysics (INAF) and the Politecnico di Torino (POLITO). The scientific research carried out for the project is supported under the Accordo Attuativo No. 2021-14-HH.0. Special thanks go to ASI, in particular to Dr. Francesco Vespe (ASI-CGS), who financed this project.

I would like to express my deepest gratitude to my supervisors, in particular Dr. David Lucchesi (IAPS-INAF) and Dr. Massimo Visco (IAPS-INAF) for their invaluable advice and continuous support. I am grateful for their care and attention to me and the benefit of their in-depth knowledge and experience in scientific research. Thanks to Prof. Giuseppe Pucacco (University of Rome Tor Vergata) for his collaboration and his precious advice during the Thesis preparation.

Thanks to all the members of the G4S_2.0 project for introducing me to the various aspects of the project and for the rich exchange of information and ideas. I would like to acknowledge Dr. Alessandro Di Marco (IAPS-INAF) for his continuous support and for the fruitful discussions on Cosmology and Fundamental Physics. I also received a special attention during the Thesis work from Dr. Marco Cinelli, Ing. Carlo Lefevre, Ing. Carmelo Magnafico and Dr. Roberto Peron.

Many thanks to Dr. Josè Rodriguez (Geodetic Infrastructure Network, National Geographic Institute, Spain) and Dr. Ing. Benny Rievers (Space Science Department, University of Bremen, Germany) that reviewed this Thesis for their appreciation of this work and for their comments and suggestions.

I would like to acknowledge the International Laser Ranging Service Central Bureau for supporting the project objectives through a dedicated satellite laser ranging campaign and for providing high-quality laser ranging data of Galileo satellites. Special thanks to Mike Pearlman (Center for Astrophysics, Cambridge, MA, USA).

Finally, I would like to thank my husband Gianmarco for his love and strong encouragement in this work. Special thanks go to all my family, especially my parents and my brother. Their presence and love have been a source of motivation and support for me throughout these years.

Feliciana Sapio

Scientific publications related to the Thesis

- F. Sapio, D. M. Lucchesi, M. Visco, S. Benedetti, E. Fiorenza, C. Lefevre, M. Lucente, C. Magnafico, R. Peron and F. Santoli, *The Galileo for Science (G4S_2.0) project: Fundamental Physics experiments with Galileo satellites DORESA and MILENA*, Nuovo Cimento C 45, 152 (2022).
- A. Di Marco, F. Sapio, M. Cinelli, E. Fiorenza, C. Lefevre, P. Loffredo, D. M. Lucchesi, M. Lucente, C. Magnafico, R. Peron, F. Santoli, M. Visco, *The Galileo for Science (G4S 2.0) project: Measurement of the Gravitational Redshift with the Galileo satellites DORESA and MILENA*, Nuovo Cimento 46 C, 116 (2023).
- D. Lucchesi, M. Visco, C. Lefevre, M. Lucente, F. Santoli, F. Sapio, M. Cinelli, A. Di Marco, E. Fiorenza, P. Loffredo, C. Magnafico, R. Peron and F. Vespe, *Fundamental Physics measurements with Galileo FOC satellites and the Galileo for Science project. Part I: a 3D-CAD and a Box Wing for modeling the effects of Non-Conservative Forces*, Phys. Rev. D., 109, 062004 (2024).
- F. Sapio, D. Lucchesi, M. Visco, R. Peron, M. Lucente, C. Lefevre, M. Cinelli, A. Di Marco, E. Fiorenza, P. Loffredo, C. Magnafico, F. Santoli and F. Vespe: *Fundamental Physics measurements with Galileo FOC satellites and the Galileo for Science project. Part II: a Box Wing for modeling Direct Solar Radiation Pressure and preliminaries Orbit Determinations*, Phys. Rev. D., 109, 062005 (2024).

Contents

Chapter 1

Introduction

The theory of General Relativity (GR) [1] is currently considered a pillar of our understanding of the Universe.

The essence of the theory is that gravity is a manifestation of the curvature of space-time. Its relationship to the mass-energy content is explained by Einstein's field equations. The foundation is the Einstein Equivalence Principle (EEP) which is based on (i) the Universality of Free Fall (UFF) also known as Weak Equivalence Principle (WEP), (ii) the Local Lorentz Invariance (LLI), and (iii) the Local Position Invariance (LPI).

The so-called "three crucial tests" are usually cited as experimental verifications of the theory: the gravitational redshift of light, the light deflection in gravitational fields, the precession of the perihelion of Mercury's orbit. However, in 1960 Schiff [2] derived the first two effects from the Weak Equivalence Principle and Special Relativity whereas only the latter from Einstein's field equations. Therefore, he concluded that only the planetary orbit precession provides a real test of GR.

Nevertheless, GR has passed a large number of experimental tests [3,4]. Most recently, the detection of gravitational waves [5] and the direct observation of the black hole's shadow [6,7] also have confirmed the predictions of GR.

However, a large number of particles, astrophysical and cosmological observations have led part of the scientific community to believe that GR would suffer from a number of shortcomings at infrared and ultraviolet scales. For these reasons, extended and alternative theories of gravity have been proposed over the years [8,9]. On the other side, it is also possible that more (unexplored) general solutions of GR could explain most of the observations, as discussed in [10].

It is therefore clear how important it is to test the predictions of GR against the other proposed theories in order to get the best interpretation of the gravitational interaction. This possibility poses an enormous challenge, leading the scientific community to develop new experiments and strategies to directly test GR as well as its fundamental assumptions. In principle, testing the validity of some of these assumptions does not represent a truly test of GR, as anticipated above. However, it is equally important in order to catch possible physics beyond both the Standard Model of particle physics and gravity.

In this direction, testing the EEP can be useful to derive information about GR fundamentals. This can be performed by testing its three aspects: the UFF, the LLI and the LPI.

In particular, the LPI can be tested by looking for variations in fundamental constants or by constraining the gravitational redshift (GRS) [4]. Predicted by Einstein in 1907 [11], the GRS was definitively verified with the Pound and Rebka experiment in 1959 [12] and Snider [13]. The development of new technologies such as atomic clocks has allowed to perform more accurate GRS measurements, such as the one obtained with the Gravity Probe A (GP-A) rocket experiment in 1976 [14,15].

A few years ago, two satellites of the European Global Navigation Satellite System (GNSS) Galileo, offered to the scientific community the possibility of improving the GP-A measurement. In particular, two Galileo satellites (GSAT0201 and GSAT0202, also called "Doresa" and "Milena") were erroneously injected into orbits with a higher eccentricity with respect to the other satellites of the constellation. The elliptic orbit, due to the variation of the gravitational field, induces a periodic modulation of the onboard atomic clocks frequency with respect to on-ground clocks. The good clocks stability (about 10^{-14} at the time scale of the orbital period of the satellites, 46584 s)

allows to test this periodic modulation to a new level of uncertainty [16,17]. Indeed, the clock-data of these two satellites have already been used in 2018 by the GREAT (Galileo gravitational Redshift Experiment with eccentric sATellites) project, providing a new measurement of the GRS and improving the GP-A result [18,19].

The Galileo for Science project (G4S_2.0), funded by the Italian Space Agency (ASI) [20] was designed to further improve the GRS test but also to measure, for the first time, the relativistic precessions of Doresa and Milena satellites. This is a great challenge, as these effects predicted by GR are very small for these satellites. The results will be compared with GR predictions, allowing new constraints to be placed on possible alternative and extended theories of gravity [16]. This Thesis has been developed within the activities of the G4S_2.0 project since its inception, developing various aspects.

The science that can be done with GNSS satellites is not limited to these measurements. For example, a constellation of satellites could be used to detect topological Dark Matter, like Domain Wall (DW), as firstly discussed in [21]. In 2017, Roberts et al. applied this proposal to constrain the presence of possible DW Dark Matter by analysing the clocks onboard the satellites of the GPS constellation [22]. The G4S_2.0 aims to do the same but exploiting the Galileo FOC constellation and the higher sensitivity of its onboard atomic clocks [16].

Summarising, the project aims to perform three measurements in the field of Fundamental Physics: i) GRS, which is a LPI test allowing to derive interesting information on GR foundations; ii) relativistic precessions, to test GR predictions with those provided by possible extended and alternative theories of gravity iii) DW Dark Matter constraints, which will allow us to update the constraints on the interaction of non-standard fields with those predicted by the Standard Model. Three Italian research institutes are involved: Center for Space Geodesy (CGS-ASI) in Matera, Istituto di Astrofisica e Planetologia Spaziali (IAPS-INAF) in Roma and Politecnico di Torino (POLITO).

To achieve the ambitious objectives of the project, two efforts are needed: one to analyse the Galileo FOC clock-data and the other to determine their orbits.

Concerning the clock-data, and in view for the future measurement of the GRS with the set of clock-bias determined by G4S_2.0, we have preliminary analysed in-depth the clock-bias of Doresa and Milena satellites provided by GREAT. The goal was to compare them with the GR predictions to constrain, very preliminary, the GRS parameter and test the entire measurement procedure. This activity is ongoing. In fact, we have not yet received detailed information from ESA (European Space Agency) on the relativistic corrections applied to the GREAT clock-bias solution, within the orbit analysis with the `NAPEOS` software [23]. These corrections are necessary for the GRS measurement. Therefore, we plan to a posteriori evaluate these relativistic corrections by exploiting the ESOC (European Space Operations Centre) precise orbits for the GREAT project and taking advantage of the high quality of the `Bernese` software [24]. This particular activity with the `Bernese` is still in progress, and will not be treated in this Thesis.

Relativistic precessions measurements have already been performed with the LAGEOS (LAser GEOdynamic Satellite) satellites [25–28]. The new challenge is to use the Galileo satellites for this purpose. According to GR, these effects are manifested also in the rate of some orbital elements. It is our intention to perform an accurate precise orbit determination (POD) using the `GEODYN II` [29] software in order to extract their measurements from the rate in the orbital residuals.

Improving the POD is not an easy task to achieve with the current state of the art for the Galileo FOC satellites: reliable improvement of the dynamical model and exploiting the laser tracking of the satellites are some of the issues required. Indeed, it is essential to model as well as possible all the perturbations affecting the satellite's orbital elements in order to reveal these tiny relativistic effects. Moreover, to enhance the POD it is possible using not only the microwave tracking-data but also the full-rate Satellite Laser Ranging data (SLR). This explains the main reason that led the G4S_2.0 team to request a dedicated SLR campaign for the Galileo FOC to the International Laser Ranging Service (ILRS) Central Bureau. The results of this campaign will therefore be of extreme importance for the measurements of G4S_2.0 in the field of gravitation.

The development of a reliable dynamical model of the satellite is essential for the aforementioned measurements. The literature proposed several models for non-gravitational perturbations acting on the satellite [30]. In particular, it is of extreme importance to properly take into account

the effects due to the direct solar radiation pressure (SRP), as it is the most relevant contribution. Our goal is to refine the SRP model, in such a way as to take into consideration also minor effects (such as Earth's albedo and Earth's infrared radiation) in our future models [31]. Of course, the proper characterisation of the spacecraft geometry and its complex structure is also important. In this context, our ultimate goal is to build a Finite Element Model (FEM) of a Galileo FOC to capture its complex geometry, characterised by optical and thermal (time-dependent) properties of the surfaces, and its attitude law [30]. Moreover, we intend to use ray-tracing techniques to account for umbra, penumbra and multiple reflections. This Thesis work has contributed to develop a Box-Wing model [31] awaiting to obtain the required information to fully characterise the satellite for the FEM development. As we will see, the results of the model, although preliminary, are positive and encouraging.

About the Dark Matter constraints, it is necessary to consider the whole clock-network of the Galileo FOC constellation to search for a possible signal of DW in clock-data. This signal is characterised by a correlated sequence of delta-like pulses as the DW propagates across the satellite constellation and by a negative delta-like signal, in coincidence in all clock-data, when the reference clock on Earth is invested by the DW [22]. We will see how our approach differs from that in the literature: before performing the measurement, we want to characterise the clock-network from a statistical point of view, *i.e.* how many events our network can detect. Therefore, one of the objectives of this Thesis was the effort to develop a code that realistically simulates the interaction between a DW and the constellation of Galileo FOC satellites with the consequent evaluation of the detection efficiency.

The goals of the G4S_2.0 are various and ambitious: i) the new measurement of the GRS to a new level of uncertainty will be an important outcome in the Experimental Gravitation context; ii) relativistic precessions, here in the weak-field regime, will allow us to study possible deviations from GR and constrain other theories of gravity at a scale different from previous measurements with LAGEOS satellites; iii) the use of the Galileo FOC onboard atomic clock can allow us to explore the intriguing alternative of ultra-light scalar field DWs as Dark Matter. However, in addition to the possible detection of DWs, it also highlights the possibility of using a GNSS constellation as a tool to study the interactions between the fields of the Standard Model of particle physics and those predicted by other theories beyond it.

The Thesis is structured as follows. In Chap.2 we present the GNSS constellation chosen to carry out our measurements, *i.e.* the ESA GNSS Galileo. In particular, we focus on the Galileo FOC satellites describing their structure and components, their physical characteristics and attitude law. In Chap.3, we describe the main perturbations acting on a Galileo FOC satellite and the current state of the art of their modelling. We present our Box-Wing model and the results we obtain for the direct solar radiation pressure, both in terms of perturbing accelerations and in effects on the orbital elements. We will see how our model differs from others in the literature and how our efforts to build a FEM are progressing. In Chap.4, we provide a basic description of the precise orbit determination and the software we currently use for it. We will see our POD results in the orbital residuals and our strategy for extracting the relativistic precessions measurements. We will understand how our Box-Wing model can be used to improve the POD performed with `GEODYN II` and, consequently, the future measurements. Finally, we will explain the reasons for requesting a new dedicated SLR campaign. In Chap.5 we turn our attention to the atomic clocks of the Galileo FOC satellites: the basic operating principle, the signal and the role in the context of Fundamental Physics are explained. In Chap.6 we give an original overview on the cosmological context. In particular we focus on an interesting Dark Matter candidate constituted by ultra-light scalar fields, in particular in the form of Domain Wall. We give an original description of the mathematical framework of these objects and their possible interaction with a GNSS constellation. We will illustrate the way to detect them using the satellites' atomic clock and our investigation strategy. Finally, in Chap.7, we present our conclusions and reflections on the present work, highlighting the activities to be carried out in the near future.

Chapter 2

The ESA GNSS Galileo

In this Chapter we describe the infrastructure of the Galileo satellite constellation. Our focus is on the Galileo FOC satellites, in particular their physical characteristics and attitude law, as they are of interest to us for the G4S_2.0 project measurements. Finally, the Galileo observables and orbit products are explained.

2.1 Galileo infrastructure

Galileo is a Global Navigation Satellite System (GNSS) developed by the European Union, through the European Space Agency (ESA), as an independent alternative to the GPS and GLONASS, the US and Russian GNSS. The system is primarily intended for civilian use, as it can provide real-time position measurements within 1 m[1]. It is characterised by three standard segments [32]:

- The *Space Segment* consists in the satellites constellation. Its main functions regard the generation and the transmission of code and carrier phase signals as well as the storage and the broadcast of the navigation message uploaded by the Ground Segment. The planned Galileo FOC (Full Operational Capability) constellation is based on 27 operational and 3 spare satellites, distributed on 3 orbital planes, equally spaced, inclined at 56° with respect to the Earth's equatorial plane. The orbital altitude is about 23.222 km (Medium Earth Orbit).

- The *Ground Segment* is responsible for the proper operation of the Galileo GNSS. It consists in two Ground-Control Centres (GCC), five Telemetry, Tracking and Control stations (TT&C), nine Mission Uplink Stations (ULS) and a worldwide network of Galileo Sensor Stations (GSS).

  The two GCC, located in Oberpfaffenhofen (Germany) and Fucino (Italy) represent the core of the Ground Segment. Each control centre handles control functions supported by a *Galileo Control Segment* (GCS) and mission functions supported by a *Galileo Mission Segment* (GMS). The GCS manages the monitoring and the maintenance of the satellite constellation status and configurations while the GMS manages navigation system control. The GCS uses the TT&C stations to communicate with each satellite to provide telemetry data to the Galileo satellites, and to distribute and uplink the control commands needed for the maintenance of the Galileo constellation. The GMS has the role to determine and uplink the navigation messages needed to furnish the navigation and timing data. For this purpose, the worldwide network of GSS is exploited. The GCC analyses the GSS collected data in order to provide Galileo navigation and integrity data messages. Then, the nine ULS are involved to uplink these data from the GCC to the satellites.

- The *User Segment* which includes the Galileo receivers providing positioning, velocity and timing to the whole user community.

[1] From the beginning of 2023 Galileo's functionality has been enhanced with the addition of a new high-precision service that can achieve horizontal accuracy of 20 cm and vertical accuracy of 40 cm. See https://www.esa.int/Space_in_Member_States/Italy/Il_nuovo_servizio_di_Galileo_offrira_una_precisione_di_20_cm

2.2 Galileo satellites

Two experimental Galileo satellites were launched in December 2005 and April 2008: the satellites GIOVE-A (*Galileo In Orbit Validation Element*) and GIOVE-B respectively. The main purpose of these satellites was to test and validate the technologies to be used in the operational Galileo constellation as well as the reception and the performance of the generated Galileo signals. The 2 GIOVE prototype vehicles were retired in 2012.

The *In-Orbit-Validation* (IOV) phase started in 2011 with the launch of two operational Galileo satellites and placed in the first orbital plane. A year later, the launch of the next two satellites was performed with their placement in the second orbital plane. The IOV phase consisted of testing and operating the four spacecraft and their associated ground infrastructure.

2.2.1 The Galileo FOC satellites

The successful completion of the IOV phase was followed by the FOC (*Full-Operational-Capability*) phase. In August 2014 the first pair of Galileo FOC satellites, GSAT0201 and GSAT0202, were launched. They were erroneously placed on an incorrect orbit, with relatively high eccentricity ($e \simeq 0.23$). Successively, the orbit was corrected ($e \simeq 0.16$) and it was possible to use these two satellites for navigation. However, the relatively high eccentricity of these two satellites with respect to the others Galileo FOC, makes them attractive for Fundamental Physics measurements (as already shown in Chap.1).

Over the years, there have been other launches of Galileo FOC satellites. The planned Galileo Space Segment consisted of 30 artificial satellites in which 6 of them are spares. The completion of Batch-3 will bring to the total of 34 Galileo FOC.

As of August 2023, 28 Galileo (4 IOV and 24 FOC) spacecrafts have been launched: 23 satellites are operational, 1 is not available and 4 are currently[2] not usable[3].

Each FOC satellite has a mass of about 700 kg and 4 onboard atomic-clocks, two Rubidium Atomic Frequency Standard (RAFS) and two Passive Hydrogen Maser (PHM). In fact, for a GNSS to work properly, very stable clocks are needed to synchronise the signals transmitted by the satellites. In addition, good clock stability is extremely important for positioning accuracy. The PHM exploits the ultra-stable 1.4 GHz transition in an hydrogen atom to provide time-measurements with a time drift within 0.45 ns over 12 hours. Regarding the RAFS, the time accuracy is within 1.8 ns over 12 hours. This stability is required since an error of few nanoseconds would produce an error of the order of metres in positions measurements that would be inappropriate.

Only data from a single clock are used at a time. In particular, the operating PHM generates the reference frequency from which other units can produce the navigation signal that the Galileo satellites will broadcast. If the operating PHM fails, it will be immediately replaced by the other PHM and the two RAFS reserve clocks will be activated. In this way, the generation of the navigation signal is guaranteed at all times. More in depth information on clocks physical characteristics and their mode of operation will be discussed in Chap.5.

In addition to atomic clocks, satellites are equipped with other components for various purposes (see Fig.2.1):

- the L-band antenna for the transmission of the navigation signal (frequency-range: 1200 – 1600 MHz),
- the C-band antenna for the reception of mission data from Galileo ULS. This comprises data for the onboard clocks synchronisation with the on ground reference clock and integrity data,
- two S-band antennas which provide TT&C functions to maintain the operation of the satellite in orbit,
- the SAR (Search and Rescue) antenna to pick up signals from emergency beacons and transmit these to national rescue services,

[2] 8th January 2024.

[3] It is possible to check the status of the satellite by visiting https://www.gsc-europa.eu/system-service-status/constellation-information.

- the Laser Retro-reflector Array (LRA) which allows the measurements of the satellite position through the Satellite Laser Ranging (SLR) technique (see §2.3.3),
- the space radiators have the function to keep all the spacecraft units within their operational temperature range rejecting heat to deep space.

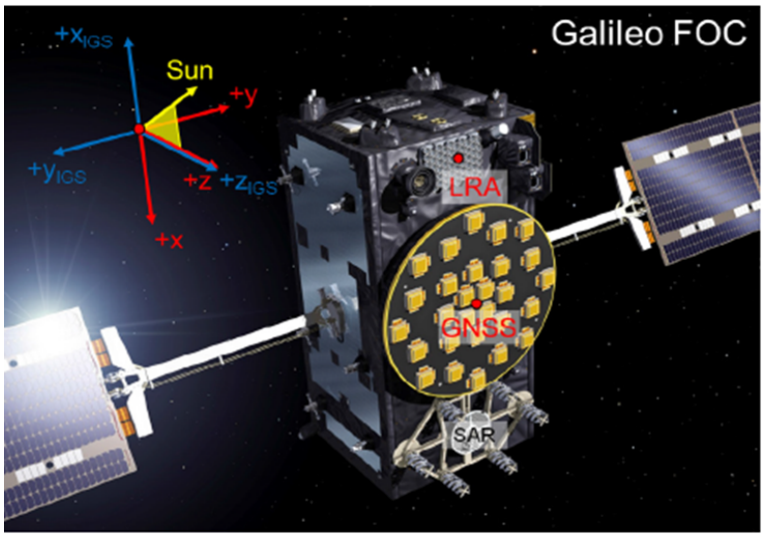

Figure 2.1. *The Galileo FOC satellite. Red arrows and labels refer to the manufacturer specific system, while IGS axis conventions are shown in blue. We refer to §2.5 for the interpretation of the red reference system. Credits: [41] and ESA.*

In 2021, ESA planned the development and the construction of the first batch of the *Galileo Second Generation* (G2) satellites. The new G2 satellites are expected to be available by 2025 and they will incorporate new on-board technologies. In particular, electric propulsion will be used to move the satellites from the injection orbit to their final operational orbits. In addition, the inter-satellite link between the satellites will allow them to routinely cross-check their performance and reduce their dependence on the availability of ground facilities[4].

2.2.2 Galileo FOC geometry and physical characteristics

Information on the spacecraft geometry and its physical properties was extracted from the ESA Galileo Metadata.

Simplifying the satellite structure as a *Box-Wing*, *i.e.* as a parallelepiped body (Box) and two rectangular surfaces (Wings) attached to it, the ESA Galileo Metadata provide dimensions of the Box spacecraft as well as the average optical coefficients for the Box panels and the Solar Arrays of the Wings. These properties are reported in Tab.2.1 and in Tab.2.2. As an example, we show in Fig.2.3 the Simplified Box-Wing (S-BW) we build with the software `COMSOL`. In Chap.3 §3.5 we describe the `Matlab` S-BW developed for the G4S_2.0 activities, on the basis of the available information released by ESA, and its applications. Then, in §3.6, a description of the S-BW model build with COMSOL, with the aim of applying the Ray-Tracing technique, is also provided.

However, as fully discussed in [30], the information provided is not sufficiently detailed. For instance, according to ESA Metadata, the surface $+Z$ of the spacecraft is made up of only two materials, A and B. However, their combined properties are not comparable to those of the real components of the surface, as can be seen in Fig.2.4. In fact, as it is shown in [30], this surface is characterised by a set of antennas, corner cube retroreflectors and Earth sensors which have different optical properties to those associated to A and B in ESA Metadata. In addition, a mylar sheet, coated with Silver and Beryllium, was used to cover both the L-band antenna and the exagonal surface occupied by the SAR antennas. Therefore, the knowledge of the mylar

[4]More information is available at https://www.esa.int/Applications/Navigation/Galileo_Second_Generation_enters_full_development_phase

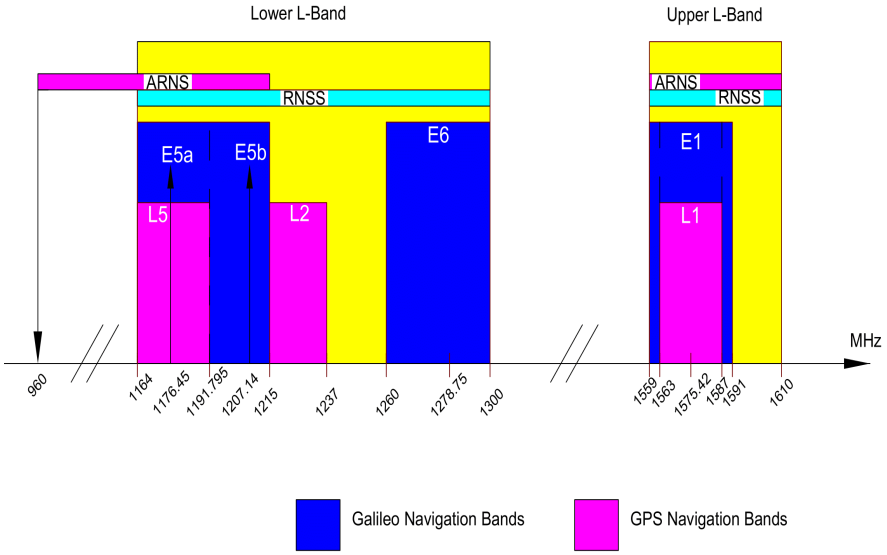

Figure 2.2. *The Galileo frequency bands have been selected in the allocated spectrum for Radio Navigation Satellite Services (RNSS) and in addition to that, E5a, E5b and E1 bands are included in the allocated spectrum for Aeronautical Radio Navigation Services (ARNS), employed by Civil-Aviation users, and allowing dedicated safety-critical applications. Figure adapted from the "Galileo OS SIS ICD v2.0" document available on: https://galileognss.eu/wp-content/uploads/2021/01/Galileo_OS_SIS_ICD_v2.0.pdf*

Dimensions [m]		Surface areas [m^2]	
ΔX	2.530	$\pm X$ panel	1.320
ΔY	1.200	$\pm Y$ panel	2.783
ΔZ	1.100	$\pm Z$ panel	3.036

Table 2.1. *Dimensions and surface areas of the Box of Galileo FOC satellites from ESA Metadata.*

optical properties is also required instead of those of the previously mentioned antennas. This is just an example of the amount of detail that is necessary to build a spacecraft model that is as close to reality as possible.

2.3 Galileo observables

2.3.1 The pseudorange

The *travel time* or *time of flight* Δt of the signal to propagate from the phase centre of the satellite antenna (at the transmission time) to the phase centre of the receiver (at the reception time) is one of the basic GNSS observables [32]. Measuring Δt allows to determine the distance between a receiver and a satellite, which is the so called *pseudo-range*, $\rho = c\Delta t$, where c is the speed of light.

Technically the pseudo-range is obtained by extracting the ranging codes[5], a binary sequence different for each satellite, contained in the Galileo navigation signals: the receiver obtains Δt finding the maximum correlation between the received code from the satellite and its replica generated in the receiver. Since pseudo-range measurements are affected by signal or instrument errors, they do not give the true geometric distance between the satellite (s) and the receiver (r). Therefore, we need first take into account the possible synchronisation errors between the receiver and the satellite clock, which are characterised by different reference time scales (T_2 and

[5]also called Pseudo-Random Noise (PRN) sequences or PRN codes.

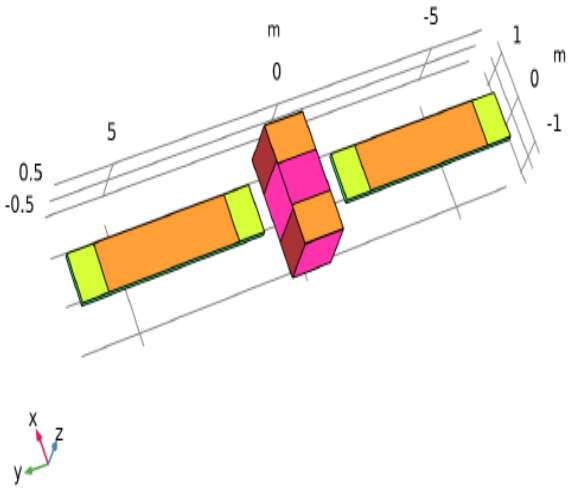

Figure 2.3. *Our S-BW model in COMSOL based on ESA Galileo Metadata. The colours correspond to the material reported in Tab.2.2.*

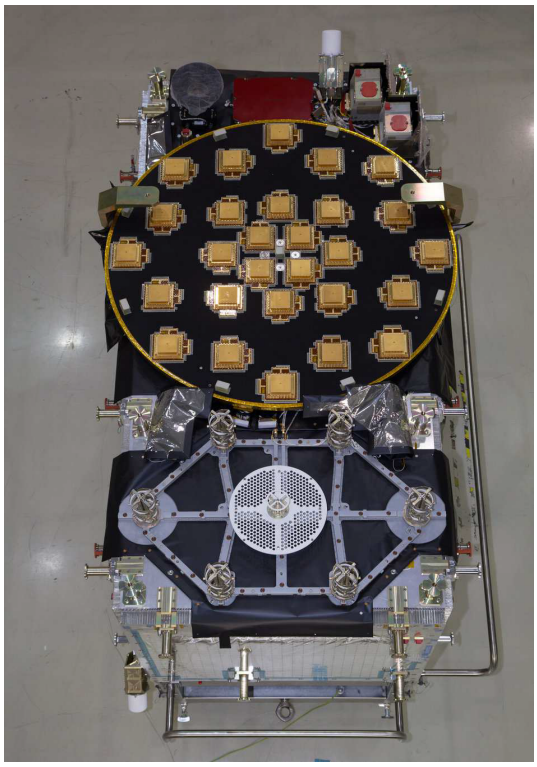

Figure 2.4. *Galileo FOC spacecraft: photo of the +Z panel. Courtesy of ESA.*

Component	Surface	Material	Area $[m^2]$	α	ρ	δ
Box	+X	A	0.440	0.93	0.00	0.07
		C	0.880	0.08	0.73	0.19
	$-X$	A	1.320	0.93	0.00	0.07
	$+Y$	A	1.129	0.93	0.00	0.07
		C	1.654	0.08	0.73	0.19
	$-Y$	A	1.244	0.93	0.00	0.07
		C	1.539	0.08	0.73	0.19
	$+Z$	A	1.053	0.93	0.00	0.07
		B	1.969	0.57	0.22	0.21
	$-Z$	A	2.077	0.93	0.00	0.07
		C	0.959	0.08	0.73	0.19
Wing	+SA	E	3.880	0.92	0.08	0.00
		D	1.530	0.90	0.10	0.00
	-SA	E	3.880	0.92	0.08	0.00
		D	1.530	0.90	0.10	0.00

Table 2.2. *Surfaces of the satellites with their materials, corresponding area and optical coefficients, according to ESA Galileo Metadata. α,ρ and δ are the absorption, reflection and diffusion coefficients, respectively. They represent the average values of the materials coefficients in the visible part of the electromagnetic spectrum.*

T_1 respectively). So, the signal time of flight can be written as:

$$\rho = c[t_r(T_2) - t_s(T_1)]\,, \tag{2.1}$$

where $t_r(T_2)$ is the reception time of the signal, measured at the time scale of the receiver clock and $t_s(T_1)$ is the emission time of the signal, measured at the time scale of the satellite clock. Denoting GNSS time scale by a superscript ^{GNSS} and offsets of the receiver and the satellite clocks from GNSS time[6] by the symbols δt_r and δt_s, the pseudorange is obtained as:

$$\rho = c[(t_r^{GNSS} + \delta t_r) - (t_s^{GNSS} + \delta t_s)] \tag{2.2}$$

We can write the above expression using $\Delta t^{GNSS} = t_r^{GNSS} - t_s^{GNSS}$ and $\delta t = \delta t_r - \delta t_s$

$$\rho = c(\Delta t^{GNSS} + \delta t)\,. \tag{2.3}$$

It is evident that the pseudorange is larger than the actual signal path by a distance $c\delta t$ which depends on the relative offset of the two clocks. A more complete expression considers errors related to atmospheric signal delays and instrumental delays[7]:

$$\rho = d + c(\delta t_r - \delta t_s) + \Delta\rho_{ion} + \Delta\rho_{trop} + K_r + K_s\,. \tag{2.4}$$

where d is the geometric distance between the receiver and the satellite, $\Delta\rho_{ion}$ the ionospheric range correction, $\Delta\rho_{trop}$ the tropospheric range correction, K_r and K_s the receiver and the satellite instrumental delays which are dependent on the code and frequency.

2.3.2 The carrier-phase

A measurement of the apparent distance between a satellite and a receiver is also obtained from the *carrier phase*, in units of cycles of the carrier frequency. The Galileo navigation signal are radio-frequency (RF) signals in L-band (more precisely in E-band) that consists in a RF

[6] including the relativistic satellite clock correction. This correction, also called keplerian correction (τ_{kepl}), is needed for navigation purposes in order to take into account the eccentricity of the orbit. It assumes the following form: $-\frac{2\boldsymbol{x}\cdot\boldsymbol{v}}{c^2}$, where $\boldsymbol{x}$ and $\boldsymbol{v}$ are the satellite's position and velocity vectors, respectively.

[7] Multipath effects and the offset of the GNSS antenna phase center from the satellite center of mass, should be also considered for a detailed description of the pseudorange measurements. Another source of error to consider in Eq.2.4 is the receiver noise.

carrier modulated by a Pseudo-Random-Noise (PRN) code[8]. We can treat any signal as a sinusoid which has the following complex notation: $Ae^{i(\omega t+\theta)}$, where A is the amplitude, ω the frequency and θ is the phase in radians when $t = 0$. When the RF signal is modulated by the PRN code, the resulting signal is no longer a sinusoid but can be expressed as a linear combination of sinusoids, according to the Fourier theorem. For GNSS signal processing, we define the signal phase as the phase of the carrier signal. In other words, this is the phase of the pure sinusoid that would result if the PRN code and any other modulation were removed.

The phase $\phi_r(t)$ of the GNSS satellite signal received by the user at GNSS time t is given as $\phi_r(t)$ [33]:

$$\phi_r(t) = f_s(t - \Delta t^{GNSS}) + f_s\delta t_s\,, \tag{2.5}$$

where f_s is the emitted frequency and $f_s\Delta t^{GNSS}$ denotes the phase retardation due to the signal propagation from the satellite to the receiver. At the receiver a reference signal with phase

$$\phi_{ref}(t) = f_{ref}t + f_{ref}\delta t_r \tag{2.6}$$

is generated using the receivers reference frequency f_{ref}. The phase difference

$$\phi_r(t) - \phi_{ref}(t) = N + \Delta\phi \tag{2.7}$$

can be expressed by an integer number of cycles N and the actual measurement value $\Delta\phi$. As $f_{ref} = f_s$, by inserting Eq.2.5 and Eq.2.6 into Eq.2.7 we obtain — after multiplying by the wavelength λ — the *observation equation*:

$$\rho_\phi(t) = c\Delta t^{GNSS} + \lambda N + c\delta t\,, \tag{2.8}$$

where $\rho_\phi = -\lambda\Delta\phi$ is the range equivalent of the measured phase difference, *i.e. phase-pseudorange*. The integer N is unknown, thus phase difference measurement is ambiguous up to an integer multiple of whole cycles/wavelenghts.

Carrier phase measurements are affected by the same sources of error as described for the pseudorange observable but it is not possible to measure the whole number of cycles between the satellite and the receiver for the carrier phase ambiguity. Every time the receiver loses the lock of the signal, this ambiguity changes arbitrarily, causing jumps or discontinuities in the range.

Concerning the errors, phase measurements and code pseudo-range measurements are subject to systematic and random errors. Systematic errors are at the origin of measurements biases, which must be adequately taken into account to correctly estimates the so-called clock-bias.

A reliable clock-bias estimate is necessary for the gravitational redshift experiment and for the domain wall dark matter constraint experiment. The main sources of measurement biases are related to satellite orbits, propagation medium, satellite atomic clocks and receiver clock, antenna phase center variations, and relativistic effects, to name just a few systematic sources of error.

2.3.3 SLR technique

Unlike GNSS pseudorange or carrier phase observations, which measure the travel-time of an electromagnetic radiation by comparing the transmitter and receiver clocks, the *Satellite Laser Ranging* (SLR) is a two-way measurement system that uses a single clock to determine the round-trip time between the transmission and reception of a laser pulse. This means that it does not involve an unknown clock difference and has very small biases, in the mm to cm range.

Laser pulses are transmitted from a SLR ground station to Cube Corner Retro-reflectors (CCRs) on a satellite (a valuable discussion of this technique can be found in [34]). Laser tracking data are usually known as normal points (NPs) and provide the station-satellite distance. They are obtained by averaging the tracking data (full rate data) over a specified time interval, which depends on both the LRA structure and the height of the satellite. In the case of GNSS satellites, the averaging time is usually 5 minutes. The result is an average value with a corresponding root

[8]The PRN codes allow the receiver to determine the travel time of the radio signal from the satellite to the receiver, as mentioned in the previous paragraph.

mean square (RMS) value[9]. These high quality data are currently provided by the International Laser Ranging Service (ILRS) with range NPs characterised by an accuracy of mm in their RMS [35]. In the case of the two LAGEOS satellites, an accuracy of a few mm is achieved in the RMS of their Normal Points, which corresponds to an accuracy of a few centimetres in orbit reconstruction using the best dynamicalal models for data reduction and empirical accelerations [36].

2.4 Galileo ephemerides and orbits

At each epoch, the satellite's motion is described by six parameters, which can be either the position and velocity vector components or the six Keplerian elements which are: the *right ascension of ascending node* (RAAN) Ω, the *inclination of the orbital plane i*, *the argument of perigee* or *pericenter* ω, the *semi-major axis of the orbital ellipse a*, its *eccentricity e* and the *perigee passing time* T_0[10] (see Fig.2.5).

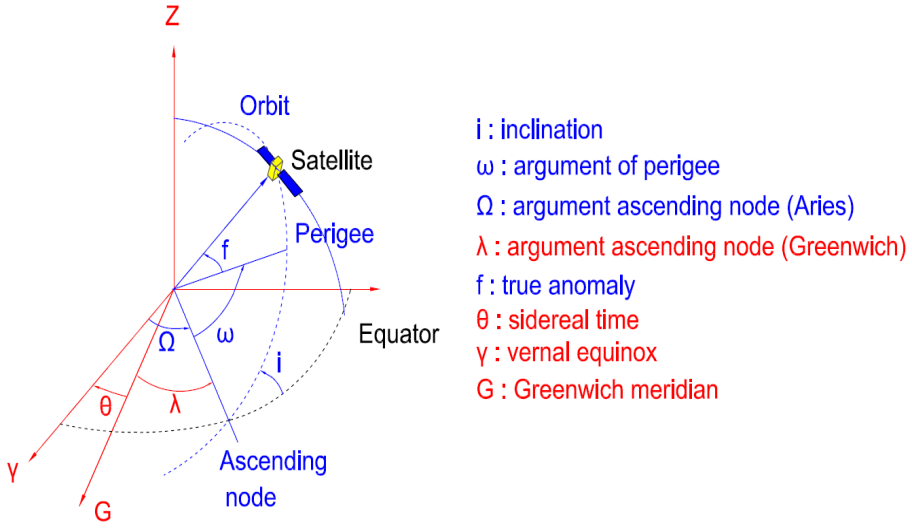

Figure 2.5. *GNSS satellite orbital elements. Figure adapted from [32].*

In the ideal 2-body keplerian case with no external perturbations, the orbit of an Earth satellite is an ellipse with all Keplerian elements constant of motion with the exception of the perigee passing time. In presence of perturbations (both gravitational and non-gravitational), we define *osculating ellipse* at time t the orbit that the satellite will follow if the external perturbations will be suddenly turned off. This osculating orbit will be defined by the initial condition at time t.

Some physical characteristics of some Galileo FOC satellites and their orbits are reported in Tab.2.3.

The navigation data contain all the parameters necessary for the user to calculate a complete position, velocity and time solution. They are stored on board each satellite for a specific time-period and are broadcast worldwide by all the satellites of the Galileo constellation. The 4 types of data needed to perform positioning are[11]:

- ephemerides parameters, which are needed to indicate the position of the satellite to the user receiver;
- time and clock correction parameters, which are needed to compute pseudo-range;

[9] For a detailed description of the NPs algorithm see https://ilrs.gsfc.nasa.gov/data_and_products/data/npt/npt_algorithm.html

[10] The orbital position of a satellite at a given time t can be obtained using the *perigee passing time* T_0 or one of the following 'anomalies': the true anomaly $f(t)$, the eccentric anomaly $E(t)$ and the mean anomaly $M(t)$.

[11] According to the "Galileo OS SIS ICD v2.0" document available on https://galileognss.eu/wp-content/uploads/2021/01/Galileo_OS_SIS_ICD_v2.0.pdf

- service parameters, which are needed to identify the set of navigation data, satellites, and indicators of the signal health;
- almanac parameters, which are needed to indicate the position of all the satellites in the constellation with a reduced accuracy.

Concerning the *ephemerides*, for each satellite of the Galileo constellation and for any epoch, a set of 16 parameters is transmitted to the user and updated regularly. These parameters are:

- 6 Keplerian elements, related to (but not equal to) the
  - mean anomaly M
  - eccentricity e
  - semimajor axis a
  - RAAN Ω
  - inclination I
  - argument of perigee ω
- 6 harmonic coefficients, related to the amplitude of the cosine and sine harmonic correction terms on the
  - argument of latitude u
  - orbit radius r
  - orbit inclination I
- 1 orbit inclination rate parameter $\dot{I}$
- 1 RAAN rate parameter $\dot{\Omega}$
- 1 mean motion correction parameter N, where the mean motion is defined as $n = 2\pi/P$ with P denoting the satellite's period
- 1 reference time parameter t_{0e} for the ephemeris data set.

These 16 parameters are processed by the Galileo receivers to compute the satellite position. In this procedure, the orbit is considered to be Keplerian and gravitational and non-gravitational perturbations are treated as time-dependent variations of the orbital elements. These temporal variations account for both *short-term effects*, at half of the orbital period, and *long-term effects*, *i.e.* the secular effects mainly related to the deviations of the Earth from the spherical symmetry in its mass distribution. The product is called as *Broadcast ephemeris* and has an accuracy of about 1 m. Broadcast ephemerides are regularly updated at time intervals ranging from 10 minutes up to 3 hours, depending on the GNSS constellation and on the type of the navigation message [37].

Precise orbits, as well as clocks-solutions, are also provided by some organisations such as IGS[12] (International GNSS Service) and ESOC[13] (European Navigation Support Office) in form of *combined orbits*.

IGS analysis centres provide satellite orbit solutions to the CDDIS[14] (Crustal Dynamics Data Information System) at predetermined intervals, *e.g.*, sub-daily, daily, or weekly, depending on the data product. The IGS Analysis Centre Cordinator then collects these solutions and produces a combined product, which is then archived at the CDDIS. These combined solutions are the official IGS products. This is a very important aspect, as a combined orbit product has a higher level of reliability and precision when compared to the orbits generated by a single analysis centres.

[12] https://igs.org/

[13] https://esoc.esa.int/

[14] CDDIS is NASA's public, active archive of space geodesy data, derived products, and related information. However, it also supports the international geodesy and Earth science community by providing timely access to the contents of its archive. More information at: https://cddis.nasa.gov/About/Background.html

Type	Eccentric orbit	Nominal orbit	Nominal Orbit
Name	GSAT0201, GSAT0202	GSAT0206	GSAT0208
PRN	E18, E14	E30	E08
Slot	Ext01, Ext02	A05	C07
Launch dates	August 22, 2014	September 11, 2015	December 17, 2015
Mass: m (kg)	660.977, 662.141	707.735	709.138
Average cross-section: $A_{\odot}(m^2)$	13.210	13.210	13.210
a (km)	27977.6	29599.8	29599.8
e	0.162	0.0	0.0
I (°)	49.850	56.0	56.0
Ω_0 (°)	52.521	317.632	197.632
ω_0 (°)	56.198	0.0	0.0
M_0 (°)	316.069, 136.069	0.153	120.153
$\dot{\Omega}$ (°/d)	-0.03986760	-0.02764398	-0.02764398
$\dot{\omega}$ (°/d)	+0.03383184	0.0	0.0
$\dot{M}$ (°/d)	+667.86467481	+613.72253566	+613.72253566
Period: P (hours)	12.94	14.08	14.08

Table 2.3. *Characteristics and orbital parameters of Galileo FOC satellites, mainly adapted from ESA Galileo metadata. The reference date for the satellites is 2016-11-21 at 00:00:00 UTC. Semi-major axis, eccentricity and inclination must be considered as mean values and not as obsculating elements. The metadata provides the indicated values for the mass of the satellites for December 2021 (see Tab.3.4 in Chap.3 for the mass values after the manoeuvres of the satellites)*

IGS combined orbit solutions are available in three forms: *ultra-rapid*, *rapid*, and *final*. The *ultra-rapid* product, useful for real-time and near real-time applications, is provided at regular intervals four times per day; this orbit solution includes both observed and predicted (or propagated) satellite orbits. The accuracy of these ultra-rapid orbits is about 3 cm for the observed orbits and about 5 cm for the predicted orbits. The *rapid* orbit combination is a daily solution available approximately 17 hours after the end of the previous UTC day. The *final*, which is the highest quality IGS solutions, consists of daily orbit files, generated on a weekly basis approximately 13 days after the end of the solution week.

All these products are reported in the "`Extended Standard Product 3 Orbit Format`" (`SP3-c`) files and listed in subdirectories by GPS week. They are available to the scientific community on the IGS website[15], as well as other IGS products, *i.e.* clock solutions, Earth Rotation Parameters, station positions.

Therefore, the orbit of a satellite can be derived from Navigation data (*i.e.* Broadcast ephemeris) or can be obtained in the form of precise orbits, such as those produced by the official analysis centres of IGS in the form of combined orbits.

2.5 The Galileo FOC attitude law

For a GNSS spacecraft, the attitude is functional to the navigation task and to the corresponding requirements needed to ensure it. In this context, three drivers need to be satisfied [38]:

1. the antenna boresight needs to be kept towards the Earth's centre to provide the proper coverage and signal strength to the on-ground receivers;

2. the solar panels need to maximise the received solar radiation, by aligning them perpendicularly to the Sun direction;

3. one of the spacecraft's faces perpendicular to the antenna boresight and the solar panel's axis of rotation should face away from the Sun to improve the thermal stability of the atomic clocks (which are close to this position).

[15] https://www.igs.org/products

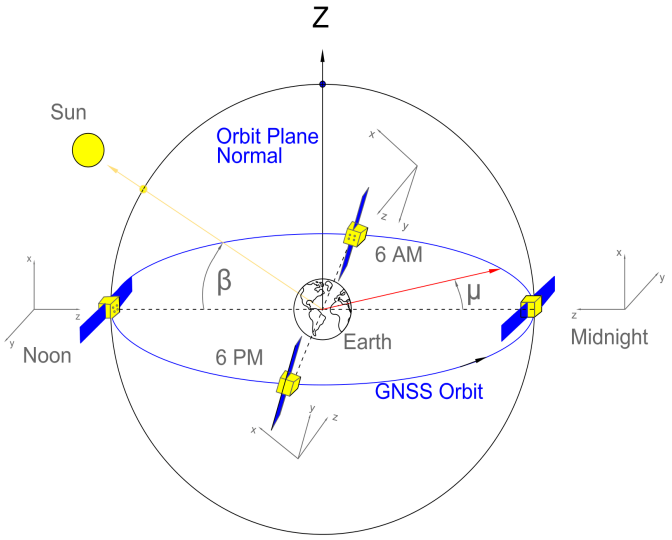

Figure 2.6. *The nominal yaw-steering mode for a GNSS spacecraft. Figure adapted from [41].*

The result of these requirements is the implementation of the *yaw-steering* (YS) mode, firstly implemented by GPS [39] and later by most other constellations [40].

A body reference frame is assumed with the $+Z$ axis aligned with the antenna boresight direction, the $+Y$ axis parallel to the solar panel rotation axis, and the X axis chosen so that the $-X$ panel is illuminated by the Sun during nominal YS, while the $+X$ panel is oriented towards deep space (see Fig.2.1). In order to follow the three drivers, the attitude law requires a rotation of the spacecraft body around the Earth pointing $+Z$-axis (yaw axis) as well as a rotation of the solar panels around the $+Y$-axis (pitch axis) to be perpendicular to the Sun (see Fig.2.6). Therefore, in order to maintain the nominal attitude, it is necessary to turn about its yaw-axis while rotating its solar panels around the $+Y$-axis. In this way, the spacecraft attitude is fully described by the *yaw-angle* Ψ. Indeed, this attitude-law is also called *yaw-steering law*. The yaw-angle Ψ is function of just two other angles: the Sun elevation $\beta_\odot$ with respect to the orbital plane and the satellite position angle μ on the orbital plane measured with respect to the Midnight ($\mu \simeq 0°$) point or to the Noon point ($\mu \simeq 180°$) of the orbits (see Fig.2.6):

$$\Psi = atan2\left(\frac{-\tan\beta_\odot}{\sin\mu}\right), \tag{2.9}$$

where for the origin of μ we followed the first convention in agreement with [41], while atan2 refers to the range $(-\pi, +\pi)$ for the variability of the yaw-angle.

According to ESA Galileo Metadata[16], for a Galileo FOC satellite the Eq.2.9 is as follows:

$$\Psi = atan2\left(\frac{\hat{s}(t)\cdot\hat{n}(t)}{\hat{s}(t)\cdot(\hat{r}(t)\times\hat{n}(t))}\right) \tag{2.10}$$

where

- t is the current on-board computer time
- $\hat{s}(t)$ is the Sun position unit vector
- $\hat{r}(t)$ is the satellite position unit vector
- $\hat{n}(t)$ is the orbit normal unit vector

[16] https://www.gsc-europa.eu/support-to-developers/galileo-satellite-metadata

and all these unit vectors are in the Earth Centered Inertial (ECI), J2000.0, reference frame. However, there are some limitations of this law related to the performance of the onboard reaction wheels. Indeed, during the eclipse season and, in particular, for small values of the $\beta_\odot$ angle (above or below the satellite's orbital plane) and close to Midnight and close to Noon, the Galileo satellites have to perform fast yaw-slews to accomplish Eq.2.9, *i.e.* an almost instantaneous rotation by 180° after crossing the orbit Midnight or Noon position. This condition cannot be fulfilled by the maximum rotation rate of the reaction wheels which prevent a nominal manoeuvre during these phases. Consequently, for small values of $\beta_\odot$ angle and when there is a collinear condition between the Sun and the spacecraft vectors with respect to the Earth, the following modified yaw-steering law is used:

$$\Psi_{mod}(t_{mod}) = 90^\circ \cdot sign + (\Psi_{init} - 90^\circ \cdot sign) \cdot cos\left(\frac{2\pi}{T_0} t_{mod}\right) , \tag{2.11}$$

- t_{mod} is the elapsed time since the switch is over,
- Ψ_{init} is the yaw-angle $\Psi(t)$ at the time of the switch over to the modified yaw profile,
- sign is the sign of Ψ_{init},
- the period $T_0 = 5656$ s corresponds to about two times the maximum duration of the noon/midnight manoeuvre.

As reported in ESA Galileo FOC metadata, the switch over the modified yaw-steering law takes place when all of the following conditions are satisfied:

- the Sun elevation angle $\beta_\odot$ is smaller than the value $\beta_0 = 4.1^\circ$
- the current collinearity angle ϵ is smaller than the value $\epsilon_0 = 10.0^\circ$
- the collinearity angle for the previous epoch was bigger than ϵ_0.

The collinearity angle ϵ is defined as:

$$\begin{cases} \epsilon = arccos(\hat{r} \cdot \hat{y}) & \text{if} \quad arccos(\hat{r} \cdot \hat{y}) \leq 90^\circ \\ \epsilon = 180^\circ - arccos(\hat{r} \cdot \hat{y}) & \text{if} \quad arccos(\hat{r} \cdot \hat{y}) > 90^\circ \end{cases} \tag{2.12}$$

where

$$\begin{cases} \hat{x} = \hat{n} \times \hat{s} \\ \hat{y} = \hat{n} \times \hat{x} \end{cases} \tag{2.13}$$

In Fig.2.7 it is shown the comparison of the nominal and the modified yaw-steering law described in Eq.2.10 and Eq.2.11 for the GSAT0208, in circular orbit, over a simulation period of 1 year. The two laws overlap perfectly outside the eclipse season, but show differences close to and during eclipses, with the consequence of a lack of orthogonality of the solar panels to the incident solar radiation. The differences between the two attitude laws can be seen in Fig.2.8, where the smoothest variation of the modified law with respect to the nominal law is clear and evident.

It is worth mentioning that the yaw steering law reported in ESA Galileo Metadata was designed for satellites in nominal orbit, *i.e.* circular orbit, like every GNSS satellites, and not for those in elliptical orbits such as GSAT0201 and GSAT0202. However, this law is equally applied to these satellites[17]. Denoting θ the angle between the normal to the solar panels and the direction of the incident solar radiation, Fig.2.9 shows that θ, in the case of elliptical orbit, is ~ 2.5 times greater than its value (about 4°) in the case of nominal orbit. Therefore, this attitude law is not optimized in the case of the satellites in elliptical orbit and will impact in their orbit determination during the eclipse season, if not included in the model.

[17] E. Schoenemann (ESA) private communication.

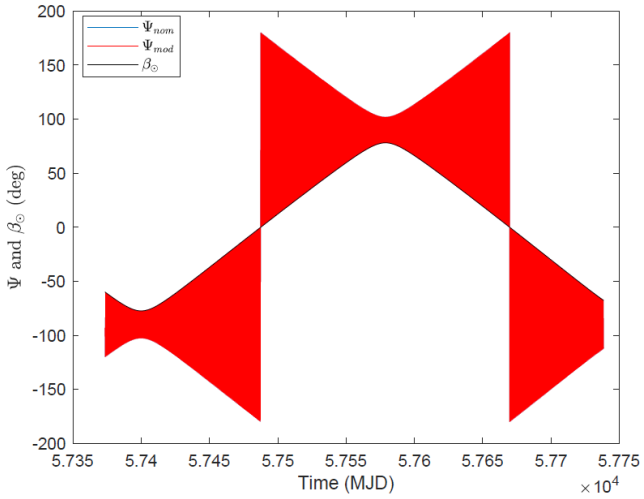

Figure 2.7. *Nominal (blue) and modified (red) attitude law for GSAT0208. Two eclipse seasons are shown. The starting epoch corresponds to November 21, 2016. The black line defines the variation of the Sun's altitude with respect to the orbital plane in the period shown.*

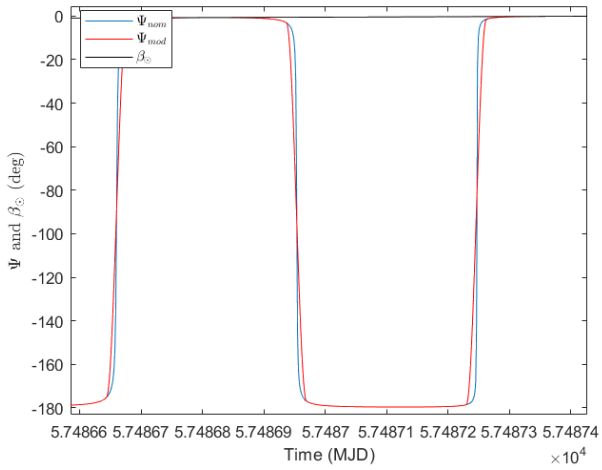

Figure 2.8. *Detail of Figure 2.7 close to the first eclipse season.*

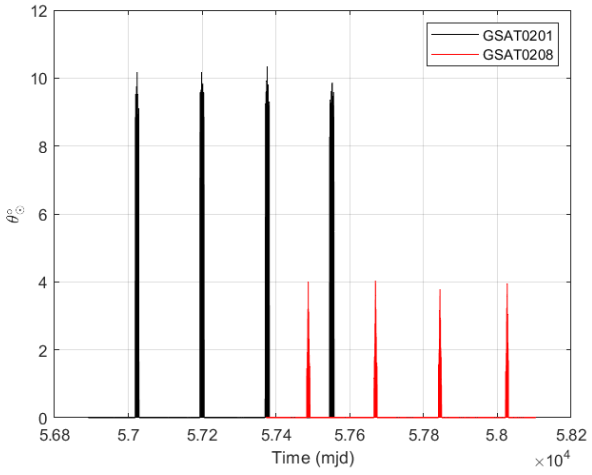

Figure 2.9. *Angle between the normal to the solar panels and the direction of the incoming solar radiation: comparison between GSAT0201 in elliptical orbit and GSAT0208 in quasi circular orbit.*

Chapter 3

Perturbations and Models

Many perturbing accelerations act on a satellite, causing its orbit to deviate from the Keplerian orbit. This Chapter provides an overview on these perturbations and their effects on the satellite's orbital elements. First, we introduce the perturbations of gravitational origin, those responsible for the major deviations from the ideal Keplerian orbit of a two-body system. We then turn our attention to perturbations related to non-conservative forces, *i.e.* non-gravitational perturbations.

The main non-gravitational perturbation is the direct solar radiation pressure. It is therefore necessary to build a sufficiently accurate model for it before being able to seriously consider smaller perturbation effects, such as those related to terrestrial radiation and thermal thrust effects. In the context of the G4S_2.0 project, this is very useful to better characterise the dynamical model of the satellite to be used in the precise orbit determination from which it will be possible to extract the measurements of our interest. In this Chapter we also show our Box-Wing model of the satellite and the perturbing accelerations produced by the direct solar radiation pressure, as well as its long-term effects on the orbital elements.

3.1 The satellite perturbed motion

The Keplerian motion of a satellite orbiting the Earth is perturbed by a wide range of physical causes, resulting from the interactions of the spacecraft with natural celestial bodies and with the atoms, particles and fields encountered along its way. This lead to *perturbing accelerations* of different origin (both gravitational and non-gravitational). These accelerations have to be managed appropriately in the satellite dynamical model which is indispensable for the precise orbit determination (POD), *i.e.* the procedure of obtaining a precise description of the satellite's orbit by fitting the tracking data with a suitable set of dynamical models.

The equation that describes the motion of any artificial satellite around the Earth may be written as:

$$\boldsymbol{a} = \boldsymbol{a}_{Mon} + \boldsymbol{a}_{GP} + \boldsymbol{a}_{NGP} + \boldsymbol{a}_{GR} \tag{3.1}$$

where $\boldsymbol{a}_{Mon}$ provides the main contribution from the Earth's monopole acceleration, while the other terms provide, respectively, the acceleration contribution from the gravitational perturbations (GP), from the non-gravitational perturbations (NGPs) and from the General Relativity main contributions (GR).

POD techniques, applied to GNSS satellites, have become more precise over time as a consequence of the remarkable increase in accuracy of distance measurements from the satellite to ground stations. This highlighted the complex and subtle effects of the NGPs on their orbit. Consequently, the need to consider properly their perturbing effects has become necessary to further improve the POD of these satellites at the current level of the microwave-ranging accuracy/precision [42–46]

As written in §2.2.1, the Galileo-FOC satellites have a complex shape characterised by solar panels, motors and antennas. Therefore, modelling NGPs is further complicated with respect to passive satellites which do not have this complex structure. One of the G4S_2.0 objectives is to manage the NGP in such a way to obtain the best possible POD for Galileo satellites, on the basis of the current tracking technologies of their orbits, *i.e.* microwave and satellite laser

ranging (SLR). As previously anticipated in Chap.1, this task is being carried out with a view to future measurements in the field of Fundamental Physics that we intend to perform by exploiting a better knowledge of the orbits of the Galileo satellites.

A possible alternative is to use an on-board *accelerometer* that directly measures the effects of NGPs on the satellite, which would then no longer need to be modelled. In addition, these measurements can be used to calibrate models, or they can be used in a complementary way. The G4S_2.0 activities related to NGPs will also help to define the main characteristics of an on-board accelerometer, such as its sensitivity and measurement bandwidth, to be considered as a new payload for a next generation of Galileo satellites to further improve the performance of the Galileo constellation.

In the following sections, we will provide an overview on the main perturbations that act on the Galileo-FOC satellites, with a particular attention to the direct solar radiation pressure.

3.2 Gravitational perturbations

The gravitational perturbations are mainly due to the non-sphericity of the Earth and to tidal effects. The Earth's mass distribution is not spherically symmetric and deviations from this symmetry are responsible of additional terms with respect to the Newtonian one (or monopole). Moreover, Earth's mass is not distributed equally and it also changes over time.

It is worth mentioning that the knowledge of gravitational perturbations plays an important role both in the satellite POD and in the estimation of the main sources of systematic errors that affect a measurement. The correct modelling of the even zonal harmonics (l = even, $m = 0$) represents the main challenge in some GR measurements, *e.g.* the relativistic precessions, since they have the same signature of the relativistic effect but much larger amplitudes. Therefore, as we will see in section §3.2.2, to reduce the impact of these coefficients on these relativistic measurements, we model them taking into account for their significant time dependence.

Please, see Tab.4.1 in §4.1.1.1 for gravitational field models that we use in the POD.

3.2.1 Geopotential: static contribution

The Earth's potential U (the geopotential) can be represented by a spherical harmonic expansion [47]:

$$U = \frac{GM_T}{r} \sum_{l=0}^{\infty} \sum_{m=0}^{l} \left(\frac{R_T}{r}\right)^l P_{lm}(\sin\varphi)(C_{lm}\cos(m\lambda) + S_{lm}\sin(m\lambda)) \,, \tag{3.2}$$

where R_T is the Earth mean equatorial radius, r is the geocentric distance of the satellite, φ and λ are the geocentric latitude and longitude, P_{lm} are the associated Legendre functions and the coefficients C_{lm} and S_{lm} depend on the Earth's mass distribution. The indices l and m are called, respectively, degree and order of a particular harmonic term. The coefficients completely characterise the gravitational potential outside the mass distribution itself. In practice, the series is truncated at some finite l_{max} and the model is then sensitive to inhomogeneities at the scale of $\pi R_\oplus / l_{max}$. The lower-degree harmonics are related to the choice of the reference frame in which the potential itself is expressed, and have been fixed accordingly in our analysis. The geopotential coefficients are classified in zonal harmonics ($m = 0$), tesseral ($m < l$) and sectorial ($m = l$), see Fig.3.1.

In the case of zonal coefficients, the notation $J_l = -C_{l0}$ is commonly used, as all S_{l0} coefficients vanish. Since the magnitude of Legendre functions (and hence of the coefficients) cover a range of ten or more orders of magnitude with l and m, the functions are usually normalised and the new "normalised" coefficients $\bar{C}_{lm}$ and $\bar{S}_{lm}$ are given by:

$$\left\{ \begin{array}{c} \bar{C}_{lm} \\ \bar{S}_{lm} \end{array} \right\} = \sqrt{\frac{(n+m)!}{(2-\delta_{0m})(2n+1)(n-m)!}} \left\{ \begin{array}{c} C_{lm} \\ S_{lm} \end{array} \right\} . \tag{3.3}$$

So, we can derive the acceleration due to the Earth's gravity potential in terms of the

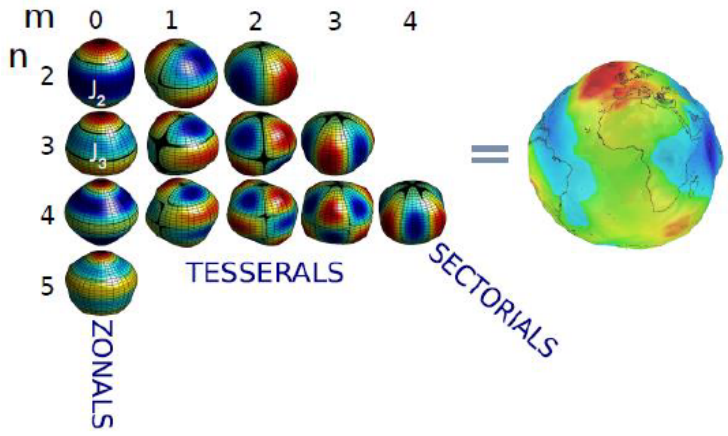

Figure 3.1. *Tesseral, zonal and sectorial coefficients are used to describe the Earth's gravitational field. The zonal coefficients describe the dependence on latitude only, while the tesseral coefficients describe the dependence on both latitude and longitude. The sectorial coefficients describe the dependence on longitude only. On the right the real Earth gravitational field characterised by gravity anomalies measured by the mission GRACE (Gravity Recovery And Climate Experiment) [49].*

normalised geopotential coefficients [48]:

$$\ddot{r} = \nabla \frac{GM_T}{r} \sum_{l=0}^{\infty} \sum_{m=0}^{l} \left(\frac{R_T}{r}\right)^l \bar{P}_{lm}(\sin\varphi)(\bar{C}_{lm}\cos(m\lambda) + \bar{S}_{lm}\sin(m\lambda))\,, \tag{3.4}$$

where the normalised associated Legendre functions are

$$\bar{P}_{lm} = \sqrt{\frac{(2-\delta_{0m})(2n+1)(n-m)!}{(n+m)!}} P_{lm}\,. \tag{3.5}$$

From Tab.3.1, it is evident that the acceleration due to the Earth's monopole term is the major contribution to the satellite's motion. The perturbing effects are generally compared with it in order to quantify their entities in the perturbed motion with respect to the Keplerian one. The comparison is also extended to LAGEOS II, one of the best tracked satellites by the ILRS.

The most relevant perturbing acceleration is due to the $\bar{C}_{20}$ coefficient, *i.e.* the Earth's oblateness. For a Galileo-FOC satellite, the acceleration due to this coefficient is smaller by a factor of 10^4 with respect to the one due to the Earth's monopole but it is approximately three order of magnitude larger than any other acceleration due to the other coefficients. Eq.3.6 shows how the even zonal harmonics, in particular the coefficient $\bar{C}_{20}$, influence the evolution of the orbit, in this case of the argument of pericenter, the main observable for the measurement of the relativistic precessions.

$$\dot{\omega}^{\text{class}} = -\frac{3}{4} n \left(\frac{R_\oplus}{a}\right)^2 \frac{1-5\cos^2 i}{(1-e^2)^2} \left(-\sqrt{5}\bar{C}_{20} + \dots\right). \tag{3.6}$$

Therefore, a reliable knowledge of these harmonics is crucial to achieve an accurate measurement of the main relativistic precessions predicted by GR or other alternative theories of gravitation.

For a more in-depth information on the static gravity field models, we refer to the International Centre for Global Earth Models (ICGEM): Global Gravity Field Models[1].

3.2.2 Geopotential: time-dependent contribution

Since the end of the 80s of the last century, it was known in the literature that the low-degree coefficients of the gravitational field of the Earth, and in particular the quadrupole coefficient $\bar{C}_{20}$,

[1] http://icgem.gfz-potsdam.de/tom_longtime

Table 3.1. *Comparison of the main gravitational accelerations (S.I. units) on LAGEOS II with the corresponding accelerations on a Galileo FOC satellite.*

Physical effect	Formula	Parameter [S.I. units/adim.]	LAGEOS II	Galileo FOC
Earth's monopole	$\frac{GM_\oplus}{r^2}$	$GM_\oplus = 3.986004418 \times 10^{14}$	2.6948	0.4549
Earth's oblateness	$3\frac{GM_\oplus}{r^2}(\frac{R_\oplus}{r})^2\bar{C}_{2,0}$	$\bar{C}_{2,0} = -4.841694573200 \times 10^{-4}$	1.08×10^{-3}	3.1×10^{-5}
Low-order geopotential	$3\frac{GM_\oplus}{r^2}(\frac{R_\oplus}{r})^2\bar{C}_{2,2}$	$\bar{C}_{2,2} = +2.439374598584 \times 10^{-6}$	5.4×10^{-6}	1.5×10^{-7}
Low-order geopotential	$7\frac{GM_\oplus}{r^2}(\frac{R_\oplus}{r})^6\bar{C}_{6,6}$	$\bar{C}_{6,6} = +9.476848430257 \times 10^{-9}$	3.7×10^{-9}	3.0×10^{-12}
High-order geopotential	$13\frac{GM_\oplus}{r^2}(\frac{R_\oplus}{r})^{[12]}\bar{C}_{12,12}$	$\bar{C}_{12,12} = +2.422093764787 \times 10^{-9}$	3.7×10^{-11}	1.4×10^{-16}
Moon	$2\frac{GM_\bullet}{r_\bullet^3}r$	$GM_\bullet = GM_\oplus/81.3$	2.2×10^{-6}	5.3×10^{-6}
Sun	$2\frac{GM_\odot}{r_\odot^3}r$	$GM_\odot = 1.32712442099 \times 10^{20}$	9.6×10^{-7}	2.3×10^{-6}
Venus	$2\frac{GM_\varsigma}{r_\varsigma^3}r$	$GM_\varsigma = 0.82GM_\oplus$	1.2×10^{-10}	3.0×10^{-10}
Indirect oblation	$3\frac{GM_\oplus}{r_\bullet^2}(\frac{R_\oplus}{r_\bullet})^2\frac{M_\bullet}{M_\oplus}\bar{C}_{2,0}$	$GM_\oplus, \bar{C}_{2,0}$	1.4×10^{-11}	1.4×10^{-11}
Dynamic solid tide	$3k_2\frac{GM_\bullet}{r_\bullet}(\frac{R_\oplus}{r_\bullet})^2\frac{R_\oplus^3}{r^4}$	$k_2 \simeq 0.3$	3.9×10^{-8}	1.1×10^{-9}
Dynamic ocean tide	≈ 0.1 of Dynamic solid tide		3.9×10^{-9}	1.1×10^{-10}
Kinematic solid tide	$h\left(\frac{2\pi}{T_{syn\bullet}/2}\right)^2$	$h \simeq 0.30$	5.8×10^{-7}	5.8×10^{-7}
Kinematic ocean loading	$h_L\left(\frac{2\pi}{T_{syn\bullet}/2}\right)^2$	$h_L \simeq 0.05$	9.7×10^{-8}	9.7×10^{-8}
Main GR correction	$\frac{GM_\oplus}{r^2}\frac{GM_\oplus}{c^2}\frac{1}{r}$	$\frac{GM_\oplus}{c^2} = 4.43502804 \times 10^{-3}$	9.8×10^{-10}	6.8×10^{-11}

were characterised by a significant time dependence, due to several phenomena that contribute to the variation of the Earth moments of inertia, with long-period effects of annual and inter-annual periodicity [51–55].

As an example, in Fig.3.2 we show the time evolution of the quadrupole coefficient on a timespan of several years, as obtained by the Center for Space Research (CSR) of the University of Texas at Austin. For this reason, and in accordance with the approaches followed by the LARASE [36] and SaToR-G [56] experiments to model the background gravitational field of the Earth in the case of Fundamental Physics measurements, we use in our PODs for the $\bar{C}_{20}$ coefficient and for the other low-degree harmonics, in particular for the even zonal ones, the values which take into account their time dependence derived from the GRACE [49] and GRACE-FO [50] time-series.

The CSR time series from GRACE Release 06 (R6) are based on monthly estimates. In our POD software, see Chap.4, we substituted to the static values of these coefficients their temporal variation, as approximated by a linear fit to the GRACE and GRACE-FO time series [49, 54]. This temporal dependence of the coefficients of even zonal harmonics affects the prediction provided by the previous Eq.3.6 if based only on a static gravitational field.

This is an element of novelty of our work with respect to previous projects in this field of Fundamental Physics measurements with the current Galileo constellation.

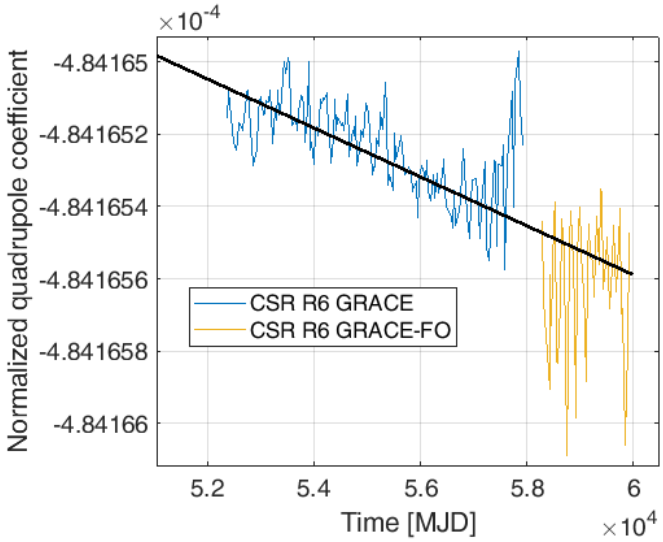

Figure 3.2. *Time dependency of the Earth's quadrupole coefficients has been determined by the CSR analysis centre from GRACE and GRACE-FO data. The black line represents the best linear fit to the data.*

We refer to the International Centre for Global Earth Models (ICGEM): Gravity Field Solutions for dedicated Time Periods (`http://icgem.gfz-potsdam.de/sl/temporal`) for more information on the geopotential time series.

3.2.3 Tidal perturbation

Other celestial bodies exert an acceleration with respect to the Earth as well as with respect to an orbiting satellite around it producing a *tidal effect* on its orbit. This effect is related to the difference between the force on the Earth and that on the satellite [48, 57]. For Earth orbiting satellites, the Sun and the Moon have to be considered while the planetary perturbations are considered, when meaningful, as third-body effects (in Tab.3.1 Venus is reported as provides the largest contribution). These tidal forces also produce permanent and periodic deformations that displace the Earth's crust (*Solid Earth tides*) and also displace water masses (*Ocean tides*).

In general, tidal perturbations affect orbits in three different ways [48]:

1. through kinematic effects, because they cause periodic pulsations and, as a consequence, displacements of the ground tracking stations;

2. through dynamic effects, producing a temporal variation of the geopotential that affects the satellite's orbit;

3. through reference system effects, by perturbing the Earth's rotation and consequently perturbing also the reference system used for orbit determination.

As Tab.3.1 shows, the main tidal term is the kinematic solid tide which produces a symmetrical deformation of the Earth towards the perturbing body (in this case the Moon) and opposite to it. The indirect oblation term in Tab.3.1 results from the Earth's oblateness which affects the motion of the Moon and shifts the centre of mass of the Earth-Moon system with respect to the satellite.

Despite ocean tides account for only $\simeq 10\%$ of the total response to the tidal disturbing potentials, while solid tides account for about 90% of the total response, their uncertainties are a factor of 10 larger than those of solid tides. This is due to their intrinsic complexity, which makes them more difficult to be modeled [58, 59] in the POD software.

If tidal effects were ignored in the satellite POD, the tracking station acceleration would appear as a residual acceleration on the satellite. Since in G4S_2.0 we are interested in the measurement of relativistic effects, let be T the period considered for the analysis of a relativistic effect and P the period of a tidal perturbation. We can divided tidal effects in[2]:

1. tides with $P \leq T$: in this case, even if not modelled, tidal effects tend to average out because they perform full or quasi-full cycles during T.

2. tides with $P > T$: in this case, if the phase and period of the tide are unknown, they mimic a pseudosecular trend, superimposed on the relativistic secular effect. Otherwise, they can be fitted and removed from the residuals.

In general, the Earth's tidal potential U_T, *i.e.* the potential through which the Earth responds to the external tide-generating potential U^* due to the lunisolar gravitational pull, can be expressed in terms of spherical harmonics with a time-variation of the C_{lm} and S_{lm} coefficients, as well as the static geopotential [57, 60]. Specifically, both solid Earth tides and Ocean tides are conventionally modeled as time-dependent corrections, ΔC_{lm} and ΔS_{lm}, to the unnormalized geopotential coefficients.

The solid and ocean tides due to the combined gravitational pull of the Moon and Sun on our planet have a great influence on the orbital elements, in particular on the right ascension of the ascending node Ω and on the argument of pericenter ω [61]. Following the formalism of [47], it is possible to express the tidal potential as functions of the orbital elements in an inertial reference frame, and not as functions of the coordinates (ϕ, λ).

Indeed, within this formalism, in the case of the static geopotential U we have:

$$U = -GM_{\oplus} \sum_{\ell=2}^{+\infty} \sum_{m=0}^{\ell} R_{\oplus}^{\ell} U_{\ell m}, \tag{3.7}$$

where G represents the gravitational constant, $M_{\oplus}$ and $R_{\oplus}$ are, respectively, the Earth's mass and mean equatorial radius and finally the $U_{\ell m}$ represent the components of the potential in the form [47]:

$$U_{\ell m} = \frac{1}{a^{\ell+1}} \sum_{p=0}^{\ell} F_{\ell m p}(\mathrm{i}) \sum_{q=-\infty}^{+\infty} G_{\ell p q}(e) \times$$
$$\left[\begin{pmatrix} C_{\ell m} \\ -S_{\ell m} \end{pmatrix}_{\ell-m \text{ odd}}^{\ell-m \text{ even}} \cos(\psi_{\ell m p q}) + \begin{pmatrix} S_{\ell m} \\ C_{\ell m} \end{pmatrix}_{\ell-m \text{ odd}}^{\ell-m \text{ even}} \sin(\psi_{\ell m p q}) \right], \tag{3.8}$$

where

[2]Naturally this description is general and also applies to other perturbations, particularly to those of non-gravitational origin.

- ℓ, m: degree and order of the expansion in spherical harmonics of the geopotential;
- $C_{\ell m}, S_{\ell m}$: normalised adimensional Stokes coefficients of the geopotential;
- p, q: auxiliary indices of the expansion;
- $\psi_{\ell mpq} \doteq (\ell - 2p)\omega + (\ell - 2p + q)\mathcal{M} + m(\Omega - \theta)$;
- $a, e, \mathrm{i}, \Omega, \omega, \mathcal{M}$: Keplerian elements of the unperturbed orbit, respectively, semi-major axis, eccentricity, inclination, right ascension of the ascending node, argument of pericenter and mean anomaly at epoch;
- $F_{\ell mp}, G_{\ell pqq}$: inclination and eccentricity functions [47, 62, 63];
- θ: Greenwich Sidereal Time.

This allows to consider the potentials as perturbing functions that can be used to evaluate the variations of the osculating orbital elements through the *Lagrange perturbation equations*[3] (see Appendix.A).

This will be addressed in the following sections, where the perturbing tide effect will be derived on the argument of pericenter. This Keplerian element represents one of the main observables for gravitational measurements of G4S_2.0, being subject to both Schwarzschild and Lense-Thirring precession (see §3.2.4). The approach described in [61] will be followed.

3.2.3.1 Solid tides

Applying the Kaula transformation rules, and after several mathematical calculations, we obtain the potential for the combined effects of Moon and Sun [64]:

$$U_{\mathcal{T},\mathcal{S}} = -\frac{GM_\oplus}{R_\oplus^2} \sum_{\ell=2}^{\infty} \left(\frac{R_\oplus}{a}\right)^{\ell+1} \sum_{m=0}^{\ell} A_{\ell m} \times$$
$$\sum_{p=0}^{\ell} F_{\ell mp}(\mathrm{i}) \sum_{q=-\infty}^{+\infty} G_{\ell mq}(e) \sum_f k_{\ell m}(f) H_\ell^m(f) \cos\left(\sigma t + \psi_{\ell mpq} - \epsilon_{\ell m}(f)\right), \tag{3.9}$$

where

$$A_{\ell m} = \sqrt{\frac{2\ell + 1}{4\pi} \frac{(\ell - m)!}{(\ell + m)!}} \tag{3.10}$$

represents the spherical harmonics normalization factor, f is the frequency of a specific tidal contribution term and $\sigma = 2\pi f$ is the so called circular frequency[4]. The coefficients H_ℓ^m are proportional to $(M^*/M_\oplus)(R_\oplus/a^*)^\ell$ and contain the ephemerides information of the Moon and of the Sun. These coefficients represent the amplitudes in the harmonic expansion of the tidal (*i.e.* lunisolar) potential. Finally, $\epsilon_{\ell m}(f)$ represents the phase lag of the solid Earth with respect to the tide constituent of fixed degree ℓ and order m and circular frequency σ that is induced by the Earth's mantle anelasticity.

By using the Lagrange perturbation equations for the argument of perigee ω, with perturbing function given by the potential $U_{\mathcal{T},\mathcal{S}}$ with which the solid Earth responds to the tide generating potential, see Eq.3.9, the amplitude of the periodic perturbation of the perigee at a given degree ℓ in the expansion of the tidal potential and at a given frequency f may be easily computed. We obtain:

[3] In the Lagrange perturbation equations, unlike the Gauss equations used in §3.5.2, the perturbing acceleration is limited to gravitational perturbing accelerations.

[4] The summation over the frequencies f in Eq.3.9 stands for the sum over the integers $j_1, \ldots, j_6$ that define the Doodson number.

$$\Delta\omega_{\ell f} = \frac{GM_\oplus}{R_\oplus^2}\frac{1}{na^2\sqrt{1-e^2}}\sum_{m=0}^{\ell}\left(\frac{R_\oplus}{a}\right)^{\ell+1}A_{\ell m}\times$$
$$\sum_{p=0}^{\ell}\sum_{q=-\infty}^{+\infty}\left[\frac{1-e^2}{e}F_{\ell mp}(\mathrm{i})\frac{dG_{\ell pq}(e)}{de}-\frac{\cos\mathrm{i}}{\sin\mathrm{i}}\frac{dF_{\ell mp}(\mathrm{i})}{d\mathrm{i}}G_{\ell pq}(e)\right]\frac{k_{\ell m}(f)H_\ell^m(f)}{f_p}. \tag{3.11}$$

In these equations, the frequencies f_p and σ are given by

$$f_p = (\ell-2p)\dot\omega + (\ell-2p+q)\dot M + m(\dot\Omega-\dot\theta)+\sigma \tag{3.12}$$

and

$$\sigma = j_1\dot\theta + (j_2-j_1)\dot s + j_3\dot h + j_4\dot p + j_5\dot N' + j_6\dot p_s. \tag{3.13}$$

In last equation, the circular frequency σ has been expressed as function of the following ecliptical angular variables[5]:

- s: mean tropic longitude of the Moon;
- h: mean tropic longitude of the Sun;
- p: mean tropic longitude of the perigee of the Moon;
- N': mean tropic longitude of the node of the Moon;
- p_s: mean tropic longitude of the perigee of the Sun;

and of the integers j_k (with $k=1,...,6$) that define the so called *Doodson number*[6]

$$j_1(j_2+5)(j_3+5).(j_4+5)(j_5+5)(j_6+5) \tag{3.14}$$

representing a given tidal component.

Eq.3.11, is important because it will allow us to estimate the systematic errors produced by the different most significant solid tides on the argument of pericenter of the Galileo satellites in elliptical orbit. This will constitute one of the items that will make up the error budget of the relativistic measurement on this observable.

3.2.3.2 Ocean tides

In the case of ocean tides, the final expression for the potential is:

$$U_{\mathcal{T},\mathcal{O},f} = \sum_{\ell=0}^{\infty}\sum_{m=0}^{\ell}\sum_{+}^{-}\left(\frac{R_\oplus}{a}\right)^{\ell+1}A^{\pm}_{\ell mf}\sum_{p=0}^{\ell}\sum_{q=-\infty}^{+\infty}F_{\ell mp}(\mathrm{i})G_{\ell mq}(e)\times$$
$$\begin{pmatrix}\cos\left(\psi_{\ell mpq}\pm(\sigma t-\epsilon^{\pm}_{\ell m}(f))\right)\\ \sin\left(\psi_{\ell mpq}\pm(\sigma t-\epsilon^{\pm}_{\ell m}(f))\right)\end{pmatrix}^{\ell-m\text{ even}}_{\ell-m\text{ odd}}, \tag{3.15}$$

where

$$A^{\pm}_{\ell mf} = 4\pi G R_\oplus\rho_w\frac{1+k'_{\ell f}}{2\ell+1}C^{\pm}_{\ell mf}. \tag{3.16}$$

[5]In writing Eq.3.13 we have expressed the mean lunar time τ as difference between the sidereal time θ and the mean longitude of the Moon s, so that $\dot\tau=\dot\theta-\dot s$. Notations are conventionally standard: the symbol p is used with different meanings in the two formulas, but there is no risk of ambiguity.

[6]The first index j_1 is used to classify the kind of tide: $j_1=0$ corresponds to long-period or *zonal* tides, $j_1=1$ corresponds to diurnal or *tesseral* tides, finally $j_1=2$ corresponds to semidiurnal or *sectorial* tides.

The quantities $\epsilon^{\pm}_{\ell m}(f)$ represent the phase shift due to the hydrodynamics of the oceans (where the + sign refers to Westwards waves and the − sign refers to Eastwards waves)[7], while the terms $k'_{\ell f}$ and $C^{\pm}_{\ell m f}$ are, respectively, the load Love numbers and the ocean tidal coefficients of the chosen model for the ocean tides.

By the use of the Lagrange perturbing equations for the pericenter rate, we obtain:

$$\Delta\omega_{\ell f} = \frac{1}{na^2\sqrt{1-e^2}} \sum_{m=0}^{\ell} \sum_{+}^{-} \left(\frac{R_\oplus}{a}\right)^{\ell+1} \times$$
$$A^{\pm}_{\ell m f} \sum_{p=0}^{\ell} \sum_{q=-\infty}^{+\infty} \left[\frac{1-e^2}{e} F_{\ell m p} \frac{dG_{\ell p q}}{de} - \frac{\cos i}{\sin i} \frac{dF_{\ell m p}}{di} G_{\ell p q}\right] \frac{1}{f_p}, \tag{3.17}$$

where

$$f_p = (\ell - 2p)\dot{\omega} + (\ell - 2p + q)\dot{M} + m(\dot{\Omega} - \dot{\theta}) \pm \sigma \tag{3.18}$$

and σ is still given by Eq.3.13.

From Eq.3.18 it is clear that in the case of ocean tides the frequencies of the various perturbations are in general different from those of solid tides because of the presence of Eastwards waves. Indeed, for these waves the corresponding negative sign prevents the cancellation of the modulation at the sidereal day $\dot{\theta}$ with the choice $j_1 = m$. Anyway, in the case of the Westwards tidal waves the cited cancellation is still valid, and for the even degree tides we obtain the same long-period effects that we obtained in the case of solid tides.

Again, as in the case of previous Eq.3.11, Eq.3.17 is important because it will allow us to estimate the systematic errors produced by the different most significant ocean tides on the argument of pericenter of the Galileo satellites in elliptical orbit. This will constitute one of the items that will make up the error budget of the relativistic measurement on this observable.

We refer to [57] for further details on tidal terms and their consideration for analyses of satellite orbits around the Earth.

3.2.4 GR model

The main relativistic corrections to the Newtonian equation of motion can be derived from GR geodesic equation applied to the metric tensor $g_{\mu\nu}$ in the weak-field and slow-motion (WFSM) limit of the linearized theory of GR. In particular, a formulation of the relevant equations of motion in a geocentric non–inertial reference system — non–rotating with respect to the barycentric one — is given in [65]. The analysis we follow is consistent with this formulation. The GR acceleration introduced in previous Eq.3.1 is constituted by three terms:

$$\mathbf{a}_{GR} = \mathbf{a}_{Schw} + \mathbf{a}_{dS} + \mathbf{a}_{LT}. \tag{3.19}$$

Therefore, a test mass orbiting around Earth (the Galileo satellite) is subject to these three main relativistic effects. The biggest acceleration is due to the Gravitoelectric field curvature of spacetime induced by Earth mass–energy:

$$\mathbf{a}_{Schw} = \frac{Gm_E}{c^2 r^3}\left[\left(\frac{4Gm_E}{r} - v^2\right)\mathbf{r} + 4(\mathbf{v}\cdot\mathbf{r})\mathbf{v}\right], \tag{3.20}$$

this represents the Schwarzschild (or Einstein) term of the acceleration, and is responsible of the corresponding precession.

The satellite, in its motion around Earth, follows its revolution in the spacetime curved by the Sun mass–energy; this (via parallel transport of the normal to the satellite orbit) induces the *de Sitter* or *geodetic precession*:

$$\mathbf{a}_{dS} = 2\boldsymbol{\Omega} \times \mathbf{v}, \tag{3.21}$$

[7]Where, Westwards waves means waves from East → Weast, and vice-versa in the case of Eastwards waves.

where

$$\mathbf{\Omega} \approx -\frac{3}{2}(\mathbf{V}_E - \mathbf{V}_S) \times \frac{GM_S \mathbf{X}_{ES}}{c^2 R_{ES}^3}. \tag{3.22}$$

In GR, unlike Newtonian physics, mass–energy currents also cause effects, named Gravitomagnetic effects (see [66]). In particular, Earth intrinsic angular momentum curves spacetime and induces a further effect on the satellite orbit, called *Lense–Thirring effect*:

$$\mathbf{a}_{LT} = \frac{2Gm_E}{c^2 r^3}\left[\frac{3}{r^2}(\mathbf{r}\times\mathbf{v})(\mathbf{r}\cdot\mathbf{J}) + \mathbf{v}\times\mathbf{J}\right]. \tag{3.23}$$

In the notation we follow [65], where small letters refers to the geocentric reference frame and capital letters to the solar barycentric one. In particular, c is the speed of light, G the Newtonian gravitational constant, m_E and J are Earth mass and angular momentum, $\mathbf{r}$ and $\mathbf{v}$ the test mass position and velocity in the geocentric frame, M_S is the Sun mass, $\mathbf{V}_E$ and $\mathbf{V}_S$ are the Earth and Sun barycentric velocities, $\mathbf{X}_{ES}$ is the Earth–Sun vector, with distance R_{ES}.

We see that, while the effects described by Eq.3.20 and Eq.3.23 depend only on the Earth mass–energy and mass–energy currents (angular momentum or spin), the de Sitter precession of Eq.3.21 and Eq.3.22 involves also the Sun as third body, *i.e.* a relativistic three–body problem.

The mathematical expressions for the precessions are given by Eqs.3.24–3.26, in the case of Schwarzschild precession and Lense-Thirring precession, and by previous Eq.3.22 for de Sitter precession. The dragging effect manifests itself in a secular shift of the right-ascension of the ascending node (RAAN) Ω and of the argument of pericenter ω of the satellite:

$$\dot{\omega}_{\mathrm{Schw}} = \frac{2+2\gamma-\beta}{3}\frac{3(GM_\oplus)^{3/2}}{c^2 a^{5/2}(1-e^2)}, \tag{3.24}$$

$$\dot{\omega}_{\mathrm{LT}} = -\mu\frac{6GJ_\oplus}{c^2 a^3(1-e^2)^{3/2}}\cos i, \tag{3.25}$$

$$\dot{\Omega}_{\mathrm{LT}} = \mu\frac{2GJ_\oplus}{c^2 a^3(1-e^2)^{3/2}}, \tag{3.26}$$

where a, e and i represent, respectively, the semi-major axis, the eccentricity and the inclination of the orbit, and $J_\oplus$ represents the angular momentum of the Earth. The dimensionless coefficient μ represents the Lense-Thirring effect parameter, with $\mu = 1$ if GR is the correct theory of gravitation, and $\mu = 0$ in Newtonian physics. This coefficient is not a PPN parameter[8]. Conversely, β and γ are PPN parameters, with $\beta = \gamma = 1$ if GR is the correct theory of gravity.

Finally, in Tab.3.2 we reported the numerical values of Schwarzschild (or Einstein) precession [1] on the argument of pericenter, of the Lense-Thirring precession [67] on the right ascension of the ascending node and on the argument of pericenter, and finally of the de Sitter precession [68] on the right ascension of the ascending node for two Galileo FOC satellites and LAGEOS II. Measuring these effects, in the case of Galileo satellites, will be very hard, in particular for the right ascension of the ascending node, because of the smaller relativistic effects and of the larger NGPs.

GR precession	GSAT0201	GSAT0208	LAGEOS II
$\dot{\omega}_{Schw}$	+428.63	+362.72	+3352.58
$\dot{\Omega}_{LT}$	+2.39	+2.18	+31.51
$\dot{\omega}_{LT}$	-5.15	-3.77	-57.33
$\dot{\Omega}_{dS}$	+17.64	+17.64	+17.64

Table 3.2. *Relativistic precessions on GSAT0201 (E18) and GSAT0208 (E08) and their comparison with LAGEOS II. Units are in milli-arcsec per year (mas/yr).*

[8] Parameterized Post Newtonian (PPN) parameters [3, 4].

3.3 Non-Gravitational Perturbations

It is possible to classify the *Non Gravitational Perturbations* (NGP) on Galileo satellites based on their sources: the Sun, the Earth and its environment, the spacecraft itself [30]. While the acceleration due to gravitational forces is independent of the satellite's mass and area, this is not the case of the perturbing surface forces. The area-to-mass ratio (A/M) of the spacecraft is one of the parameters that control the magnitude of the NGP relative to the gravitational perturbations. In the case of an artificial satellite around the Earth this quantity is relatively high, between 0.01 and 0.001 m^2/kg, while it is several orders of magnitude smaller for a natural body [30]. Consequently, in the latter case the NGP are usually negligible but they have to be taken into account in the case of spacecrafts. These perturbations are connected one another and contribute to the perturbed motion of a satellite around the Earth, in a different way. We examine in depth some aspects in the following sections.

3.3.1 NGPs due to the Sun

The interaction between the visible solar radiation with a satellite can produce different physical effects that can be classified as:

- direct solar radiation pressure
- Yarkovsky-Schach effect
- Asymmetric reflectivity
- Poynting-Robertson effect.

The *direct solar radiation pressure* (SRP) is the major perturbation on the orbit of a Galileo satellite ($\sim 10^{-7}$ m/s^2), as well as on all GNSS satellites. The perturbation consists in a net acceleration resulting from the interaction (*i.e.* absorption, reflection or diffusion) of the solar light with each elementary surface of the satellite. Each photon has momentum $p = E/c$ that can be exchanged during the interaction with a solid surface. This results in a momentum transfer to the satellite.

Let be α, ρ, δ the absorption, reflection and diffusion coefficients of an elementary surface dA, respectively. They are constrained by the following equation:

$$\alpha + \rho + \delta = 1\,. \tag{3.27}$$

Assuming the following simplifying assumptions:

- the absorbed light is not re-emitted;
- the intensity of diffused light, for a given direction, is proportional to the cosine of the angle with the unit vector $\mathbf{n}$ perpendicular to dA;
- the reflection is perfectly specular;

we obtain the following expression for the total elementary acceleration by the incident solar radiation [48]:

$$d\boldsymbol{a} = -\frac{\phi_\odot}{mc}\left[(1-\rho)\hat{\boldsymbol{e}}_{\boldsymbol{D}} + 2\left(\frac{\delta}{3} + \rho cos\theta\right)\hat{\boldsymbol{n}}\right] dA|cos\vartheta|\,, \tag{3.28}$$

where $\phi_\odot$ is the solar irradiance, m is the mass of the satellite, c is the speed of light, $\hat{e}_D$ is the unit vector directed towards the Sun from the spacecraft center of mass. Finally $\hat{n}$ represents the unit vector normal to the surface and ϑ the angle between $\vec{n}$ and the unit vector $\hat{\boldsymbol{e}}_{\boldsymbol{D}}$, such as $cos\vartheta = \hat{\boldsymbol{e}}_{\boldsymbol{D}} \cdot \hat{\boldsymbol{n}}$. In other words, we assume that each surface dA behaves like a linear combination of an ideal black body, a perfect mirror and a perfect diffuser. In these conditions, Eq.3.28 is the resultant acceleration of the elementary accelerations $d\boldsymbol{a}_{\boldsymbol{\alpha}}$, $d\boldsymbol{a}_{\boldsymbol{\rho}}$, $d\boldsymbol{a}_{\boldsymbol{\delta}}$ which are caused on dA by the absorbed, reflected and diffused sunlight respectively. Thus, we can calculate the total effect of SRP on the satellite by decomposing the spacecraft surface into a finite number of elementary surfaces whose optical properties are assumed to be known. Then, according to Eq.3.28, the total

elementary acceleration is calculated for each elementary surface, at any time and for a given position of the satellite with respect to the Sun. Finally, the total solar radiation perturbation vector, acting on the satellite, is derived as the sum of the all elementary accelerations.

We underline that we avoid the assumption that the absorbed radiation is re-emitted as "thermal" radiation [30]. This is due to a plethora of effects of different origins and acting on the satellite with accelerations of the order of 10^{-10} m/s^2. Therefore, these effects can only be taken into account after adequate modelling not only the direct solar radiation, but also the terrestrial albedo and the infrared radiation pressure (see §3.3.2).

The *Yarkovsky-Schach effect* is characterised by an anisotropic emission of thermal radiation resulting from temperature gradients across the satellite surface. Such gradients are created by solar heating and the thermal inertia of satellite elements. This effect produces a resulting perturbation acceleration and long-term effects on the orbit due to the modulation of the thermal radiation by eclipses. However, in the literature of GNSS, this effect is considered as part of the thermal re-rediation from the satellite. This effect is well known in the case of the two LAGEOS satellites [69, 70]

The *asymmetric reflectivity* is due to possible difference in reflectivity of the various satellite elements. This effect was well investigated in the case of LAGEOS satellites [71, 72]

Regarding the *Poynting-Robertson* effect [69], it can be explained as follows: we assume that the re-emission of the absorbed photons by the satellite is isotropic in its own reference frame so, the photons emitted in the direction of motion are blue-shifted due to Doppler effect. This implies that they carry away more momentum than the photons emitted in the opposite direction. The result is a net deceleration force acting on the satellite.

In Tab.3.3 the values of the main non-gravitational accelerations on the Galileo-FOC satellites are reported and, for comparison, on the LAGEOS II satellite. As mentioned before, the SRP is the largest perturbation and, consequently, it represents the main source of error in determining the orbit of any GNSS spacecraft. Building a sufficiently accurate model of the SRP is therefore indispensable to seriously consider smaller perturbation effects, such as those related to terrestrial radiation and thermal thrust effects (see Tab.3.3). In fact, to properly account for thermal effects (whatever their origin, internal or external), we need to model the direct SRP better than 1%, down to 0.1%. Since the POD needs the dynamical model (as we will see in §4.1), then more accurate orbits can be derived with the aforementioned improvements. As a consequence, the scientific objectives of the G4S_2.0 project can benefit from the satellite dynamical model enhancements and from the corresponding POD, since they play a key role to perform measurements in the field of Fundamental Physics. Geodetic and geophysical applications and International GNSS Service (IGS)[9] products will also be significantly affected.

We will focus on our model for the acceleration produced by the direct SRP on the satellite in §3.5, showing its effects on the satellite's orbital elements and some considerations that we can derive for future measurements.

3.3.2 Other NGPs

The perturbations due to the Earth and its environment can be identified in

- Albedo
- Infrared radiation pressure
- Neutral and charged particle drag
- Earth-Yarkovsky effect

The main effect on the satellite's orbit, among those discribed in this paragraph, is due to *Earth's albedo* (*i.e.* the indirect solar radiation pressure). This is the strongest perturbation after the direct SRP. The solar radiation reflected from a surface element on the Earth is not isotropic (*i.e.* not symmetrically distributed around the local zenith) and produces long-term effects on the satellite orbit. The complexity of these effects is mainly related to the asymmetry between the Earth's northern and southern hemispheres, resulting both from the different sea/land distribution and from seasonal phenomena (*e.g.* cloud and snow cover).

[9] https://igs.org/

Table 3.3. *Comparison of the main non-gravitational accelerations (S.I.units) on LAGEOS II with the corresponding accelerations on a Galileo FOC satellite. The symbol (-) means that the acceleration is negligible, while the symbol (NA) means that the acceleration is currently unknown (not available), since it has not yet been evaluated.*

Physical effect	Formula	Parameter [S.I. units/adim.]	LAGEOS II	Galileo FOC
Direct SRP	$C_R\frac{A}{m}\frac{\Phi_\odot}{c}$	$\Phi_\odot = 1360.8$	3.2×10^{-9}	1.0×10^{-7}
Earth's Albedo	$2\frac{A}{m}\frac{\Phi_\odot}{c}A_\oplus\frac{\pi R_\oplus^2}{4\pi r^2}$	$A_\oplus \approx 0.3$	1.3×10^{-10}	7.0×10^{-10}
Earth's Infrared radiation	$\frac{A}{m}\frac{\Phi_{IR}}{c}\frac{R_\oplus^2}{r^2}$	$\Phi_{IR} \approx 240$	1.5×10^{-10}	1.1×10^{-9}
Neutral drag	$\frac{1}{2}C_D\frac{A}{m}\rho V^2$	$C_D \simeq 4.0, \rho \approx 5.7 \times 10^{-18}$	2.6×10^{-13}	–
Charged drag	see Chap.5 in [74]	Species densities, floating potential	2.0×10^{-12}	NA
Power from antennas	$\frac{P}{mc}$	$P = 265$		1.2×10^{-9}
Thermal effect solar panels	$\frac{2}{3}\frac{\sigma}{c}\frac{A}{m}(\epsilon_1 T_1^4 - \epsilon_2 T_2^4)$	$\epsilon_1 \simeq \epsilon_2 \approx 0.8, T_1 \simeq 317, T_2 \simeq 318$		1.9×10^{-10}
Poynting Robertson	$\frac{1}{4}\frac{A}{m}\frac{\Phi_\odot}{c}\frac{R_\oplus^2}{r^2}\frac{v}{c}$	$\Phi_\odot = 1360.8$	4.2×10^{-15}	1.9×10^{-14}
Solar Yarkovsky-Schach	$\frac{16}{9}\frac{A}{m}\frac{\epsilon\sigma}{c}T_0^3\Delta T$	$\epsilon, T_0\Delta T$	1.0×10^{-10}	NA
Earth Yarkovsky	$0.41\frac{4}{9}\frac{A}{m}\frac{\epsilon\Phi_{IR}f_0}{\alpha c}\frac{R_\oplus^2}{r^2}$	$\Phi_{IR} \approx 240, f_0 \approx 0.30, \alpha \approx 1.789$	2.5×10^{-11}	NA

The *infrared radiation* (IR) *pressure* is due to the Earth's temperature, and its effects are comparable with those of the albedo. In order to calculate the perturbing accelerations from these two effects, we use a dataset from CERES (Clouds and the Earth's Radiant Energy System)[10] data provided on the top of the atmosphere. The region of the satellite's field of view is divided into spherical sectors, and for each sector the radiation emitted is calculated for terrestrial infrared radiation and albedo. This is computed for each satellite position.

The *neutral drag perturbation* is due to the collisions between the satellite cross-section and particles of the Earth's atmosphere, along its trajectory. Moreover, as a consequence of the Earth's magnetic field, there could be a *charged drag* due to the Coulomb interaction between charged particles (trapped by the Earth's magnetic field) and the charged satellite. Since the atmospheric density decreases exponentially with increasing height, the neutral drag mainly affects the low-Earth satellites. Therefore, in the case of the Galileo-FOC it can be neglected because of their higher altitude. Regarding the charged drag it seems that this effect has never been considered in the GNSS literature [30].

The *Earth-Yarkovsky effect* is the anisotropic emission of thermal radiation due to temperature gradients produced by the Earth's infrared radiation [73].

Moreover, an active satellite is itself responsible for the production of NGPs of thermal origin. The main effects are:

- Radiation of thermal blankets
- Radiation from radiators
- Solar panels thermal radiation
- Antennas radiation
- Manoeuvres

Within the G4S_2.0 project there is no intention to consider thermal effects on the basis of simple re-radiation, as is usually done in the GNSS literature. A reliable model for both direct and indirect SRP is a fundamental requirement for effectively addressing the modelling of all types (*i.e.* external and internal) of thermal effects acting on the satellite. In this regard, knowledge of the temperature distribution and its gradients inside the spacecraft is of fundamental importance [75–77]. Of course, taking such effects into account would refine the spacecraft dynamical model. However, these effects are responsible for perturbing accelerations up to 10^{-10} m/s^2 (see Tab.3.3). Therefore, they can only be taken into account after adequate modelling of not only the SRP, whose perturbing maximum acceleration is of the order of 10^{-7} m/s^2, but also the terrestrial albedo and the infrared radiation pressure, as as previously highlighted. In this respect, we emphasise the importance of building an accurate SRP model with the aim to reach 1% down to 0.1% levels in accuracy which is not a straightforward issue.

In conclusion, there is a wide range of perturbing accelerations that act on the satellite motion and are responsible for temporal variations of the orbital elements. They can be divided in two groups: those of gravitational and those of non-gravitational origin. The latter are further classified according to the source of the perturbation (the Sun, the Earth and the spacecraft itself). The choice of which perturbing acceleration could be neglected depends on the precision that can be achieved in the satellite's POD. This depends on the accuracy of satellite position measurements based on tracking observations and on the overall dynamical model exploited in the POD software. Nowadays, a significant increase in accuracy of tracking measurements of the satellite has been achieved, for both microwave and laser measurements. However, the level reached is not sufficient for Fundamental Physics measurements, as the complex and subtle effects of the NGPs over relatively long periods can "mask" the relativistic effects of the secular type. The main challenge is therefore to improve the dynamical model for the various perturbations. As already mentioned, the primary focus is to enhance the SRP model, since it is the largest perturbation and the main source of error in orbit modelling. This would allow albedo and IR radiation pressure effects to be properly taken into account, as they are two orders of magnitude lower than the SRP. The G4S_2.0 activities, which aim to achieve the ambitious objectives in the field of Fundamental Physics measurements, are going in this direction.

[10] https://terra.nasa.gov/data/ceres-data

3.4 Current Models for the Non-Gravitational Perturbations

Coping with NGPs modelling can be solved twofold by:

- developing a refined model of the spacecraft in such a way to describe the physical interaction between each element of the spacecraft and the perturbation source. The POD will then make use of the calculated perturbing accelerations for data reduction.
- studying the NGPs effects along the satellite orbit in order to understand which component of the perturbation is significant. Based on this information, an analytical model is developed to be used in the POD procedure for data reduction.

The second approach, which is the most adopted in the NGPs literature, is characterised by some fixed parameters of the model or by some estimated parameters in the POD (*i.e.* the radiation coefficient C_R[11] or the drag coefficient C_D[12]). Sometimes, *empirical accelerations* are used in the parameter-estimation to compensate some deficiencies in a priori models [42, 78–80]. However, the use of empirical accelerations "attenuates" the full effect of the perturbing accelerations and should therefore be avoided whenever the correct physical description of the phenomena is required.

Developing a simplified analytical model, *i.e.* a Simplified Box-Wing (S-BW) model, best represents the second approach described above. Assuming the optical coefficients of each surface are known, with the S-BW model we can calculate the SRP accelerations acting on it. At the same time, the development of a S-BW model is also a first step towards the realisation of the first approach mentioned above, *i.e.* the development of a *Finite Element Model* (FEM) of the satellite.

The current models for NGPs can be summarised in the following typologies (also in chronological order of their development):

1. Cannonball
2. Empirical accelerations
3. S-BW
4. BW
5. BW with adjusted coefficients
6. FEM

In the case of a GNSS spacecraft, the *cannonball model* is a very rough solution to account for the satellite's shape, as it is approximated as a sphere. When applied to the SRP, it models the average cross-section as seen by the Sun with average optical coefficients parameterised by a radiation coefficient, C_R. Due to its extreme simplification, it has usually been used as an a priori model with the addition of estimates of empirical terms. In Chap.4, §4.2, we illustrate the results obtained by performing a preliminary POD for Galileo FOC satellites with a cannonball model, although it is a very simplified model. Then, in §4.2.1, we will show the results obtained by inserting our Box-Wing model in the POD.

Regarding *empirical models*, in [42] the Empirical CODE Orbit Model (ECOM) is introduced: the accelerations are represented by a constant and two periodic once-per-revolution accelerations (sine and cosine terms) along the three directions in the Sun–Satellite–Earth (SSE) reference frame. So, the SRP acceleration is modeled as:

$$\boldsymbol{a}_{\odot} = \boldsymbol{a}_{\odot,0} + D(u)\hat{\boldsymbol{e}}_{\boldsymbol{D}} + Y(u)\hat{\boldsymbol{e}}_{\boldsymbol{Y}} + X(u)\hat{\boldsymbol{e}}_{\boldsymbol{X}} \,. \tag{3.29}$$

The first term, $\boldsymbol{a}_{\odot}$ represents the acceleration given by an a priori model for the SRP, $\hat{\boldsymbol{e}}_{\boldsymbol{D}}$ is the unit vector from the spacecraft center of mass to the Sun, $\hat{\boldsymbol{e}}_{\boldsymbol{Y}}$ is the unit vector along the spacecraft solar panel axis, $\hat{\boldsymbol{e}}_{\boldsymbol{X}} = \hat{\boldsymbol{e}}_{\boldsymbol{D}} \times \hat{\boldsymbol{e}}_{\boldsymbol{Y}}$ defines a right-handed system. Finally, u is the

[11] This quantity parameterised the average optical coefficients of a surface.
[12] This coefficient is used to quantify the drag or resistance of an object in a fluid environment.

spacecraft argument of latitude ($u = \omega + f$), with ω the argument of pericenter and f the true anomaly. $D(u)$, $Y(u)$ and $X(u)$ are the empirical accelerations. They are decomposed as:

$$\begin{cases} D(u) = D_0 + D_s \sin(u) + D_c \cos(u) \\ Y(u) = Y_0 + Y_s \sin(u) + Y_c \cos(u) \\ X(u) = X_0 + X_s \sin(u) + X_c \cos(u) \end{cases} \tag{3.30}$$

Therefore, this model is characterised by nine parameters that can be estimated over a fixed period to absorb the part of the SRP perturbation that is not modelled [81]. An extended ECOM2 was proposed in [44]. The ECOM2 model includes even periodic terms in the direction of the Sun (currently twice per revolution) and odd periodic terms along the X axis (currently once per revolution), in addition to a constant acceleration along each of the above axes. Finally, the acceleration along the Y axis is simply given by a constant contribution. As a consequence, ECOM2 is expressed as follows:

$$\begin{cases} D(u) = D_0 + \sum_{i=1}^{n_D} \{D_{2i,c} \cos(2i)\Delta u + D_{2i,s} \sin(2i)\Delta u\} \\ Y(u) = Y_0 \\ B(u) = B_0 + \sum_{i=1}^{n_B} \{B_{2i-1,c} \cos(2i-1)\Delta u + B_{2i-1,s} \sin(2i-1)\Delta u\} \end{cases} \tag{3.31}$$

where we have introduced the symbol B instead of X, in accordance with the notations of [44], and where the argument of the latitude of the satellite with respect to that of the Sun $\Delta u = u - u_\odot$ has replaced the argument of the latitude u of the satellite. It is important to emphasise that the B axis does not (in general) coincide with an axis of the spacecraft.

We have already emphasised the positive role of empirical terms to absorb unknown effects, but at the cost of losing the physical content of some perturbing effects. This is positive for positioning, as the orbital residuals can be reduced, but not adequate for other GNSS applications, such as Geophysics or Fundamental Physics where a comprehensive knowledge of the physical perturbation is required. For GNSS positioning the main objective is to reduce the POD residuals of the satellites by exploiting the modelling of the direct SRP, currently with a BW, and absorbing the other effects as much as possible by introducing ad hoc empirical terms, which however have the primary objective of absorbing the unmodeled part of the SRP not considered by the BW model [30]. Instead, our interest is different: we aim to study the effects of the SRP on the satellite orbital elements in order to derive physical information about the Fundamental Physics measurements we want to perform. Of course, we also want to reduce the POD residuals on the orbital elements but without losing physical information on the phenomena, *i.e.* without introducing the empirical accelerations, but instead improving the SRP dynamical model to a new level of accuracy.

As previously anticipated in §2.2.2, the *Box-Wing* (BW) model is a simplification of the complex structure of a satellite by assuming a parallelepiped/cuboid body (Box) and two flat surfaces (Wings) of the solar panels. On the assumption that each surface dA behaves as a linear combination of a black body, a perfect mirror and a perfect diffuser (with the corresponding optical coefficients α, ρ and δ such as $\alpha + \rho + \delta = 1$), we obtain Eq.3.28 which is the acceleration due to direct SRP. The introduction of a BW simplifies the SRP acceleration calculation from an elementary-surface model to a (parameterised) model with geometric properties (box and wings shape) as boundaries. The acceleration, according to Eq.3.28, is calculated for each surface of the box and of the panels, assuming that the corresponding optical parameters are known.

Such models have been developed in [43] for GPS satellites. There are also many examples of BW models for the GNSS, such as the one in [82] on the basis of ESA Galileo Metadata. We also developed a BW model on the basis of these data, so we refer to it as a "Simplified" Box-Wing (S-BW). Our results are reported in the following paragraph.

A refined *Finite Element Model* is characterised by the following features:

1. a very accurate representation of the complex geometry of the spacecraft;
2. the knowledge of the physical characteristics - such as optical (in the visible and in the infrared) and thermal - of each type of surface and element (antenna, appendices, CCR, insulators, radiators, etc.) that constitute the spacecraft, also including the internal ones;

3. the knowledge of the time variations of these characteristics (especially the optical ones) and how they depend, for istance, on the illumination conditions;

4. taking into account multiple reflections;

5. the knowledge with high accuracy of the spacecraft attitude with respect to the Earth and to the manoeuvres;

6. for a given attitude, it is necessary to model the mutual shadowing effects produced by the spacecraft surfaces and appendices, in order to account for umbra and penumbra effects.

Developing and successfully using a sophisticated and complete spacecraft FEM based on Ray-Tracing is therefore a daunting task. In fact, this first approach in modelling has not been pursued until recent years, due to the many complexities mentioned above and also due to the time-consuming of numerical integrations required to perform all the detailed interactions, which must include multiple reflections, with umbra and penumbra calculations, knowledge of the optical properties of the surfaces, and the correct satellite attitude in space. However, since the last two decades, it is now possible to perform a satellite FEM to improve the modelling of NGPs, starting with the SRP, using a normal personal computer, thanks to improvements in computing power and the development of algorithms and dedicated software for Ray-Tracing techniques or the Test Particle Monte Carlo (TPMC) approach [83–86].

Although the key elements of developing a reliable FEM are well described in the literature [43, 87–96] it appears that a refined FEM has never been developed, tested and routinely applied in the POD of GNSS satellites.

In the context of G4S_2.0 project, we aim to build a FEM for the Galileo-FOC satellites to derive the perturbing accelerations arising from the interaction of each surface element with external and internal radiation sources. Moreover, we aim to employ the Ray-Tracing technique to properly take into account multiple reflections and mutual shadowing effects. Achieving this complex task, will allow us to improve the POD and, consequently, G4S_2.0 scientific results.

In general, the main benefits that can be achieved by using a FEM are [30]:

1. avoiding the extensive use of empirical parameters currently used in the POD through the use of new high accuracy numerical model that includes the perturbing effects of direct SRP;

2. better modelling of perturbing effects which are two orders of magnitude lower in acceleration than SRP, such as the Earth's albedo and infrared radiation pressure;

3. a better and more detailed consideration of the numerous thermal effects due to the radiation emitted by the spacecraft surface, if the anisotropic temperature distribution is known;

4. it would hopefully allow, under favourable conditions, to take into account the perturbing effects associated with variations in solar irradiation (we refer to [30] for more details on this aspect).

5. better predictions (both directly and indirectly) for the orbits generated by IGS and by the main Analysis Centres;

6. more precise and accurate POD for Fundamental Physics measurements exploiting GNSS satellites.

On the first point, as previously anticipated, reducing the use of empirical accelerations avoids mitigating the effects of perturbing accelerations. Consequently, the measurement of a physical effect can certainly benefit from this.

In particular, the use of empirical terms would be restricted to thermal effects if FEM were successfully applied to modelling the effects of radiation pressure from the Earth-atmosphere system, the second point above.

On the third point, if we have a good knowledge of the anisotropic temperature distribution on the surface of the spacecraft and its elements (also taking into account its interior, with heat transport and radiation mechanisms of the spacecraft structure), it would be possible, in

principle, to calculate the elementary acceleration from each surface element. In this way, the total acceleration produced by the radiation from the surface of the spacecraft can be calculated. We refer to [93] as a very good example in this direction.

Regarding the fifth point, we stress the fact that the development of a reliable FEM model is also important for the IGS orbits predictions, *i.e.* orbit propagation, since their final accuracy depends strongly on the quality and reliability of the SRP model.

Finally, once a FEM is implemented the a-posteriori analysis of the orbits is simpler than the one required to obtain the IGS orbits. In this context, it will be important to correctly define the length of the orbital arc of the POD of the considered satellites. This will depend both on the relativistic effect, which is the subject of our analysis from time to time, and on the number of observations available. In addition, it will also be relevant to explore the possibility of inserting the perturbing accelerations obtained from the FEM in the typical GNSS POD procedures to better characterise the spacecraft dynamical model.

In the Fundamental Physics context, a FEM for a Galileo FOC satellite has already been developed by ZARM [18] and SYRTE [97] for the measurement of the gravitational redshift [18, 19]. Indeed, a FEM of a Galileo FOC has been developed by ZARM and the results for the SRP have been used by ESA in their POD for the measurement of the gravitational redshift performed in 2018 [18], but no results had been published at the time of this measurement[13] and no mention of the FEM is reported in [18]. The FEM model developed by ZARM was published only in 2023 [98]. This model has good performance, well superior to those of a S-BW, but cannot be considered a refined FEM of the Galileo FOC satellite since not based on sufficiently detailed information regarding the optical properties of the various components of the satellite and also not having any information on the temperature distribution on the satellite[14]. As a consequence, the accuracy that can be achieved with a FEM for the modelling of the SRP for a Galileo FOC satellite has not yet been defined. However the FEM model described in [98] is remarkable in several aspects.

In conclusion, several models have been developed to explain the main perturbations affecting GNSS satellites. The main challenge is to build a refined FEM model that would lead in the future to several advantages in NGPs modelling and in Fundamental Physics applications.

3.5 The G4S_2.0 models for the NGPs

As mentioned in §2.2.2, the information contained in the ESA Galileo Metadata is not sufficiently detailed for the development of a FEM. This will be our ultimate goal in G4S_2.0 but, as an intermediate step, we developed a S-BW model, based on the available information by ESA, as well as a 3D-CAD of a Galileo FOC satellite.

Already with this model, new results have been achieved: the study of the SRP effects on the Keplerian elements and the comparison of these predictions in the orbital elements with the corresponding orbital residuals obtained with a POD (see Chap.4).

Firstly, in §3.5.1 we show the results for the accelerations produced by the SRP on GSAT0201 and GSAT0202 satellites in elliptical orbits, obtained by applying our S-BW developed with `Matlab`. In §3.5.2 we then explain the long-term SRP perturbing effects on the Keplerian elements. Finally, we refer to §4.1.1.1 for the `GEODYN II` POD residuals compared with our S-BW model predictions of the Keplerian elements.

3.5.1 S-BW results: Long-term analysis of the SRP acceleration

The SRP modelling is given by Eq.3.28 and the relative assumptions. The application of our S-BW takes into account a period of 2-years starting from the launch of the satellites, see Tab.2.3. An integration step of 120 s has been used. The eclipses have been modeled with a conical shadow model for a spherical Earth, in such a way to consider penumbra effects [33]. We also considered the variation of the mass of the satellites, when it occurs, as reported by the ILRS, see Tab.3.4.

[13] Benny Rievers personal communication
[14] Benny Rievers personal communication

Satellite	Time interval	Mass [kg]	Time interval	Mass [kg]
GSAT0201	August 22, 2014	660.977	-	-
GSAT0202	August 22, 2014 to July 30, 2015	662.646	July 31, 2015 to onward	662.141

Table 3.4. *Mass values for Galileo satellites FOC GSAT0201 (E18) and GSAT0202 (E14). These values for satellite masses are current as of 2022-12-20.*

Satellite	$a[m]$	e	$I[^\circ]$	$\Omega[^\circ]$	$\omega[^\circ]$	$M[^\circ]$
GSAT0201	27978099.66	0.1604	50.369	53.505 -0.04000414086	50.184 +0.04910776939	316.069 +667.909221051
GSAT0202	27977624.83	0.1608	50.309	52.459 -0.04002923721	52.086 +0.04784293004	136.069 +667.909221051

Table 3.5. *Orbital elements for the Galileo FOC satellites GSAT0201 (E18) and GSAT0202 (E14) estimated from the Precise Orbits of ESOC. The reference date for the satellites is 2016-11-21 at 00:00:00 UTC. The rates of the angular variables are in degree/days [°/d].*

Regarding the Keplerian orbital elements, we refer to Tab.3.5, since those reported in Galileo Metadata seem to be very inaccurate except for the mean anomaly M. Therefore, a transformation from the terrestrial rotating reference frame to the J2000.0[15] inertial one was performed on the ESOC state-vector. This state-vector was finally transformed into the corresponding six Keplerian elements. Finally, from the temporal evolution of the elements we estimated their corresponding rate.

First, we computed the variation of the Sun's height $\beta_\odot$ with respect to the orbital plane of GSAT0201 together with its attitude law Ψ (see Fig.3.3 and Fig.3.4). It is evident that the time evolution of the attitude law is characterised by a long-term evolution mainly related to the satellite's draconic year and by higher frequency evolutions, mainly at the satellite's orbital period. This is useful for understanding the behaviour of the SRP over time.

We then used our S-BW to calculate the perturbing accelerations due to the SRP. The corresponding results are shown in two different reference frames. Fig.3.5 shows the acceleration in the DYB frame of the spacecraft, which is also known as the Sun-Satellite-Earth (SSE) reference frame already introduce in 3.4. We reiterate that the D-axis is defined by the unit vector $\hat{\boldsymbol{e}}_{\boldsymbol{D}}$, $\hat{\boldsymbol{e}}_{\boldsymbol{Y}}$ is the unit vector along the spacecraft solar panel axis and defines the Y-axis, finally $\hat{\boldsymbol{e}}_{\boldsymbol{B}} = \hat{\boldsymbol{e}}_{\boldsymbol{D}} \times \hat{\boldsymbol{e}}_{\boldsymbol{Y}}$ defines a right-handed reference system and the corresponding B-axis. The interaction of the direct SRP with the solar panels, which are always orthogonal to the incident solar radiation except during the eclipses-periods (as described in §2.5), explains the overwhelming contribution of the acceleration along the D-axis. The interaction of the solar radiation with the spacecraft's bus surfaces contributes when the various contributions are projected along the D-axis. As can be deduced from this figure, the maximum accelerations (in absolute value) along the D-axis are about two orders of magnitude greater than the accelerations along the B-axis. In fact, the behaviour of the acceleration along the D-axis is very close to that of the absolute value of the direct SRP on the S-BW model, see Fig.3.6. Regarding the acceleration along the Y-axis, it is non-zero only during the eclipse season according to the attitude-law previously described.

For our purposes, visualizing the SRP perturbing accelerations in the Gauss co-moving reference frame $(\hat{\boldsymbol{r}}, \hat{\boldsymbol{t}}, \hat{\boldsymbol{w}})$ is also important, see Fig.3.7. Indeed, its introduction allows to express the perturbation effects of the modeled SRP in the so-called *Gauss perturbing equations* in order to estimate their impact on the satellite orbital elements, see §3.5.2. In this frame co-rotating with the satellite revolution around the Earth, the radial direction $(\hat{\boldsymbol{r}})$ is identified by the direction from the Earth's center of mass to the satellite center of mass. The out-of-plane or cross-track direction $(\hat{\boldsymbol{w}})$ is identified by the obsculating angular momentum direction. Finally, the transverse direction $(\hat{\boldsymbol{t}})$ is defined in such a way to define a right-handed reference system: $\hat{\boldsymbol{t}} = \hat{\boldsymbol{w}} \times \hat{\boldsymbol{r}}$. As we can see from Fig.3.7, the radial R and transverse T accelerations have a similar behaviour and magnitude. The maximum values for the out-of-plane W accelerations are slightly smaller and

[15]The current reference standard epoch for the scientific community.

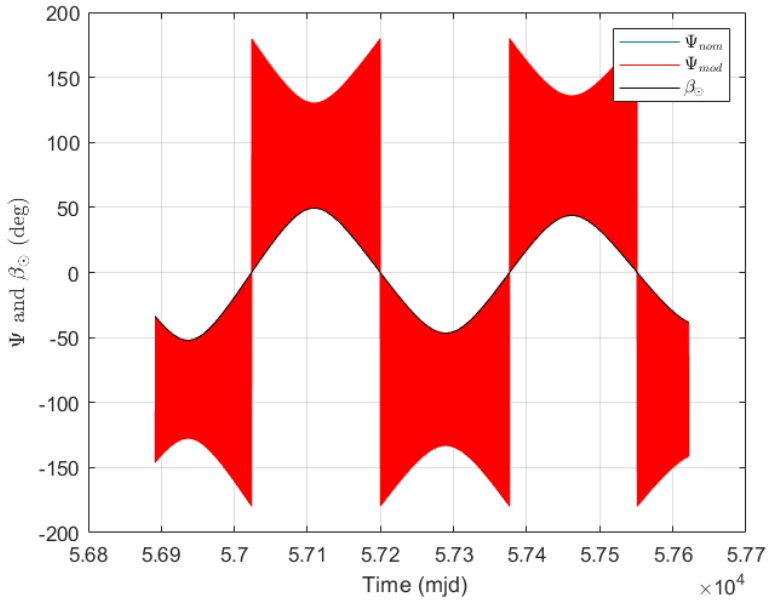

Figure 3.3. *GSAT0201 (E18): Nominal (blue) and modified (red) attitude law. Four eclipse seasons are shown. The starting epoch corresponds to August 23, 2014.*

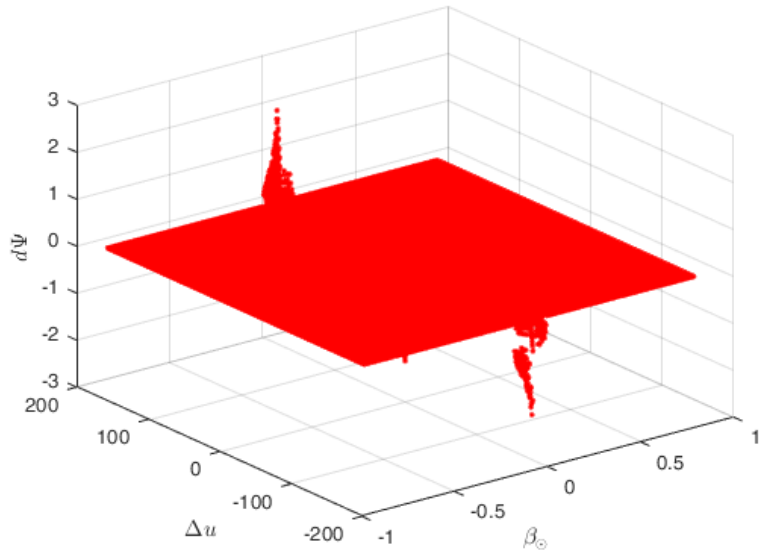

Figure 3.4. *GSAT0201 (E18): 3D-plot of the difference between the nominal attitude law and the modified attitude law as a function of the satellite position on the orbit with respect to the Sun (Δu) and of the solar height on the orbital plane ($\beta_\odot$). As we can see $d\Psi$ is always zero except when $\beta_\odot$ is close to* $0°$ *($|\beta| \leq 4.1°$) and $\Delta u \cong \pm 180°$.*

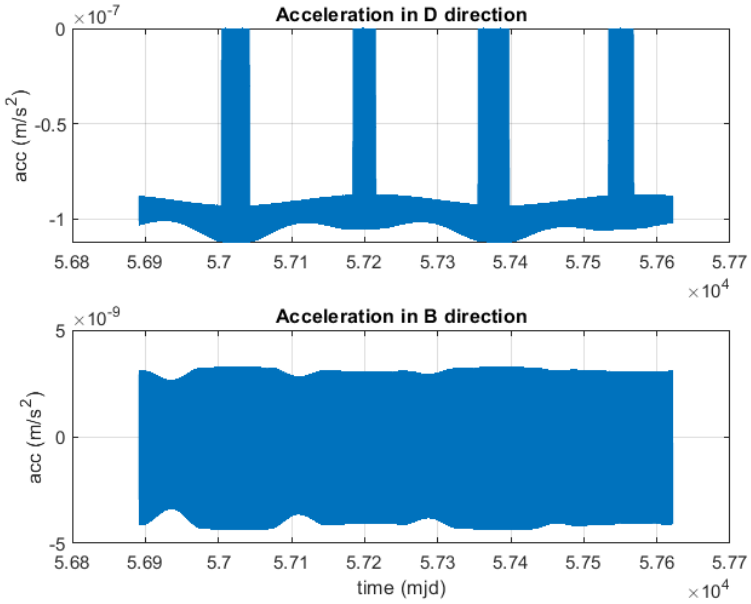

Figure 3.5. *GSAT0201 (E18): acceleration due to the direct SRP along the D (top) and B (bottom) directions.*

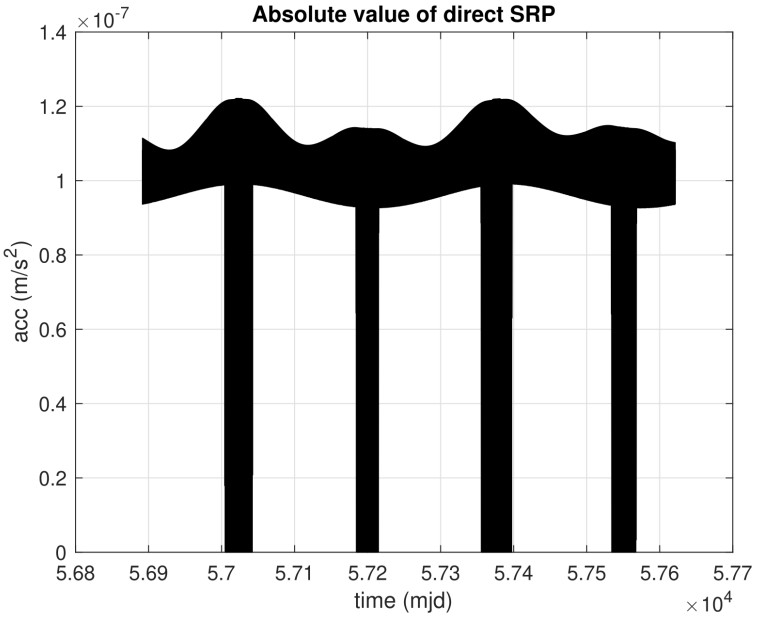

Figure 3.6. *GSAT0201 (E18): absolute value of the acceleration due to the direct SRP.*

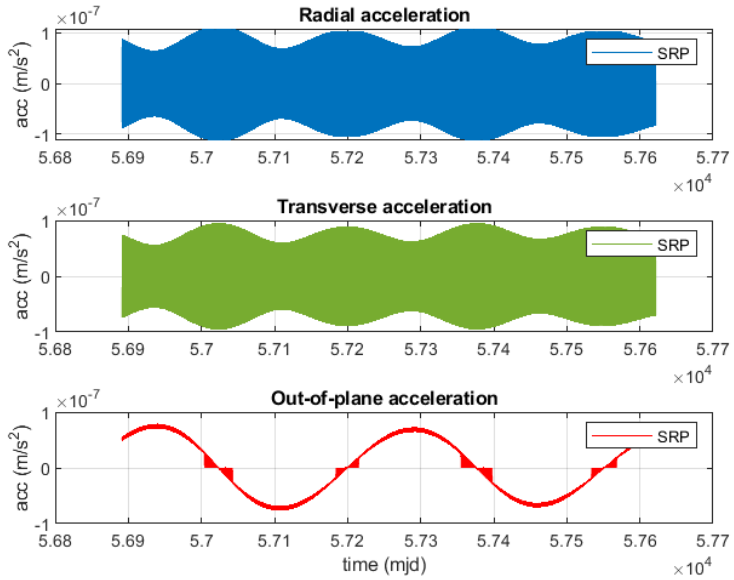

Figure 3.7. *GSAT0201 (E18): acceleration due to the direct SRP along the directions of the Gauss co-moving frame.*

their long-term behaviour is clearly modulated by the variation of the Sun height with respect to the orbital plane. This long-term modulation is also present for the other two components, but for these components the modulation of the acceleration at the orbital period assumes a clear and evident importance. In Fig.3.8 and in Fig.3.9 we compare these three components of the direct SRP in two very different conditions for the Sun height $\beta_{\odot}$: during a few eclipses (where the solar height is very close to zero) and far way from the eclipses (where the solar height is very close to its maximum value). Obviously, in the first case the out-of plane component of the SRP acceleration is practically zero and its effects on the orbital elements are completely negligible. Conversely, in the second case the out-of-plane component is almost constant and larger than the other two components. Finally, the radial and transverse components show a similar behaviour in both cases, as already anticipated.

We apply to the GSAT0202 part of the analysis already carried out on the GSAT0201 satellite. In fact, the results are similar because the two satellites in elliptical orbit have very close average orbital parameters and are on the same auxiliary orbital plane. For this reason, we will focus on a few key points. Figure 3.10 shows the results for the absolute value of the SRP in the case of GSAT0202. On simple visual inspection, the figure appears indistinguishable from the corresponding figure of GSAT0201, see Figure 3.7. However, the magnitude is a bit larger due to the smaller mass of GSAT0202, see Tab.3.4. In Figure 3.11, the results for the three components of the SRP accelerations in the Gauss frame are shown. Again, the results have the same general characteristics as those already highlighted in the case of GSAT0201.

3.5.2 S-BW results: Long-term effects on the orbital elements

The BW model is also useful for delineating the *long-term perturbing effects* produced by the SRP. This can be helpful to extract some information related to Fundamental Physics measurements, such as the relativistic precessions of the orbits and the consequent constraints that can be placed on some alternative theories of gravitation, *i.e.* alternative to General Relativity in their predictions.

The most natural way to proceed in this direction is to exploit the accelerations produced by the SRP in the Gauss reference frame, through the corresponding perturbation equations of the osculating elements. In particular, *Gauss perturbation equations* (see Appendix.A) describe the variations of the Keplerian elements under the action of a perturbing acceleration of any origin, *i.e.* due to conservative or non-conservative forces.

Figures from Fig.3.12 to Fig.3.17 show the results obtained for the variation of the six

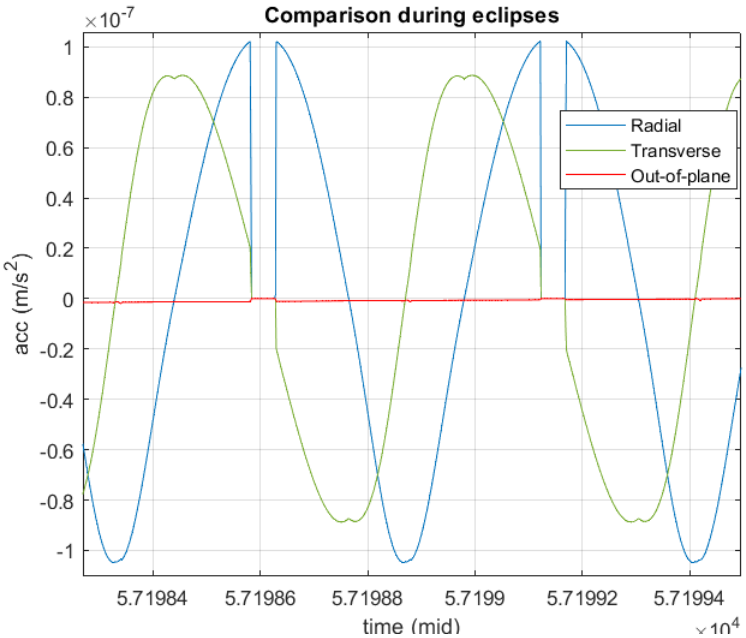

Figure 3.8. *GSAT0201 (E18): components of the Gauss perturbing acceleration due to the direct SRP during eclipses.*

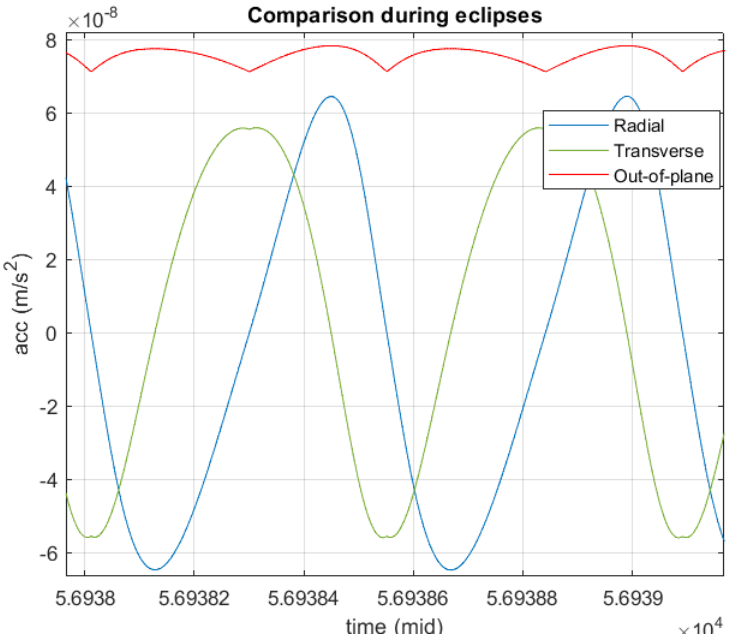

Figure 3.9. *GSAT0201 (E18): components of the Gauss perturbing acceleration due to the direct SRP far from eclipses.*

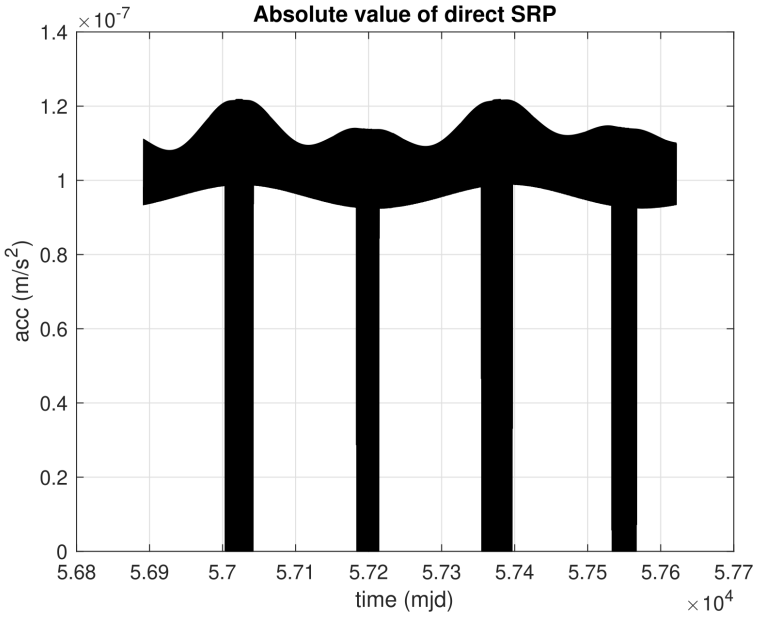

Figure 3.10. *GSAT0202 (E14): absolute value of the acceleration due to the direct SRP.*

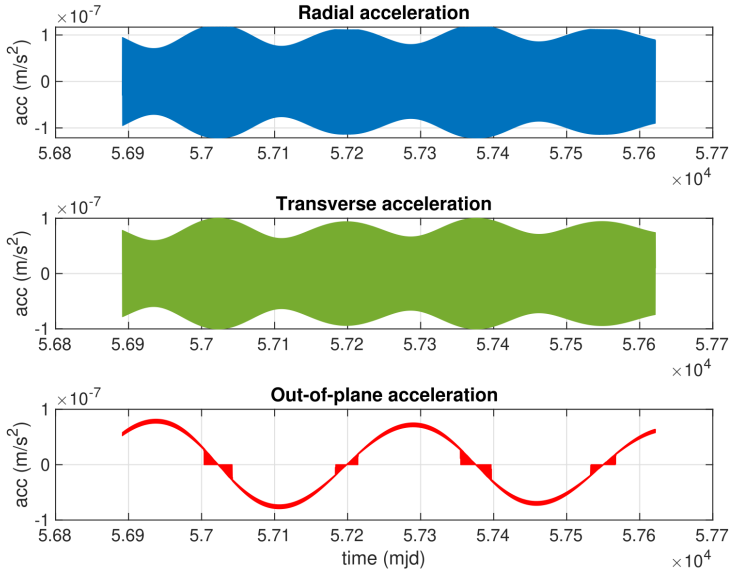

Figure 3.11. *GSAT0202 (E14): acceleration due to the direct SRP along the directions of the Gauss co-moving frame.*

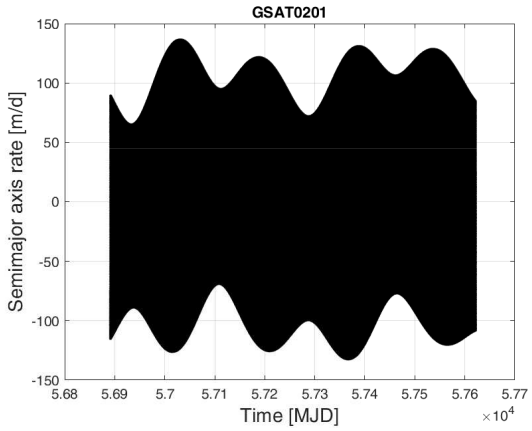

(a) *GSAT0201: long-term evolution of the semi-major axis rate $\dot{a}$.*

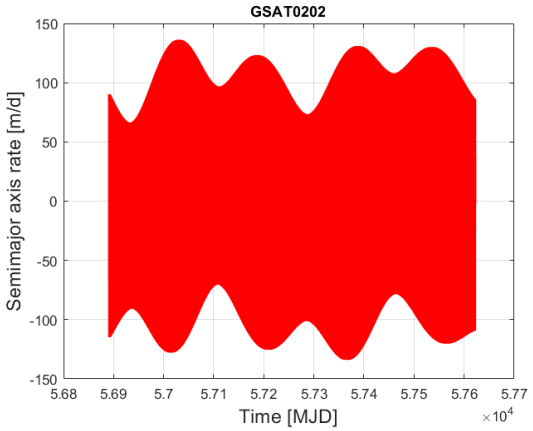

(b) *GSAT0202: long-term evolution of the semi-major axis rate $\dot{a}$.*

Figure 3.12. *Long-term evolution of the semi-major axis rate of the satellites.*

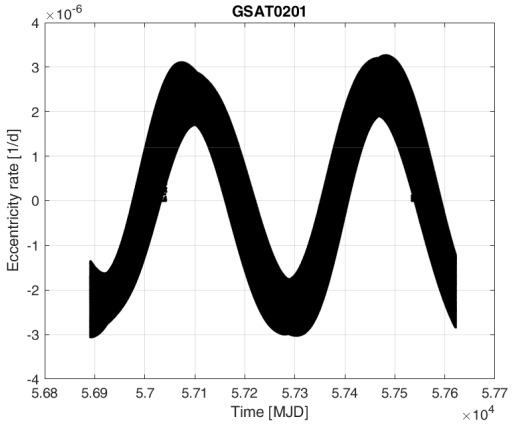

(a) *GSAT0201: long-term evolution of the eccentricity rate $\dot{e}$.*

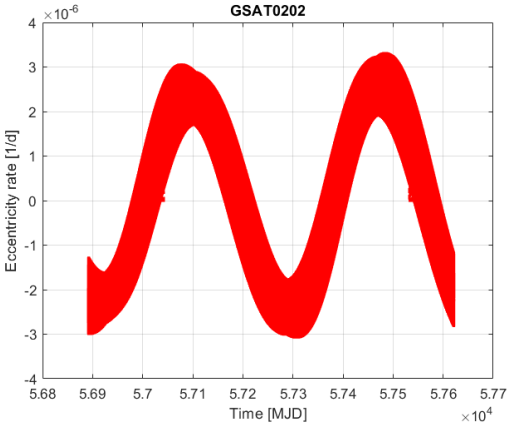

(b) *GSAT0202: long-term evolution of the eccentricity rate $\dot{e}$.*

Figure 3.13. *Long-term evolution of the eccentricity rate of the satellites.*

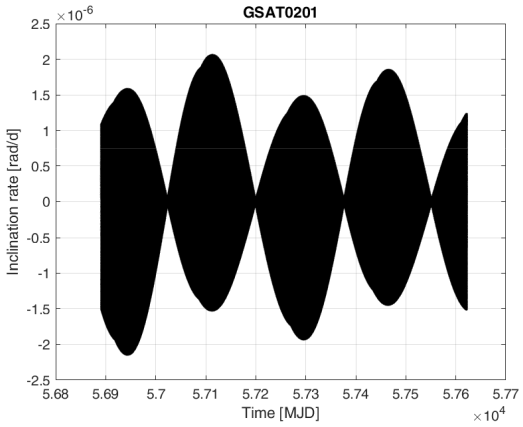

(a) *GSAT0201: long-term evolution of the inclination rate $\dot{I}$.*

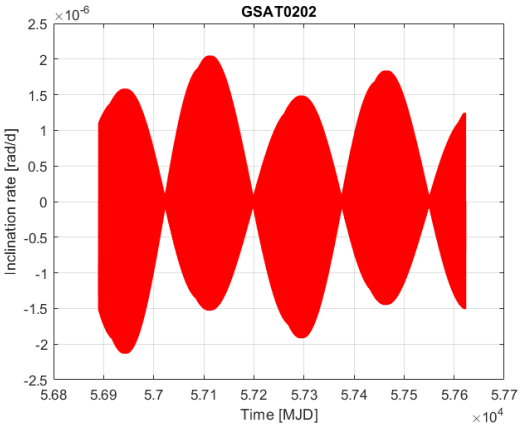

(b) *GSAT0202: long-term evolution of the inclination rate $\dot{I}$.*

Figure 3.14. *Long-term evolution of the inclination rate of the satellites.*

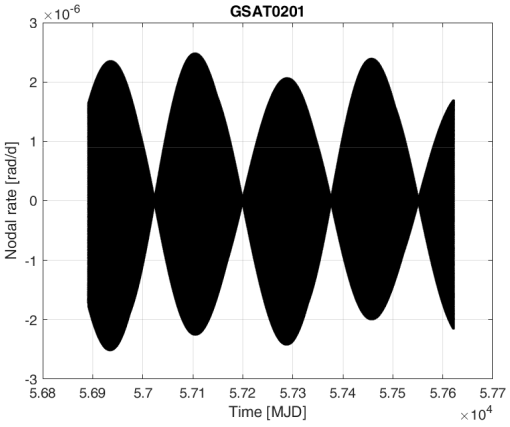

(a) *GSAT0201: long-term evolution of the RAAN rate* $\dot{\Omega}$.

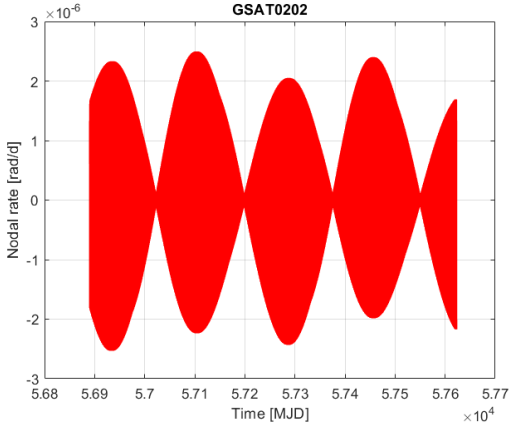

(b) *GSAT0202: long-term evolution of the RAAN rate* $\dot{\Omega}$.

Figure 3.15. *Long-term evolution of the RAAN rate of the satellites.*

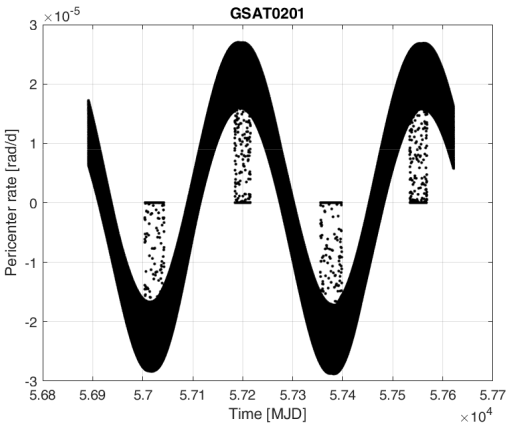

(a) *GSAT0201: long-term evolution of the argument of pericenter rate* $\dot{\omega}$.

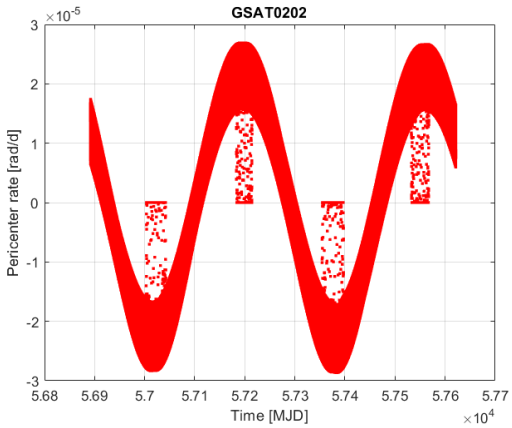

(b) *GSAT0202: long-term evolution of the argument of pericenter rate* $\dot{\omega}$.

Figure 3.16. *Long-term evolution of the argument of pericenter rate of the satellites.*

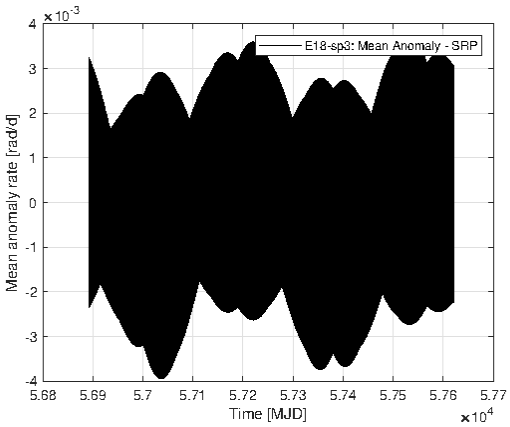

(a) *GSAT0201: long-term evolution of the Mean anomaly rate in* η: $\dot{\eta}$.

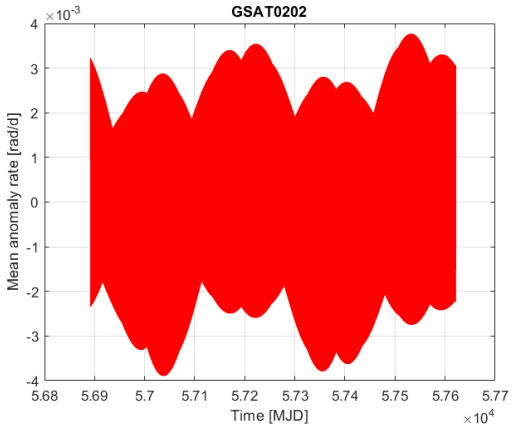

(b) *GSAT0202: long-term evolution of the Mean anomaly rate in* η: $\dot{\eta}$.

Figure 3.17. *Long-term evolution of the mean anomaly rate of the satellites in* η.

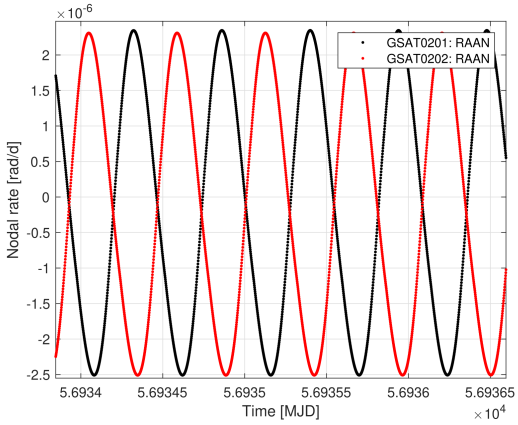

(a) *GSAT0201 and GSAT0202: differences in the long-term evolution of the RAAN rate* $\dot{\Omega}$.

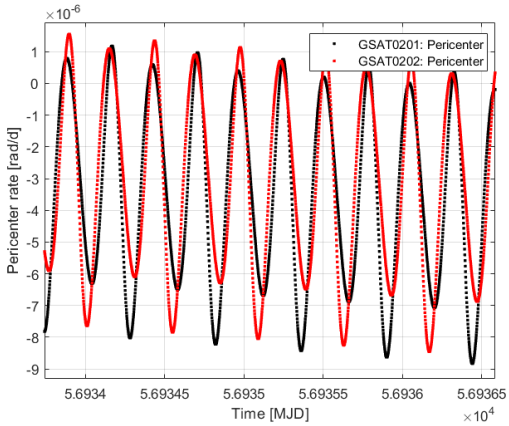

(b) *GSAT0201 and GSAT0202: differences in the long-term evolution of argument of pericenter rate* $\dot{\omega}$.

Figure 3.18. *Differences in the long-term evolution of the RAAN rate and of the argument of pericenter rate of the satellites.*

Keplerian elements of GSAT0201 and GSAT0202 on the basis of our S-BW model and the Gauss perturbing equations. The units of measurement are in m/d and 1/d, respectively for the rate in the semimajor axis and in the eccentricity of the satellites, while they are in rad/d for the angular variables. Upon first visual inspection, the results for the two satellites appear to be identical. However, in reality they are not exactly the same. The apparent overlap in the results for the different elements is due to the fact that the orbits are very close, with the same mean elements and very close initial conditions, see Tab.2.3 and Tab.3.5.

The non-overlapping of the results is evident in Fig.3.18, where the evolution of the rate of the RAAN and of the rate of the argument of pericenter for the two satellites are compared over a limited time interval of some orbits. In the case of the nodal rate, the evolution is characterised by the same amplitude, but with opposite phase. Conversely, in the case of the rate of the argument of pericenter, the behaviour is almost in phase but with different amplitudes.

In the case of the mean anomaly variation, see Fig.3.17, we plotted the long-term behaviour of $\dot{\eta}$, since that variation in ρ is comparable because of the behaviour of the semi-major axis rate, mainly characterised by an oscillation at the orbital frequency.

It is evident that the short and long-term periodic effects characterising the rates of the different orbital elements are those found for the three components of Gaussian acceleration further modulated by the (fast and slow) angular variables f, E and ω which enter the Gauss equations.

As already anticipated in Chap.1, one of the goals of G4S_2.0 is to measure the relativistic precessions of the orbits of the Galileo FOC satellites. In this context, an interesting aspect emerges from the long-term behaviour obtained for Ω (Fig.3.15) and for ω (Fig.3.16). As can be seen from these figures, integer multiples of a solar year (or rather of a draconic period) contain a complete integer number of long-period oscillations, *i.e.* full cycles. This implies that the unmodelled or poorly modelled effects of direct solar radiation tend to average towards zero (even if not completely) over these time intervals, consequently reducing their impact on the estimation of systematic errors. It may therefore be advantageous to perform the analysis on integer multiples of the solar year for relativistic precession measurements.

In Tab.3.2 we reported the main relativistic precession acting on the argument of pericenter and on the RAAN for two Galileo FOC satellites and the geodetic satellite LAGEOs II. As already underlined, measuring these effects, in the case of Galileo satellites, will be very hard, in particular for the RAAN, because of the smaller relativistic effects and of the larger NGPs.

In Tab.3.6, the average value we have obtained for the rate of the argument of the pericenter at different time intervals of our 2-years analysis. The average changes by about two orders of magnitude when moving from an interval of about 8 months to an interval containing one or two draconitic periods. Furthermore, even over two different draconitic periods of one year, the averages are different, since the maximum positive amplitudes and the maximum negative

Element	first 8 months	1st year	2 years	2nd year	last 8 months
$<\dot{\omega}>$	-8.698×10^{-6}	$+1.77 \times 10^{-7}$	$+7.0 \times 10^{-8}$	-3.6×10^{-8}	4.396×10^{-6}
$<\dot{\omega}>$	$-655,291$	$+13,335$	$+5,274$	$-2,712$	$+331,187$

Table 3.6. *GSAT0201 (E18). Average values in rad/d (first line) and in mas/yr (second line) for the rate of the argument of pericenter $\dot{\omega}$ on different time intervals of our 2-year analysis.*

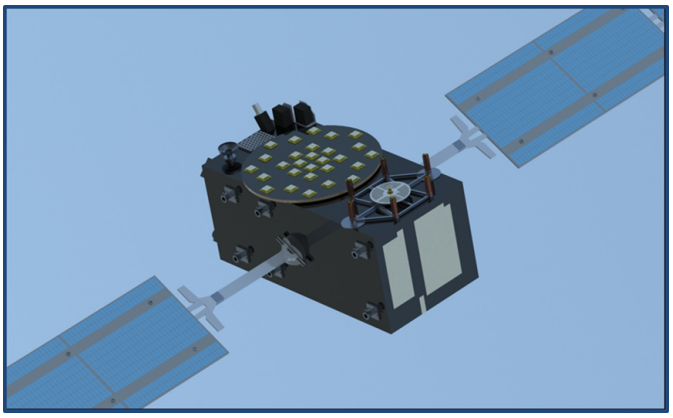

Figure 3.19. *The 3D-CAD model of a Galileo FOC spacecraft. Credits: [30].*

amplitudes are different, due to the variation of the Sun's height in the orbital plane of the satellite. These average values are huge in comparison with the smallness of the relativistic precessions. In reality, the values to be taken into account for the systematic errors estimation are somewhat smaller than those indicated in Tab.3.6. In fact, we have to consider the accuracy with which we model the SRP in the POD software: the relativistic precessions average-values, over a certain time-period, have to be rescaled by a factor that depends on this accuracy. If one succeeds in building a FEM, this would allow the average values to be reduced by a factor up to 100 and the error should be based on the knowledge of the optical parameters.

Similar considerations apply in the case of the right ascension rate of the ascending node. In this case, measuring the total relativistic effect is somewhat complicated and probably unlikely given the small relativistic precessions involved, as it is shown in Tab.3.2.

3.6 The 3D-CAD model and the Ray-Tracing Technique

The Galileo Metadata provide very poor information about the Galileo satellites. Therefore, in addition to the S-BW, a 3D-CAD of the spacecraft has been developed. Some of the necessary information, such as positions and sizes of the various satellite components, was derived indirectly from the large number of spacecraft photographs available from ESA. Then, the `SketchUp`[16] programme was employed to build the 3D-CAD of the Galileo satellite [30]. Using this software, we first drew a parallelepiped with the dimensions given in the Galileo Metadata for the box, see Tab.2.1 and with the average optical coefficients specified in Tab.2.2 for both the box and solar array of the wings. This information is taken from ESA Galileo Metadata. Many photos representing the different parts of the satellite were then matched to this drawing. `SketchUp` allows the representation of the 3D model drawn in it to be modified by changing the point of view and the focal length. These parameters were modified in order to perfectly overlay the photo used as a background.

Finally, a 3D model was created in a CAD (Computer Aided Design) using the `SolidWorks`[17] software [99] by exploiting the various measurements obtained from the aforementioned process, see Fig.3.19. This figure shows the high level of surface detail achieved, as can be seen by comparing it with the photo of the satellite in Fig.2.1.

[16] https://www.sketchup.com/
[17] www.solidworks.com

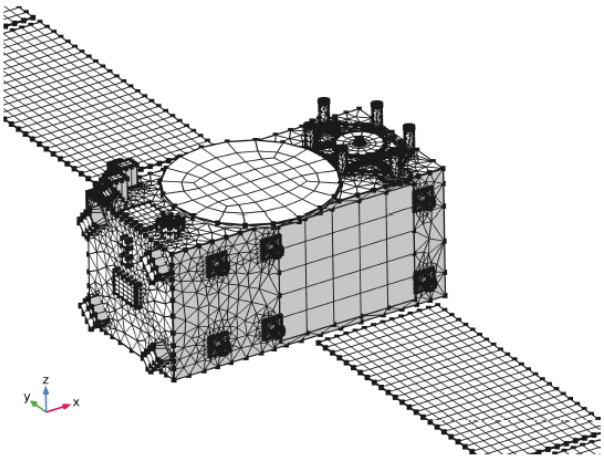

Figure 3.20. *A very preliminary partial mesh of the 3D-CAD model of a Galileo FOC spacecraft. Credits: [30].*

Still referring to [30], regarding the *Ray-Tracing technique* we used the software `COMSOL Multiphysics® "Ray Optics Module"`[18] [100]. We exploit this tool to decompose the satellite surface into finite elements (the so-called "satellite-mesh", see Fig.3.20) at the appropriate level of detail. While waiting to be able to develop a FEM within the G4S_2.0 project, the application of the Ray tracing technique on the S-BW began. Firstly, a BW according to Galileo Metadata was created in `COMSOL` (see again Fig.2.3). The BW dimensions and surfaces are reported in Tab.2.1, while the colours correspond to the materials and corresponding surfaces, described in Tab.2.2. The view factors were then calculated to determine the amount of solar radiation received by each surface of the satellite. This allows the SRP acceleration to be calculated according to Eq.3.28. Once the accelerations acting on each surface of the S-BW have been calculated, they are projected into the body reference frame and then compared with the numerical solution obtained with the `Matlab` S-BW. The comparison for the SRP acceleration is shown in Fig.3.21 over a 500 days simulation. From this figure we can deduce that the two solutions are identical. The only significant difference between the two cases is the spacecraft attitude law. In the case of the `COMSOL`-BW, a nominal attitude was always assumed with the surface of the solar panels orthogonal to the solar radiation. In the case of the `Matlab`-BW, instead, the attitude variation of the satellite during the eclipse season was considered, according to the attitude variation described in the ESA metadata. The significant differences between the two models are evident only during the eclipse-season (see Fig.3.22).

The next steps in using `COMSOL` involve the implementation of the satellite's rotation around the satellite's yaw axis, *i.e.* around the Earth-satellite radial direction, and the application of `COMSOL` Ray-Tracing algorithms on a more simplified 3D model of the spacecraft than the one shown in Fig.3.19.

[18] www.comsol.com

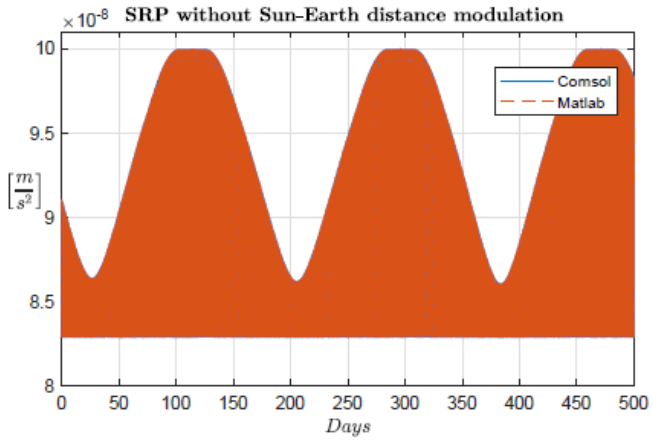

Figure 3.21. *Comparison between the absolute value of the direct SRP acceleration obtained with the BW developed in COMSOL (blue line) with the same acceleration obtained and the S-BW model implemented in MATLAB (brown line). Both solutions are functions of time. Credits: [30].*

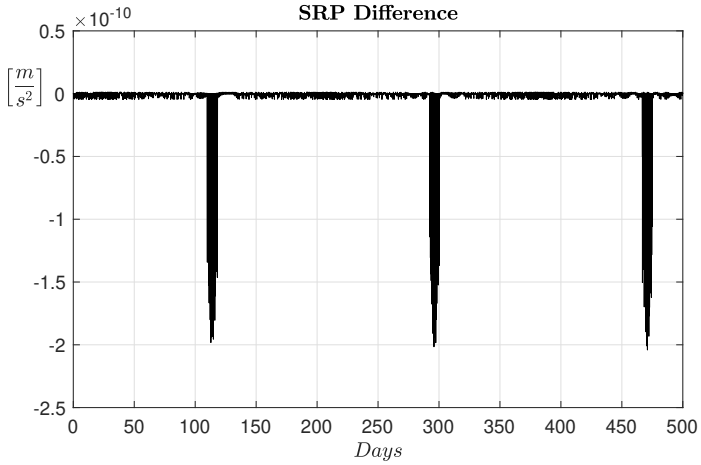

Figure 3.22. *Difference in the asolute value of the direct SRP acceleration obtained with the* `MATLAB` *model with the corresponding acceleration obtained with* `COMSOL`*. Credits: [30].*

Chapter 4

Precise Orbit Determination

This Chapter introduces the basic principles on which precise orbit determination is based. It then briefly describes the software we currently use for POD: `GEODYN II` and `Bernese`. The former will be used to extract relativistic precessions measurements from orbital residuals, while the latter will be used for the gravitational redshift measurement. Finally, we compare the predictions of our S-BW with the `Geodyn II` orbital residuals. We deduce that almost all of the observed and unmodelled effects by `GEODYN II` cannonball model can be reproduced by our S-BW. This is an important result in view of better characterising the precise orbit determination performed by `GEODYN II`. Therefore, we insert our S-BW model in the POD procedure highlighting the improvements we can achieve with it.

4.1 POD in a nutshell

The *Precise Orbit Determination* (POD) aims to accurately determine the position and velocity vectors of a body in orbit. This problem ranges from natural bodies to artificial ones, both around a planet such as the Earth, or along a trajectory in the Solar System. Essentially, the POD is based on the following main points:

- A dynamical model
- Observations, obtained by one or more tracking system
- Least squares principle.

The outcome of this procedure is a precise description of the orbit obtained by fitting the tracking data with a suitable set of dynamical models, along with a series of estimated parameters [101].

The basic idea of least squares estimation as applied to orbit determination is to find the trajectory and model parameters for which the square of the difference between the modelled observation and the actual measurements is as small as possible [33]. In other words, a trajectory that best fits the observations in a least-squares fit sense.

From the mathematical point of view, let us introduce a time-dependent, l-dimensional vector $\boldsymbol{x}(t) \in \Re^l$ containing the satellite's position $\mathbf{r}$ and velocity $\mathbf{v}$ as well as the model parameters $\boldsymbol{P} \in \Re^m$:

$$\boldsymbol{x}(t) = \begin{bmatrix} \boldsymbol{r}(t) \\ \boldsymbol{v}(t) \\ \boldsymbol{P} \end{bmatrix} . \tag{4.1}$$

The time evolution of $\boldsymbol{x}$ can always be described by an ordinary differential equation of the form

$$\dot{\boldsymbol{x}} = \boldsymbol{f}(t, \boldsymbol{x}, \boldsymbol{P}) \tag{4.2}$$

and an initial value $\boldsymbol{x_0} = \boldsymbol{x}(t_0)$ at epoch t_0. Furthermore, let be

$$\boldsymbol{O} = \begin{bmatrix} O_1 \\ \vdots \\ O_n \, . \end{bmatrix} \tag{4.3}$$

a n-dimensional vector of observations taken at times t_1,...t_n.

In general, the observable is a quadratic function of the range residuals $\boldsymbol{R}$:

$$R_i = O_i - C_i = O_i - C(\boldsymbol{x}(t_i), t_i, \boldsymbol{\beta}) \tag{4.4}$$

where C_i is the computed value of the corresponding observation O_i at time t_i and $\boldsymbol{\beta} \in R^n$ are the kinematic parameters. Considering also the errors associated with the model parameters and the observations (δP_j and δO_i respectively), we can write:

$$R_i = O_i - C_i = O_i - C(\boldsymbol{x}(t_i), t_i, \boldsymbol{\beta}) = \sum_j \frac{\partial C_i}{\partial P_j} \delta P_j + \delta O_i \,. \tag{4.5}$$

Regarding the δO_i errors, they take into account the contribution of the noise in the observations as well as the incompleteness of the mathematical model included in the POD software used. The problem of determining the orbit by the least squares method can now be defined as finding the state $\boldsymbol{x}_0^{lsq}$ which minimises the quadratic function of $\boldsymbol{R}$, $Q(\boldsymbol{R})$:

$$Q(\boldsymbol{R}) = \frac{1}{q} \boldsymbol{R}^{\boldsymbol{T}} W \boldsymbol{R} = \frac{1}{q} \sum_{i=1}^{q} \sum_{k=1}^{q} w_{ik} R_i R_k, \tag{4.6}$$

where $W = (w_{ik})$ represents the weigth-matrix, *i.e.* a symmetric matrix with non-negative eigenvalues. In conclusion, a reliable estimation of systematic error sources and a better reduction of orbital data can lead to a more precise and accurate a posteriori reconstruction of satellite orbits. It is therefore extremely important to have both good observations and good models in order to perform Fundamental Physics measurements, such as the gravitational redshift one or the tiny relativistic effects predicted by General Relativity.

Two main strategies can improve POD accuracy in the case of Galileo FOC satellites:

- improving the model of the NGPs that act on GNSS satellites, in order to better characterise the various interactions of the spacecraft with external and internal perturbations sources. As the SRP is the most important NGPs, it is a priority to refine its model as well as possible.
- using the full-rate SLR data and not only the microwave tracking data (pseudorange and carrier phase measurements) can improve the satellite POD during the transition into the Earth's penumbra.

4.1.1 Software for data reduction

Depending on the measurements we want to perform and on the type of data, we use two different POD software. We use the `GEODYN II` software [29] with SLR data for the relativistic precession measurements, as was done for LAGEOS satellites [101]. For the other measurements of the project, *i.e.* gravitational redshift and Domain Wall Dark Matter constraints, we use the `Bernese` software [24] as we deal with clock-bias and microwave data (pseudorange and carrier phase).

A brief description of the operating principle of these software is given below.

4.1.1.1 Geodyn II

`Geodyn II` is a software developed by NASA/GSFC and dedicated to satellite orbit determination and prediction, geodetic parameters estimation, tracking instruments calibration, and many other applications in the field of space geodesy, see [29, 102].

`Geodyn II` solves for the satellite orbit and the needed parameter estimation in two separate steps: (i) the orbit prediction problem and (ii) the parameter estimation problem. The orbit prediction is reached through the numerical integration of the equations of motion of the satellite using Cowell's method.

The integration procedure of Cowell's method is a predictor-corrector procedure, with a fixed time step; this method has the great advantage of being easy to implement for any given number of perturbing bodies or non-gravitational disturbing effects.

Simplifying, `GEODYN II` consists of three main programs: i) the tracking Data Formatter (TDF), ii) GEODYN IIS (GIIS) and iii) GEODYN IIE (GIIE), see Fig.4.1. The details of the input and output files of TDF, GIIS and GIIE are described in Volume 5 of Geodyn II documentation.

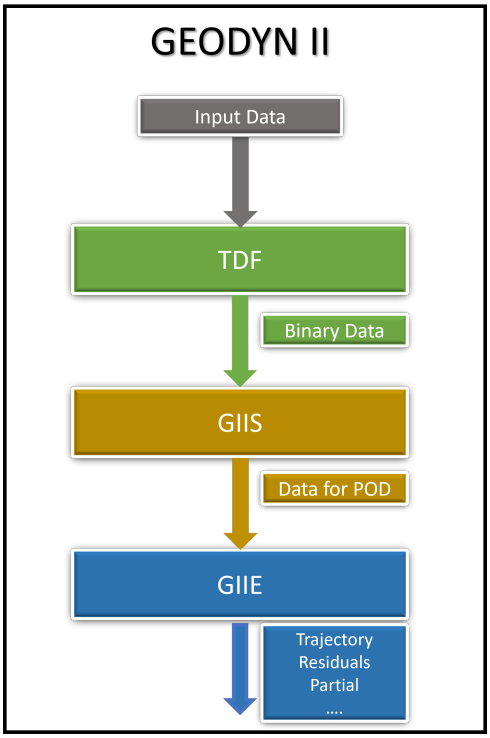

Figure 4.1. *`GEODYN II` schematic block diagram for the three main programs of the code.*

The role of TDF is to convert a set of input data in a variety of formats to blocked GEODYN II binary format. GIIS input files are:

- GEODYN II Blocked Binary Data (From TDF)
- Option Card File (see Volume 3)
- Flux, Polar Motion and UT1 Tables
- JPL Planetary Ephemeris File
- Default Gravity Model File
- Station Geodetics File
- Default Spacecraft Area and Mass Tables.

The main functions of GIIS are i) to read and interpret the option cards; ii) to read, select and rearrange the input observation data; iii) to read the optional gravity model, station geodetics, and area/mass files; and iv) to extract ephemeris and table data from the appropriate files for the time period covered by the given run. The role of GIIS is to prepare for the GIIE run, *i.e.* for the final data reduction, in order to minimize the amount of data manipulation to be performed in the GIIE program.

Finally, GIIE performs all the computations normally associated with satellite orbit and geodetic parameter estimation programs. As said, GIIE perform the data reduction, *i.e.* the POD of the satellite. Among the outputs of GIIE we have:

1. Trajectory File
2. Residual File

3. Partial Derivative File
4. Normal Equation File
5. Force Model Partial Derivative File.

We refer to `GEODYN II` documentation for further information on https://earth.gsfc.nasa.gov/geo/data/geodyn-documentation.

The modelling setup we are currently using is shown in Tab.4.1. It accounts for: i) the satellite dynamics, ii) the measurement procedure and iii) the reference frames transformations. In this context, our models comply, wherever possible, with the international resolutions and conventions, such as the International Astronomical Union (IAU) 2000 Resolutions [103] and the IERS Conventions (2010) [104]. As anticipated above, `Geodyn II` represents our reference software for the data reduction of the SLR Normal Points to be used for the measurement of the relativistic precessions, i.e. Schwarzschild [1], Lense-Thirring [67] and de Sitter precession [68].

Table 4.1. *Models currently used for the POD obtained from GEODYN II. The models are grouped in gravitational perturbations, non-gravitational perturbations and reference frames realizations.*

Model for	Model type	Reference
Geopotential (static)	EIGEN-GRACE02S/GGM05S	[49, 54, 105]
Geopotential (time-varying: even zonal harmonics)	GRACE/GRACE FO	[49, 54]
Geopotential (time-varying: tides)	Ray GOT99.2	[106]
Geopotential (time-varying: non tidal)	IERS Conventions 2010	[104]
Third–body	JPL DE-403	[107]
Relativistic corrections	Parameterised post-Newtonian	[65, 103]
Direct solar radiation pressure	Cannonball/Box-Wing	[29–31]
Earth albedo	Knocke-Rubincam	[71]
Earth-Yarkovsky	Rubincam	[108–110]
Neutral drag	JR-71/MSIS-86	[111, 112]
Spin	LASSOS	[113]
Stations position	ITRF2008/2014	[114, 115]
Ocean loading	Schernek and GOT99.2 tides	[29, 106]
Earth Rotation Parameters	IERS EOP C04	[116]
Nutation	IAU 2000	[117]
Precession	IAU 2000	[118]

The model for `Geodyn II` relativistic corrections refers to the Parameterised post-Newtonian (PPN) formalism [119–121] according to the formulation described in [65].

The internal models of `Geodyn II` have been enriched through the development of external models in the case of the non-conservative forces acting on LAGEOS type satellites [36, 70, 101, 113, 122, 123] and, on the occasion of the present G4S_2.0 project, for those acting on the Galileo FOC satellites [30, 31].

Furthermore, to take into account the inevitable incompleteness of any dynamical model, `Geodyn II` allows some empirical accelerations to be estimated arc by arc. These are general acceleration terms added to the equations of motion, and they are aimed at modelling and/or absorbing otherwise unknown small effects which may be relevant for the dynamics. In `Geodyn II`, these acceleration are decomposed in the three Gauss directions under the general form:

$$a(t) = a_0(t) + a_c(t)\cos\left(\omega(t) + f(t)\right) + a_s(t)\sin\left(\omega(t) + f(t)\right), \tag{4.7}$$

where the amplitudes a_c and a_s define the terms of acceleration at orbital frequency (in phase and in quadrature), while ω and f represents, respectively, the argument of pericenter and the true anomaly.

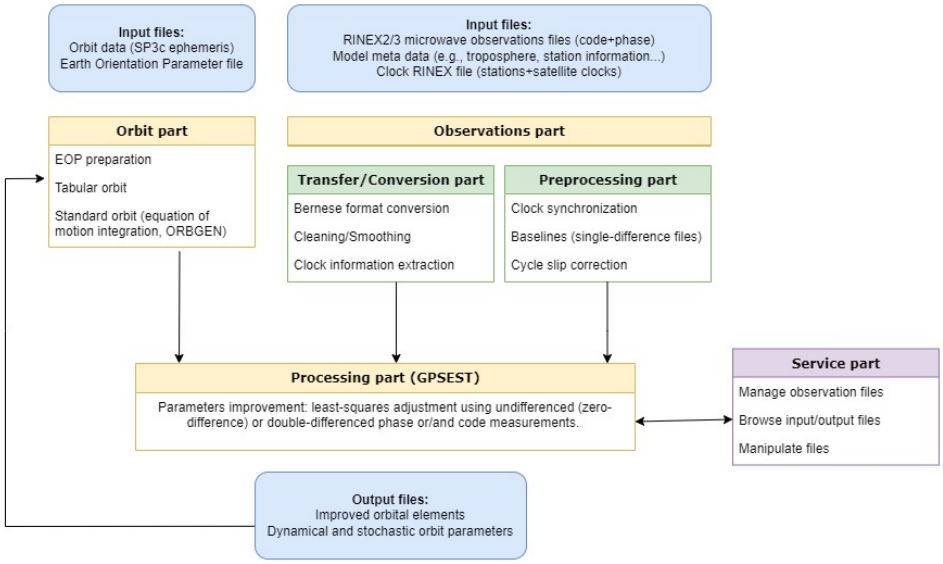

Figure 4.2. *The* `Bernese` *program structure.*

4.1.1.2 Bernese

The `Bernese GNSS Software` is a scientific multi-GNSS data processing software developed at the Astronomical Institute of the University of Bern (AIUB)[1]. It is a very useful tool for the space-geodetic community for all activities associated to high performance processing of measurements, obtained by GNSS and SLR, and precise orbit determination.

In Fig.4.2 the `Bernese` flow-diagram of a standard processing is shown. It is composed by [24]:

- The *Transfer Part* contains all the programs related to transfer of RINEX files (observations, navigation messages, meteorological files, clock files) to Bernese format or vice versa, and the manipulation of `RINEX` files.
- The *Conversion Part* collects programs to convert binary files into `ASCII` format and vice versa.
- The *Orbit Part* contains all the programs associated with satellite orbits and Earth Orientation Parameters (EOPs). This includes generating an internal orbital representation (called a standard orbit) from precise ephemerides (`SP3c` files) or broadcast information, updating orbital information, and generating precise orbital files.
- The *Processing part* contains the main processing programs. After a phase that consists in the observations pre-processing, the core of this part is represented by two main programs for the estimation parameters: `GPSEST`, based on GPS and/or GLONASS or SLR observations, and `ADDNEQ2` based on the superposition of normal equation system. The former works at least squares on single-arc solutions and allows the orbital parameters to be updated, while the latter allows single-arc solutions to be combined to obtain multi-arc solutions from the `GPSEST` ouputs (i.e. single-arc solutions).
- The *Simulation* part consists of a single program for the generation of simulated GPS and GLONASS observations based on statistical information (such as the RMS of observations).
- The *Service part* is a collection of useful tools for handling station information files, editing binary observation files, checking residuals, comparing and manipulating coordinates, and for automated processing.

[1] `http://www.bernese.unibe.ch/`

We currently use the Bernese software with the aim of obtaining the POD for the satellites of the Galileo-FOC constellation - in particular, for the Milena (GSAT0202) and Doresa (GSAT0201) satellites. In Bernese, the POD (or Orbit Improvement) is the process of improving orbital parameters using observations (microwave observations in our application). The orbital parameters that can be improved are the six Keplerian osculating elements (initial conditions at the beginning of the orbit), up to nine parameters of the CODE (Center for Orbit Determination in Europe) empirical radiation pressure model. The required procedure is divided into two main activities: obtaining an accurate a priori orbit (or standard orbit) starting from the precise ephemerides in SP3-c format; and pre-processing the microwave observations (phase and/or code) released by the CCDIS ground station network to be used for the POD [2].

Other activities have been carried out in the context of clock-bias estimation for the Galileo constellation satellites. In this regard, we will also process SLR data with Bernese, as orbit modelling errors are strongly correlated with the clock solutions. In fact, SLR data are essential to characterize orbital radial errors in the IGS Analysis Centers solutions, as radial systematic errors are one-to-one correlated with the on-board clock solution.

Finally, with Bernese 5.4 we will have the possibility to insert our S-BW model for NGPs, in the POD procedure. This will allow us to compare the results of two (or more) measurements obtained with two different software, thus demonstrating the reliability and robustness of the scientific results we will obtain within G4S_2.0 project.

4.2 PODs long-term effects

In this paragraph we show the preliminary results of the PODs performed for the GSAT0201 satellite in elliptical orbit and for the GSAT0208 satellite in nominal orbit. These analyses have been carried out using GEODYN II for the data reduction of the satellites normal points (NPs). The modelling setup accounts for: i) the satellite dynamics, ii) the measurement procedure iii) the background gravitational field and iv) the reference frames transformations. As far as possible, our models comply with international resolutions and conventions, such as the International Astronomical Union (IAU) Resolutions 2000 [103] and the IERS Conventions 2010 [104] (see Tab.4.1).

Since GEODYN II has a BW model only for a GPS satellite, we start our analysis with a simple cannonball model as a dynamical model for the satellites of our interest. We have currently used it with the average area-to-mass ratio of a Galileo FOC satellite (see Tab.2.3) to model the spacecraft in the POD. On the one hand, this choice gives us the opportunity to highlight, in the POD results, the improvements gradually obtained from a simple satellite model to the final FEM via the current S-BW model. On the other hand, as noted in the previous §3.5.2, we expect that even a simplified model gives a significant feedback on long-term effects, and our aim is to evaluate how good it is. Finally, we perform a POD by inserting our S-BW and obtain a significant reduction in the orbital residuals (see §4.2.1).

The analyses covered the period from the launch dates of the two satellites, (see Tab.2.3), until 25 November 2022: *i.e.* about 8 years in the case of GSAT0201 and about 6.8 years for GSAT0208. These time intervals were then divided into non-causally related arcs of 7 days for the POD[3]. The POD step size was 50 s. In addition, to overcome the current over-simplification of the dynamical model, in particular that of the non-gravitational forces, empirical accelerations in the form of constant and once-per-revolution were introduced and adjusted to remove the effect of the mismodelling[4]. The models we use for the Earth's background gravitational field is EIGEN-GRACE02S [105] up to degree and order 30.

Figures from 4.3 to 4.7 show the results obtained for the long-term evolution of the Keplerian elements of the two satellites. Specifically, the values plotted represent the adjustment of the state-vector at the beginning of each 7-day arc to best fit the available tracking observations

[2] https://cddis.nasa.gov/Data_and_Derived_Products/GNSS/GNSS_data_and_product_archive.html

[3] The sampling time of 7 days is chosen to study relativistic effects. In principle, there is no limit of GEODYN II on the sampling time, it only needs to have frequent observations.

[4] This type of orbit modelling is useful when longwavelengths orbit errors, including secular perturbing effects, need to be removed, as well as for long-period resonances and non-gravitational perturbations that are not included in the software dynamical model, as in this case. Experience shows that they can easily bias the estimation of other quantities, although they are useful for improving the quality of the fit.

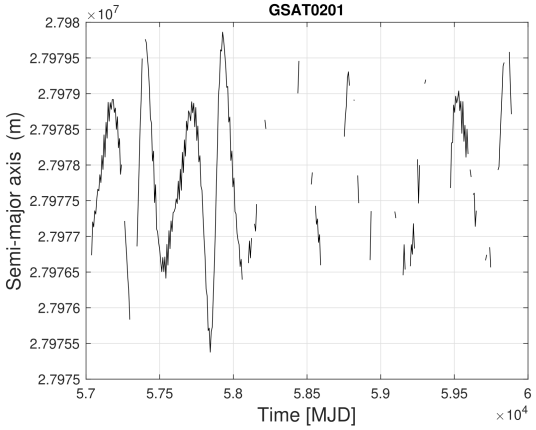

(a) *GSAT0201: long-term evolution of the satellite semimajor-axis.*

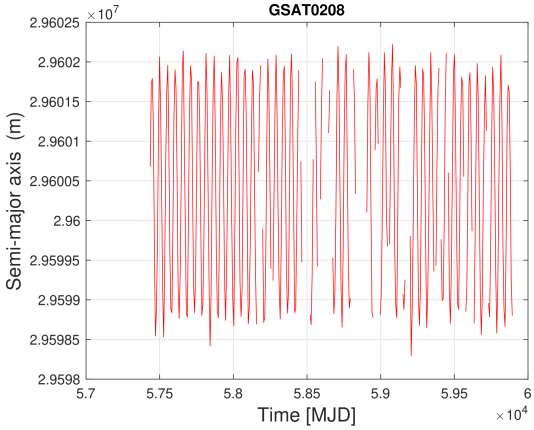

(b) *GSAT0208: long-term evolution of the satellite semimajor-axis.*

Figure 4.3. *GEODYN II POD: Long-term evolution of the semimajor-axis of the satellites.*

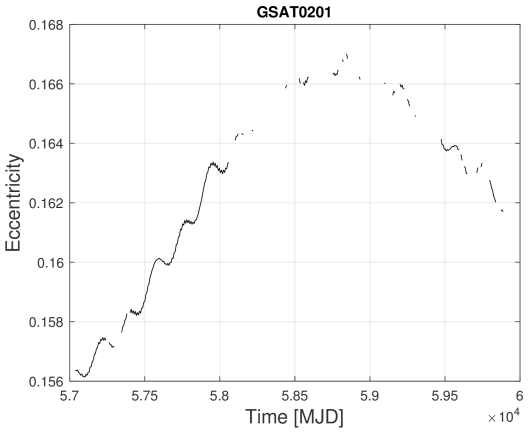

(a) *GSAT0201:long-term evolution of the satellite eccentricity.*

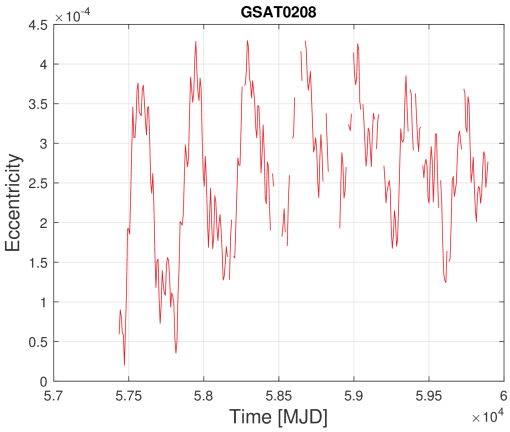

(b) *GSAT0208: long-term evolution of the satellite eccentricity.*

Figure 4.4. *GEODYN II POD: Long-term evolution of the eccentricity of the satellites.*

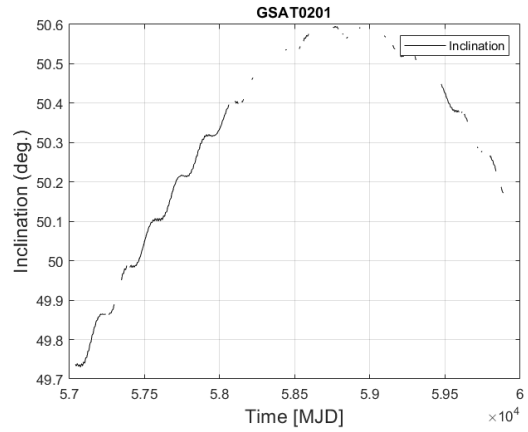

(a) *GSAT0201:long-term evolution of the satellite inclination.*

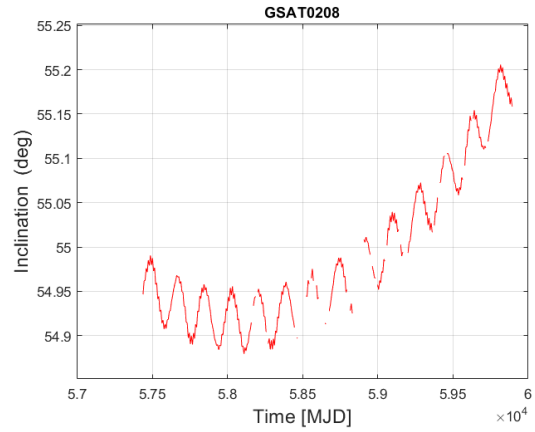

(b) *GSAT0208: long-term evolution of the satellite inclination.*

Figure 4.5. *GEODYN II POD: Long-term evolution of the inclination of the satellites.*

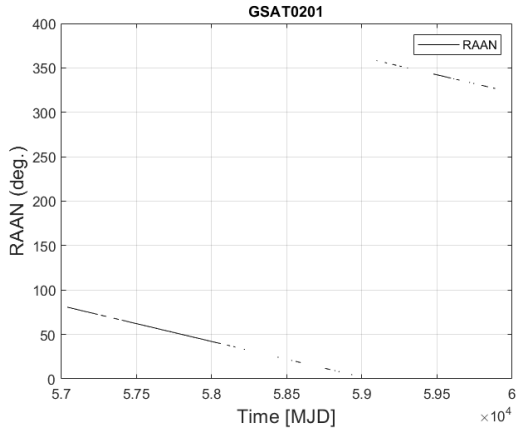

(a) *GSAT0201:long-term evolution of the satellite RAAN.*

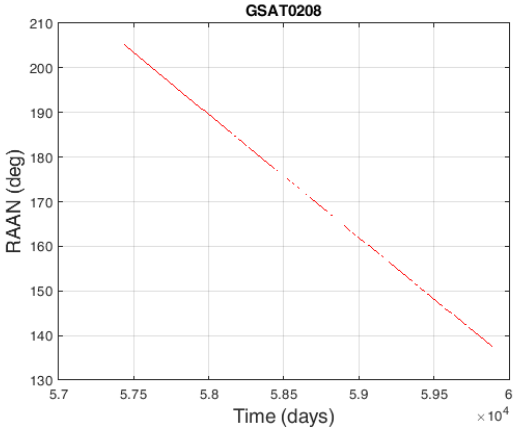

(b) *GSAT0208: long-term evolution of the satellite RAAN.*

Figure 4.6. *GEODYN II POD: Long-term evolution of the of the right ascension of the ascending node of the satellites.*

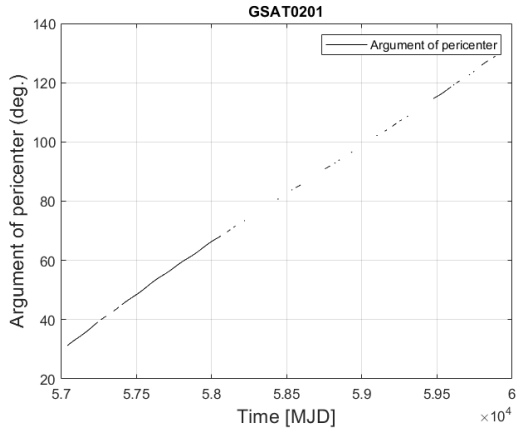

(a) *GSAT0201: long-term evolution of the satellite argument of pericenter.*

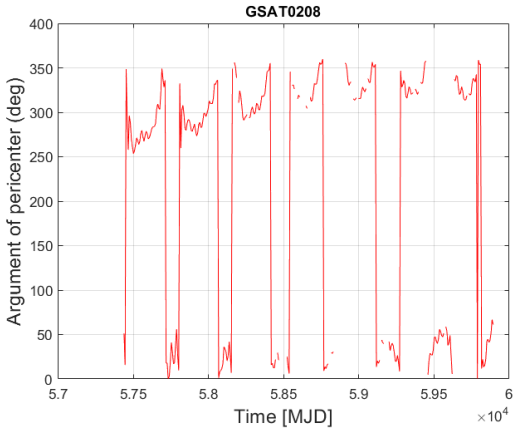

(b) *GSAT0208: long-term evolution of the satellite argument of pericenter.*

Figure 4.7. *GEODYN II POD: Long-term evolution of the argument of pericenter of the satellites.*

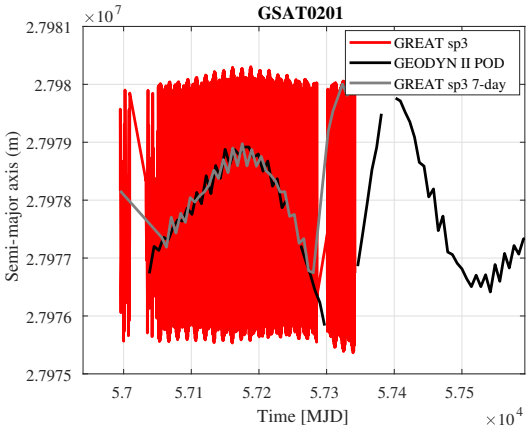

(a) *GSAT0201: long-term evolution of the satellite semi-major-axis.*

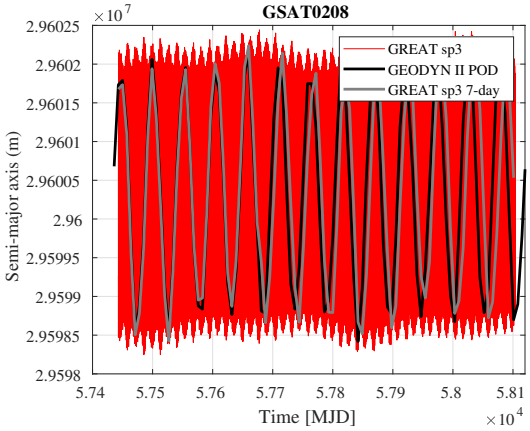

(b) *GSAT0208: long-term evolution of the satellite semi-major-axis.*

Figure 4.8. *Comparison between* `GEODYN II` *POD (black) and GREAT* `SP3-c` *precise orbit (red): Long-term evolution of the semi-major-axis of the satellites.*

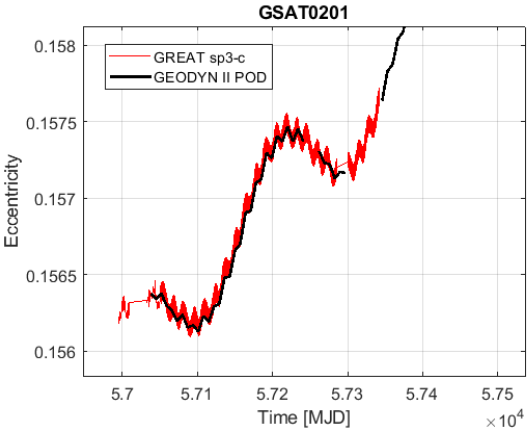

(a) *GSAT0201: long-term evolution of the satellite eccentricity.*

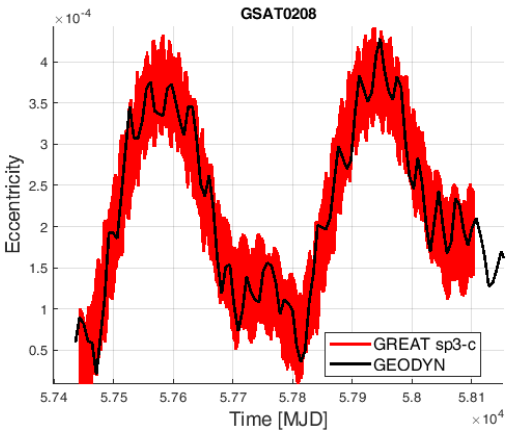

(b) *GSAT0208: long-term evolution of the satellite eccentricity.*

Figure 4.9. *Comparison between* `GEODYN II` *POD (black) and GREAT* `SP3-c` *precise orbit (red): Long-term evolution of the eccentricity of the satellites.*

of GSAT0201 and GSAT0208. The initial (a-priori) state-vector for the satellites was obtained from their `Two Line Elements` (TLE) as provided by NORAD[5](North American Aerospace Defense Command). As we can deduce from these figures, the long-term evolution of the orbital elements in the case of GSAT0201 is different from that of GSAT0208. This is mainly due to the eccentricity of the orbit. In particular, an eccentricity significantly different from zero is responsible for further long and (also short) term perturbations effects, starting with the Earth's gravitational field [124].

We then compare the results of our PODs with those obtained from the precise orbits produced by the IGS analysis centres. In particular, we compare our PODs with the precise orbits obtained by ESOC for the previous GREAT experiment. The precise orbits, already introduced in §2.4, are distributed according to the `Extended Standard Product-3` (`SP3-c`) format. In the case of GREAT, the precise orbits were obtained from ESA's `NAPEOS` orbit determination code [23], probably exploiting the dynamical models for non-gravitational forces developed within this project.

The results of the comparison in the case of GSAT0201 and GSAT0208 are shown from Fig.4.8 to Fig.4.12, respectively for the satellites semi-major axis, eccentricity, inclination, right

[5]see https://space-track.org/

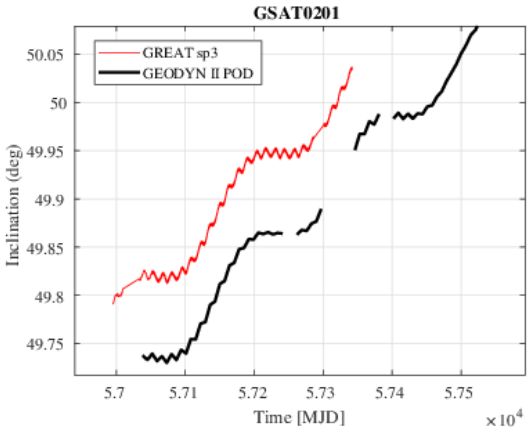

(a) *GSAT0201: long-term evolution of the satellite inclination.*

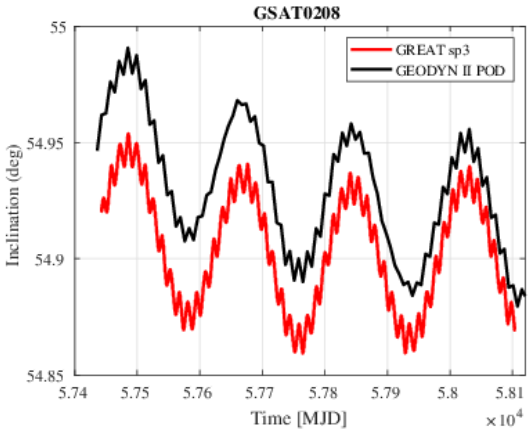

(b) *GSAT0208: long-term evolution of the satellite inclination.*

Figure 4.10. *Comparison between* `GEODYN II` *POD (black) and GREAT* `SP3-c` *precise orbit (red): Long-term evolution of the inclination of the satellites.*

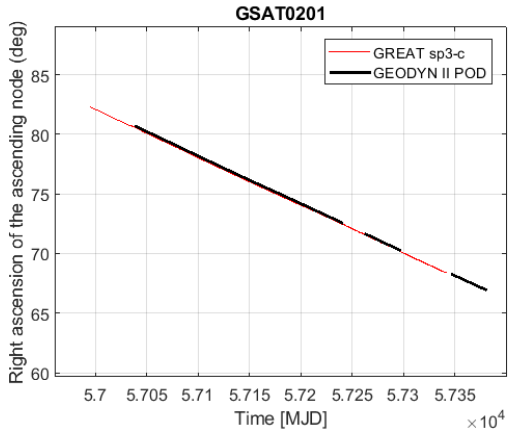

(a) *GSAT0201: long-term evolution of the satellite RAAN.*

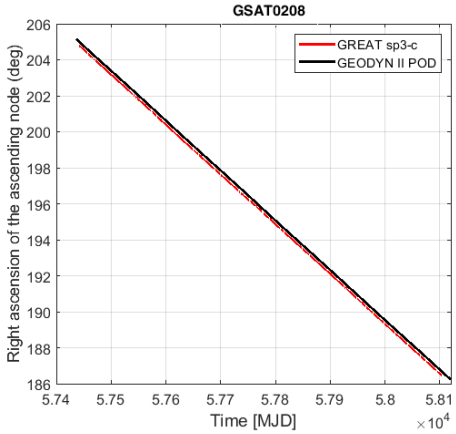

(b) *GSAT0208: long-term evolution of the satellite RAAN.*

Figure 4.11. *Comparison between* `GEODYN II` *POD (black) and GREAT* `SP3-c` *precise orbit (red): Long-term evolution of the RAAN of the satellites.*

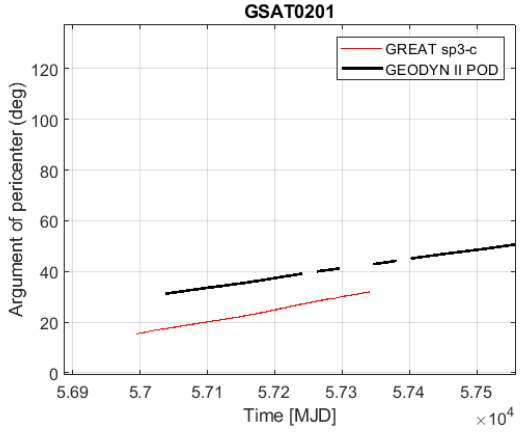

(a) *GSAT0201: long-term evolution of the satellite argument of pericenter.*

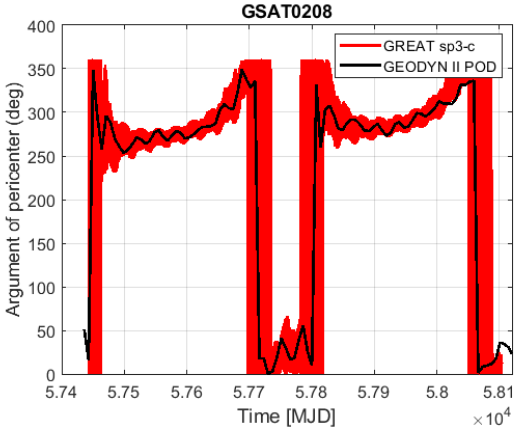

(b) *GSAT0208: long-term evolution of the satellite argument of pericenter.*

Figure 4.12. *Comparison between* `GEODYN II` *POD (black) and GREAT* `SP3-c` *precise orbit (red): Long-term evolution of the argument of pericenter of the satellites.*

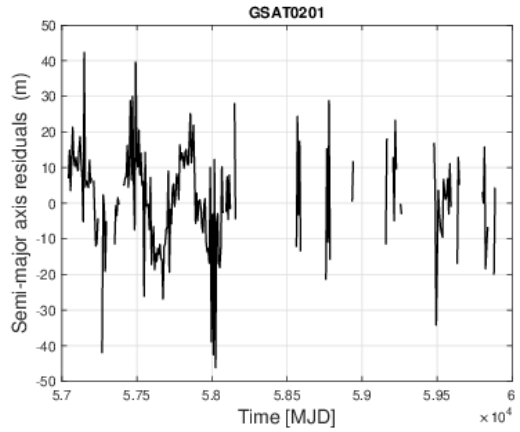

(a) *GSAT0201:long-term evolution of the satellite's semi-major axis residuals over the entire analysis period.*

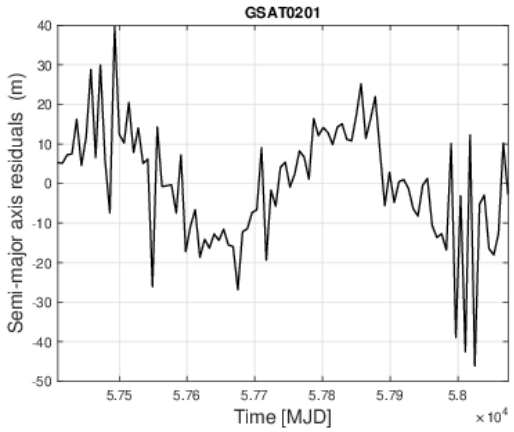

(b) *GSAT0201:long-term evolution of the satellite's semi-major axis residuals in the period 2016 - 2017.*

Figure 4.13. *GSAT0201: residuals on 7-day of the satellite's semi-major-axis.*

ascension of the ascending node and argument of pericenter. The osculating Keplerian elements are plotted in both cases, `GEODYN II` vs. GREAT `SP3-c`. As can be seen in practically all the figures, the agreement on the long-term behaviour of the orbits obtained with `GEODYN II`, based on a simple cannonball model, with those obtained by the `NAPEOS` software is quite good. One difference is the sampling time of the plotted data: 7 days in the case of the `GEODYN II`-POD and 300 s in the case of the `NAPEOS`-POD. This difference is particularly evident in the case of the semi-major axis but it is less marked in the other cases. Therefore, in the case of the semi-major axis, we plotted the GREAT data sampled every 7 days (grey line) to get a better view of the the two behaviours which are in agreement, anyway. For some quantities, it was preferred to plot the cumulative sum of the results obtained, as in the case of the right ascension of the ascending node of the two satellites or of the argument of the pericenter in the case of GSAT0201. So, to compare our POD results with those provided at the high frequencies of the precise orbits obtained by GREAT, we need to reduce the length of our arc and replace the cannonball model with more sophisticated models, as already anticipated, starting with the S-BW model.

Nevertheless, the results obtained with the current approximation are encouraging as regards the measurement of relativistic precessions, related to the secular effects produced by GR, or by theories of gravitation alternatives to GR, on the right ascension of the ascending node of the orbit and, in particular, on the argument of the pericenter of the satellites (see next section for further details). The agreement is also remarkable in the case of the eccentricity of the satellites, as well as for their inclination.

We can come to the following conclusion: these results give us a clear indication of the possibility of using `GEODYN II` to determine the effects of relativistic precessions on the orbit of the Galileo FOC satellites, even in the case where the satellite's dynamical model is not sophisticated enough with respect to the NGPs. Of course, it is necessary to have a sufficient number of laser observations to ensure the convergence of the state vectors in the data reduction process.

In order to derive gravitational effects from the analysis of satellite orbital residuals, we performed a second POD, different from the previous one, in which GR is not modelled and the empirical accelerations are not estimated. The results are shown from Fig.4.13 to Fig.4.18. The model for the `GEODYN II` relativistic corrections refers to the *Parameterised post-Newtonian* (PPN) formalism [119–121] according to the formulation described in [65].

The plotted residuals have been determined with the method described in [125] exploiting the difference between the satellite's state-vector estimated by `GEODYN II` at the beginning of each arc and the propagated value of the (estimated) state-vector of the previous arc at the same epoch. Since the residuals were obtained by propagating the state vector along the length of each arc, they represent the residuals in the rate of the orbital elements, more precisely their variation over 7 days.

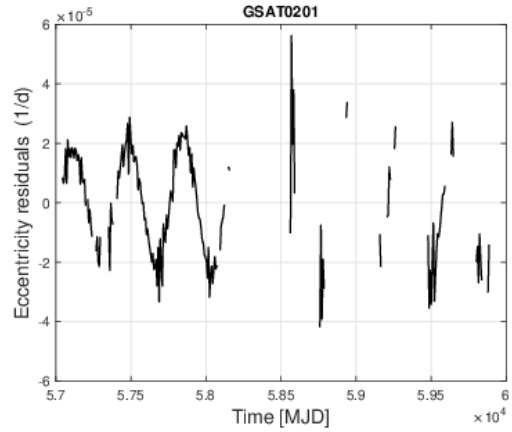

(a) *GSAT0201:long-term evolution of the satellite's eccentricity residuals over the entire analysis period.*

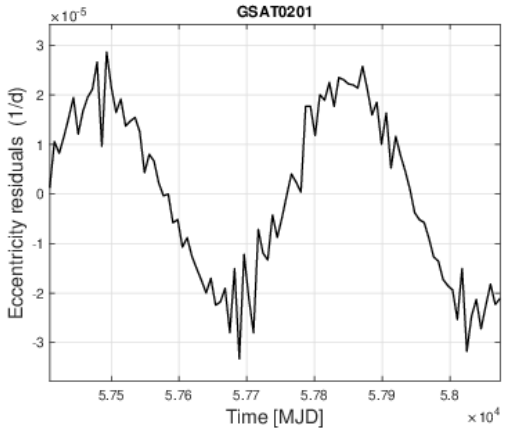

(b) *GSAT0201:long-term evolution of the satellite's eccentricity residuals in the period 2016 - 2017.*

Figure 4.14. *GSAT0201: residuals on 7-day of the satellite's eccentricity.*

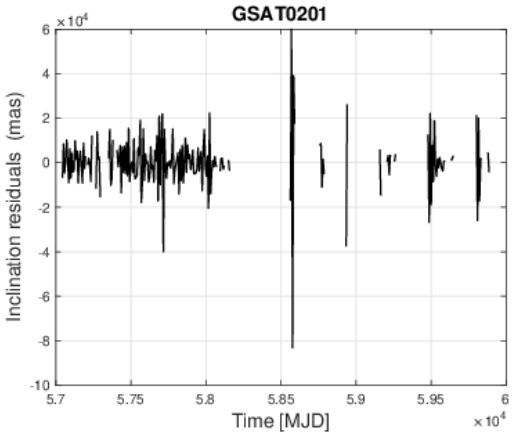

(a) *GSAT0201:long-term evolution of the satellite's inclination residuals over the entire analysis period.*

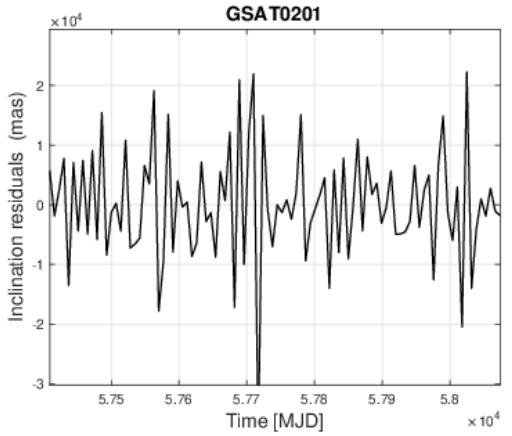

(b) *GSAT0201:long-term evolution of the satellite's inclination residuals in the period 2016 - 2017.*

Figure 4.15. *GSAT0201: residuals on 7-day of the satellite's inclination.*

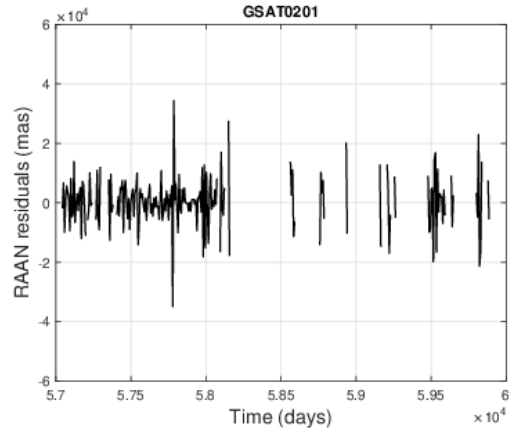

(a) *GSAT0201:long-term evolution of the satellite's RAAN residuals over the entire analysis period.*

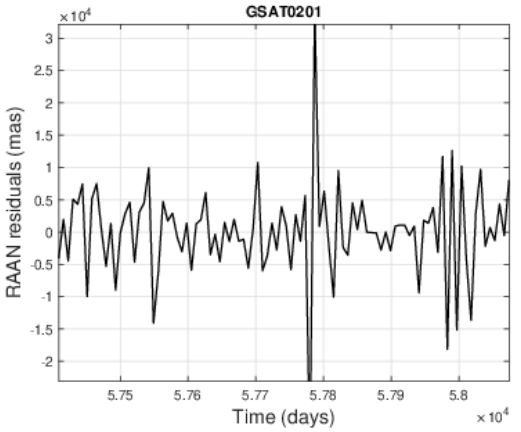

(b) *GSAT0201:long-term evolution of the satellite's RAAN residuals in the period 2016 - 2017.*

Figure 4.16. *GSAT0201: residuals on 7-day of the satellite's RAAN.*

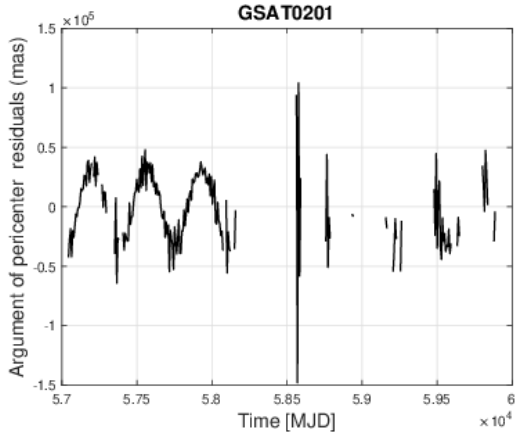

(a) *GSAT0201:long-term evolution of the satellite's argument of pericenter residuals over the entire analysis period.*

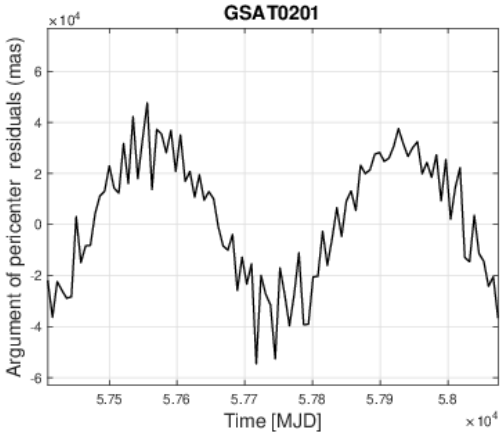

(b) *GSAT0201:long-term evolution of the satellite's argument of pericenter residuals in the period 2016 - 2017.*

Figure 4.17. *GSAT0201: residuals on 7-day of the satellite's argument of pericenter.*

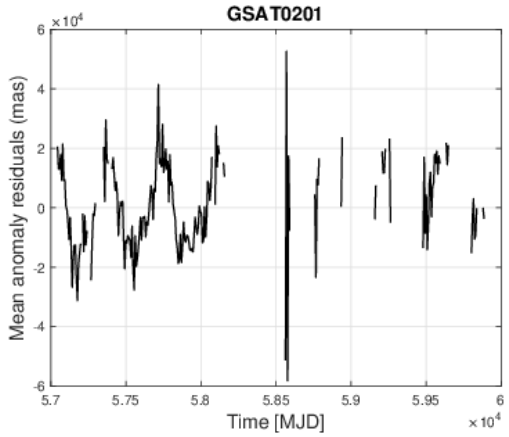

(a) *GSAT0201:long-term evolution of the satellite's mean anomaly residuals over the entire analysis period.*

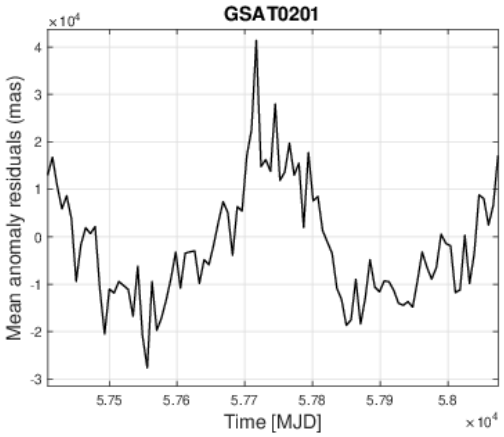

(b) *GSAT0201:long-term evolution of the satellite's mean anomaly residuals in the period 2016 - 2017.*

Figure 4.18. *GSAT0201: residuals on 7-day of the satellite's mean anomaly.*

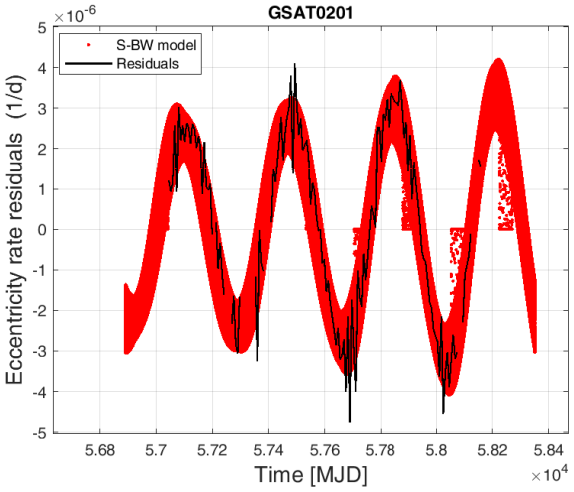

Figure 4.19. *GSAT0201: direct comparison of the eccentricity rate residuals with the corresponding prediction of the S-BW model on a 4-year timespan.*

For each figure, the plot on the left shows the residuals over the entire analysis period, *i.e.* over about 8 years, while the plot on the right shows the residuals we obtained over the 2-years period considered by the GREAT experiment: 2016 - 2017. The residuals plotted over the entire period clearly show the numerous gaps due to the non-convergence of the state-vector during the data reduction due to the scarcity of NPs for this satellite. On the contrary, the residuals obtained for the years 2016-2017 period do not show any discontinuity. This confirms the success of the observation campaign carried out by the ILRS stations in favor of the GREAT experiment for the two Galileo-FOC satellites in elliptical orbit.

As we expected, in this particular case of preliminary POD, the relativistic effects are completely masked by the imperfections of the dynamical model we used. In fact, most of the figures indicate the presence of non-modelled effects with an annual periodicity in the various orbital residuals. This is less evident in the residuals in inclination and in the right ascension of the ascending node, but it is well evident in all other cases. This clearly indicates the poor modelling of direct solar radiation for Galileo-FOC using a cannonball model, which on the contrary is a good approximation for passive and spherical in shape geodetic satellites, such as LAGEOS [126].

This is indirectly confirmed in Fig.4.19 and Fig.4.20, where the residuals in the eccentricity rate and in the argument of pericenter rate, rescaled per day, are compared with the predictions of our S-BW model presented in §3.5.2, Fig.3.13 (a) and in Fig.3.16 (a), and computed on a 4 years period. In this case, the S-BW model is able to explain almost all of the residuals currently obtained with the POD based on the cannonball model, in particular the annual oscillation. This results suggests that it is possible to use the accelerations obtained by our S-BW model (as well as the accelerations we will obtained in the future from more performing spacecraft models that we are gradually building) as input data for the `GEODYN II` software to fill its modelling gaps. This will certainly improve the overall dynamical model and the POD data reduction, thus facilitating the extraction of the relativistic precessions effects from the orbital residuals.

4.2.1 Towards relativistic precessions measurements

The results presented in the previous section are remarkable in view of the relativistic precessions measurements, since they give an indication on how the dynamical model in `GEODYN II` can be adapted with our S-BW in order to improve the modelling of the perturbing effects and thus reduce the orbital residuals from which these relativistic effects will be extracted.

Obviously, the current level of modelling of non-conservative forces and, in particular, of the direct solar radiation pressure, is not sufficient for a direct measurement of relativistic precessions. For example, in the case of the relativistic precession of the argument of pericenter of GSAT0201 (given by the sum of the Schwarzschild and the Lense-Thirring precessions, equal to ~ 423.5 mas/yr, see Tab.3.2) the result should be extracted, for instance, from the average value of the

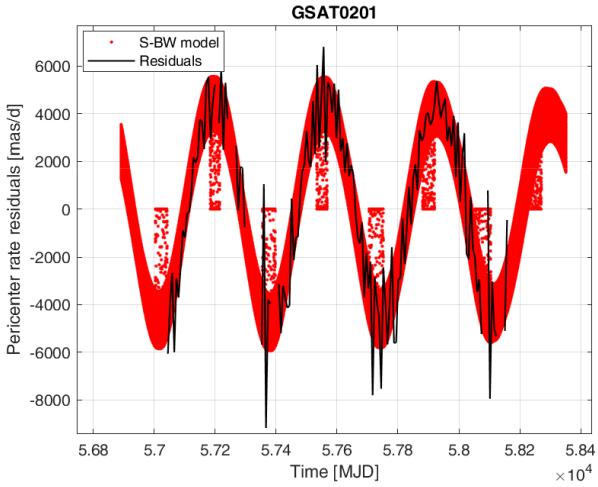

Figure 4.20. *GSAT0201: direct comparison of the argument of pericenter rate residuals with the corresponding prediction of the S-BW model on a 4-year timespan.*

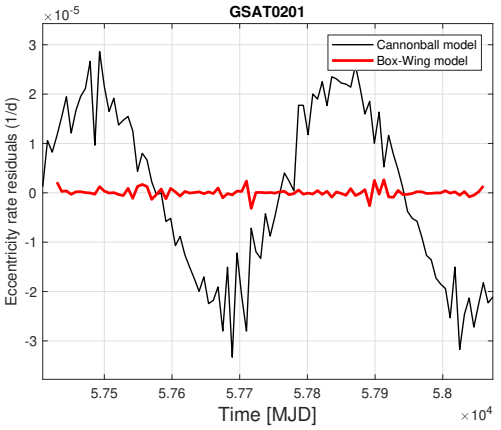

(a) *GSAT0201: long-term evolution of the satellite's eccentricity rate residuals over the 2-years of the GREAT analysis (2016-2017).*

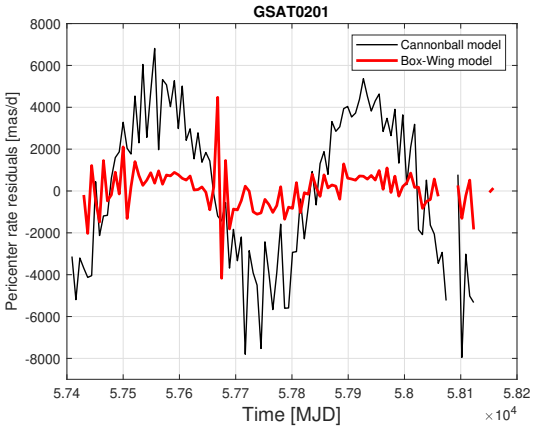

(b) *GSAT0201: long-term evolution of the satellite's pericenter rate residuals over the 2-year of the GREAT analysis (2016-2017).*

Figure 4.21. *GSAT0201 cannonball model vs S-BW model: residuals on 7-day of the satellite's eccentricity and argument of pericenter.*

pericenter rate residuals reported in Fig.4.17(a) or in Fig.4.20.

Unfortunately, both the long-term annual oscillation that characterises the residuals in the rate of the argument of pericenter of the satellite, and the shorter-term ones superimposed on it, provide an average value that completely masks the prediction provided by GR. In fact, from Fig.4.20, it is implicit that the incorporation of the S-BW model for the satellite in the POD is largely capable of absorbing the long-term annual oscillation in the pericentric rate residuals, but the higher frequency variations will not be certainly absorbed.

To show the improvement we can achieve with our S-BW, we have inserted the perturbing accelerations derived from our S-BW into the `GEODYN II` software instead of the cannonball. This was made possible by providing `GEODYN II` with two external files in binary format, one for the acceleration produced by the SRP on the box-wing model of the satellite, and one for the corresponding attitude of the satellite according to the law introduced in §2.5.

The results are given in Fig.4.21 where the residuals of the eccentricity rate and the argument of pericenter rate are shown for GSAT0201. Here we compare the new residuals obtained with `GEODYN II` by using our S-BW accelerations and the residuals obtained with the cannonball model (black).

As can be seen, the improvements in residuals reduction are significant: about a factor of 20,

or greater, in the maximum amplitude for the eccentricity rate and about a factor of 3 smaller in amplitude in the case of the argument of pericenter rate. However, these improvements are not sufficient to extract the relativistic precessions effects in a simple way. Indeed, the new residuals in the rate of the argument of pericenter are still characterised by a long-term oscillation with annual periodicity, in addition to the expected high-frequency oscillations. This aspect will be further explored but, from a preliminary analysis, we have estimated that the residual annual oscillation is due to a transversal acceleration of such periodicity and maximum amplitude of the order of 1.5×10^{-8} m/s^2. For instance, the mean value of the residuals of Fig.4.21 (b) in the case of the S-BW model, is about 30 times greater than the prediction of GR for the combined Schwarzschild plus Lense-Thirring precession (and about 300 times greater in the case of the cannonball model). This difference with the expected value according to GR is noticeable. However, it is not considered as an insurmountable obstacle to measuring relativistic precessions. There are mainly two reasons that support this consideration: one lies in the further improvement of the perturbations modelling and another in the different modalities with which the relativistic precessions can be extracted from the orbital residuals.

Regarding the first observation, the first step will be to achieve an improved Box-Wing model based on a more detailed characterisation of the optical properties of the satellite's face that constantly looks towards the ground. The second step consists of further improving the FEM model introduced in §3.6 and deeply explained in [30]. These improvements in the SRP model are estimated to be approximately a factor of 100 or 200 in the orbital residuals compared to the cannonball model. Only after these improvements will it be physically meaningful to consider the perturbations due to terrestrial albedo and infrared radiation.

About the second one, it is important to stress that the residuals in the various orbital elements do not simply show noise superimposed on the relativistic effects to be measured. They mainly show other effects that are not modelled or are poorly modelled in the dynamical model, primarily of a periodic nature. Therefore, our strategy will be to integrate the residuals in the rate of the orbital elements, as for example in the case of the rate of the argument of pericenter, thus obtaining that the periodic effects integrate and remain periodic and overlap with the linear trend of a relativistic nature. The integration process also acts as a filter, so that the effects on the pericenter rate due to periodic oscillations of a higher frequency are "mitigated". Consequently, measuring the slope will therefore provide the relativistic precession we are looking for, *i.e.* what was in the mean of the orbital element's rate before the integration is now in the slope of the element itself. Of course, it is important that the time step of the analysis is long enough to include an integer number of (possible) unmodelled long-term periodic effects, which then average their effect on the mean of the residuals, or the slope of the integrated residuals, to zero. Regarding the possible lack of normal points for the satellites, the measurement of relativistic precessions can still be attempted over a long time span by means of the statistical analysis used in [28].

4.3 The SLR Tracking Campaign for the G4S_2.0 Project

The results of the PODs in the previous section show that the scientific community does not always possess an adequate number of normal points (NPs), especially for satellites in elliptical orbits. In Fig.4.22 the number of observations, *i.e.* NPs, for GSAT0201 and GSAT0208 satellites are plotted during the period from 12-Sep-2014 to 02-May-2023.

We can see that the GSAT0208 satellite, although it was launched after GSAT0201 (see Tab.2.3 in §2.4), has been subject to a greater number of observations than the satellite in elliptical orbit. Tab.4.2 summarises, for the two satellites, the total number of NPs and their average value per year and per day. The latter value was also calculated during the 2-years (2016-2017) campaign of the ILRS for the GREAT project. As can be seen, the average number of NPs for GSAT0201 during this 2-year period is more than twice the average for the entire 8-year period considered. Conversely, the bottom line (no-GREAT) gives the average number of NPs per day after removing the 2-year period of the GREAT analysis with the dedicated SLR campaign.

This represents a delicate aspect for our Fundamental Physics measurements, since we are primarily interested in the analysis of the orbits of GSAT0201 and GSAT0202 for the measurements of relativistic precessions. This scarce number of NPs for satellites in elliptical

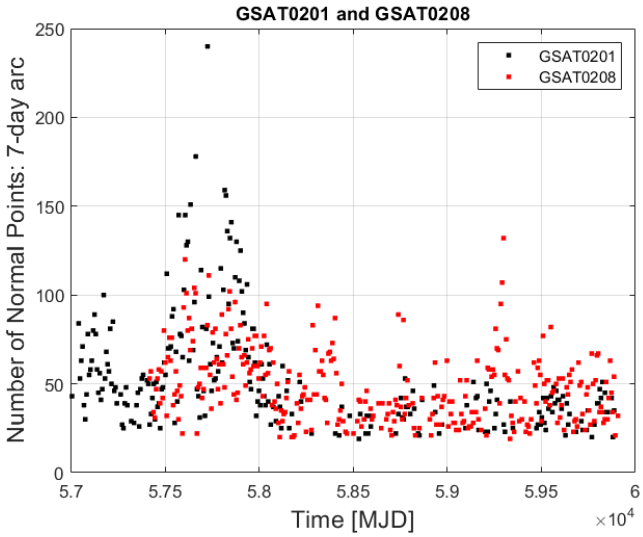

Figure 4.22. *GSAT0201 (E14) and GSAT0208 (E08): direct comparison of the available observations in the NPs format up to November 25, 2022.*

orbit is unfortunately present despite the aforementioned ILRS campaign carried out for the GREAT project[6].

Indeed, if we see, for example, Fig.4.14(b) it is evident that during the 2-years of the SLR campaign dedicated to GREAT, there is always the convergence of the state vector on 7-day arcs, while if we go outside there are many gaps Fig.4.14(a), because there are few normal points. From our `GEODYN II` analysis, we can deduce that at least 10 NPs per day are required to obtain a reliable and sufficiently robust POD.

Normal Points	GSAT0201	GSAT0208
Number of NPs	13,244	15,249
NPs/yr	1661	2235
NPs/d	4.5	6.1
NPs/d (GREAT)	10.9	9
NPs/d (no-GREAT)	2.7	5.1

Table 4.2. *Normal Points statistic for GSAT0201 and GSAT0208 on the respective time spans of the analyses performed with `GEODYN II`.*

Therefore, an increased number of SLR data is important to improve the POD of the satellites in the context of G4S_2.0. This is the main motivation that has led the G4S_2.0 team to ask for a dedicated SLR campaign to the ILRS. The request was approved and the SLR campaign started on 20th January 2024[7].

Specifically, more SLR data are useful to reduce systematic errors in the measurements to be performed. As already stressed in §4.1.1.2, orbit modelling errors are strongly correlated to the clock solutions and SLR data are essential to characterise orbital radial errors in the solutions provided by IGS Analysis Centers. In fact, the radial systematic errors are one:one correlated with the on-board clock solution. Since these systematic errors are mainly due to the mismodelling of the direct solar radiation pressure, it will be useful to have a campaign long enough to account for the variation of the $\beta_\odot$ angle, *i.e.*, the Sun height with respect to the orbital plane (already introduced in §2.5) whose period of variation is equal to the Draconit year, very close to 365 days.

[6] A further observation campaign of three months was carried out by ILRS for the ESA project called GASTON, for the search for Dark Matter of galactic origin.

[7] A dedicated online tool was developed to consult continuously the progress of the laser tracking observations https://g4s-duepuntozero.iaps.inaf.it/.

Moreover, we are interested to exploit the Full-Rate data during the penumbra transitions to improve the POD during these delicate shadow-light passages, and vice versa, of the satellites. In addition, Full-Rate data are appropriate for the determination of the spacecraft attitude.

Since the two satellites in elliptical orbit: GSAT0201 and GSAT0202 are mainly involved in the Fundamentals Physics objectives of the project, we have proposed a 2-year campaign for these two satellites. For the satellites in nominal orbit and the measures to constrain Dark Matter, we have proposed a 3-month campaign. The campaign is limited to few hours per week to limit the ILRS stations burden (usually with the determination of 2 NPs per pass).

The list of satellites to be tracked is as follows:

- Satellites in elliptical orbit (auxiliary slot):
  - GSAT0201 (E18)
  - GSAT0202 (E14)
- Satellites in nominal orbit (orbital plane A):
  - GSAT0210 (E01) A02
  - GSAT0206 (E30) A05
  - GSAT0205 (E24) A08
  - GSAT0211 (E02) A06
  - Satellites in nominal orbit (orbital plane B):
  - GSAT0101 (E11) B05
  - GSAT0102 (E12) B06
  - GSAT0221 (E15) B02
  - GSAT0203 (E26) B08
  - Satellites in nominal orbit (orbital plane C):
  - GSAT0209 (E09) C02
  - GSAT0208 (E08) C07
  - GSAT0103 (E19) C04
  - GSAT0212 (E03) C08.

Chapter 5

Atomic clocks and Fundamental Physics

In addition to the dynamical model and the POD, we are also interested in the atomic clocks of the Galileo FOC constellation. In fact, we use their data to put constraints on the galactic Dark Matter and, in the future, to perform the gravitational redshift measurement.

This Chapter focuses on the basic concepts of an atomic clock and its characteristics, such as its signal and the frequency stability. At the end, a brief overview on the applications of atomic clocks data in Fundamental Physics is given.

5.1 Basics of atomic clocks

Accurate and ultra-stable space-qualified atomic clocks are recognised as critical and indispensable equipment for GNSS. This is because they provide the timing precision and accuracy required for the ranging measurements [127]. Ranging measurements are calculated by measuring the signal propagation times. Positioning accuracy and precision depend on ranging accuracy and precision, which in turn depend on the accuracy and precision of the on-board clocks. Atomic clocks can keep time more accurately and consistently because they have much better frequency stability and accuracy than conventional oscillators. For example, a very good space-qualified ovenized crystal oscillator (OCXO) will have a 24-h timekeeping uncertainty corresponding to a position error of about 500 m, while a rubidium atomic clock will have a 24-h timekeeping uncertainty corresponding to a position error of about 5 m [127].

In simple words, an atomic clock is based on a system of atoms in one of two possible energy states. A group of atoms in one state is prepared and then exposed to microwave radiation. If the frequency radiation is the resonance frequency of the atom, an electron will rise to the higher energy state. Then, from this state, it goes to the lower energy state. In this transition, the atom releases energy at a specific frequency which is characteristic of the type of atom. A way of detecting this frequency and using it as the input to a counter is all that is needed to make an atomic clock.

More specifically, all the atomic clocks currently used on board GNSS satellites have a similar architecture [127]: a local oscillator (typically a high performance OCXO) is frequency-locked to an atomic hyperfine transition[1] frequency [128]. The clock physics package allows the local oscillator to interrogate the reference atomic transition frequency and generates a correction signal that constantly drives the local oscillator frequency toward the atom's resonant frequency.

The desirability of a particular atomic clock technology is determined by careful consideration of three different aspects: its timekeeping performance, its reliability and lifetime, and its size, weight and power requirements, usually summarised under the acronym "SWaP" [127]. Unfortunately, this typically means that none of these features can be optimised in isolation but a balanced trade-off between all three is required, with different compromises based on different system requirements.

[1] Hyperfine transitions are chosen as the frequency references for GNSS atomic clocks because their frequencies fall in the microwave regime, convenient for practical electronics engineering.

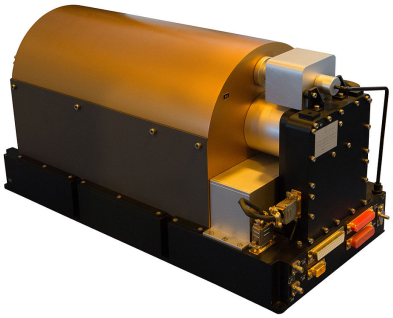

(a) *The Passive Hydrogen Maser (PHM).*

(b) *The Rubidium Atomic Frequency Standard (RAFS).*

Figure 5.1. *ESA Galileo's clocks. The PHM is the master clock onboard each satellite. It is an atomic clock which uses the ultra stable* 1.4 *GHz transition in a hydrogen atom to measure time to within* 0.45 *ns over* 12 *hours. A RAFS is used as a second, technologically independent time source. It is accurate to within* 1.8 *ns over* 12 *hours. Credits: ESA.*

Today, there are several types of atomic clocks and the main differences among them are based on the element and the method used to measure time. The caesium (Cs) atomic clock is the most widely used and accurate, being used to define the second, the SI unit time. Other types of atomic clocks use different elements, such as hydrogen or rubidium (Rb). The Rb atomic clock employs the oscillations of rubidium atoms. Although slightly less accurate than Cs clocks, Rb clocks are more portable and find applications in GNSS and scientific research. Regarding the hydrogen atomic clocks there are two primary types: active hydrogen masers (H-active or AHM) and passive hydrogen masers (H-passive or PHM). Both devices use the natural frequency of hydrogen atoms to generate a very stable and precise signal of 1.420 GHz. AHM rely on the natural oscillations of hydrogen atoms without the need for external stimulation, whereas a PHM requires an external signal to excite the atoms and to tune the atomic clock frequency. Both clocks are used in applications requiring high accuracy and synchronization, such as satellite navigation, telecommunications and scientific research, although active masers have better short and long term stability.

In Fig.5.1 the atomic clocks on Galileo satellites are shown.

5.2 Clock signal, bias and relative frequency

In general, we know that a precision clock operates at a specific working frequency and produces a periodic, oscillating electronic signal (voltage or current) which is typically used for timekeeping and synchronization tasks. In most cases, this signal takes the form of a sine wave [129]:

$$V(t) = V_0 \sin\left(2\pi\nu_0 t\right). \tag{5.1}$$

Here, V represents the clock voltage output, V_0 is the peak amplitude output, and ν_0 is the working frequency. However, clocks are often subject to various factors that introduce noises into the clock system. These noises commonly affect the signal amplitude and phase, leading to two types of perturbations: amplitude perturbation and phase perturbation. Hence, the ideal function in Eq.5.1 can be refined into a more realistic model:

$$V(t) = \left[V_0 + \delta(t)\right] \sin\left(2\pi\nu_0 t + \phi(t)\right). \tag{5.2}$$

In this case, V represents the actual clock voltage output, V_0 is the nominal peak amplitude, ν_0 is the unperturbed nominal working frequency, while δ and ϕ represent amplitude and phase perturbations, respectively. Additionally, we can define the nominal angular frequency as:

$$\omega_0 = 2\pi\nu_0 \tag{5.3}$$

Furthermore, we can express the total time-dependent amplitude of the signal as:

$$A(t) = V_0 + \delta(t) \tag{5.4}$$

and the total time-dependent phase of the signal as:

$$\Phi(t) = 2\pi\nu_0 t + \phi(t) = 2\pi\nu_0 \left(t + \frac{\phi(t)}{2\pi\nu_0}\right). \tag{5.5}$$

Therefore, a clock signal consists of two aspects: the function $\Phi(t)$ describes the background properties of the clock while the function $A(t)$ describes the output synchronization tool.

To describe the correct operation of the clock over time, we need to understand the behaviour of the time-dependent perturbations and, in particular, their practical effects. Let's begin by addressing the first type of perturbations, namely amplitude perturbation $\delta(t)$. Generally, this contribution is practically negligible compared to the nominal clock signal ($\delta(t) \ll V_0$) and it is not particularly interesting for our applications since it is related to the final electronic output $V(t)$. Instead, our focus is on the inherent properties of the clock and its capability of providing time and frequency references.

Upon closer inspection, we find that a phase perturbation can naturally give rise to a couple of effects. On the one hand, it introduces a time deviation, which is a time-dependent modification of the *time reading* of the clock compared to the nominal reading. On the other hand, it can lead to a frequency deviation, which is a time-dependent alteration of the clock's working frequency relative to its nominal value. Given these observations, we need to take three steps:

1. Introducing a proper mathematical definition for the time deviation and frequency deviation in terms of the perturbation $\phi(t)$.

2. Introducing a proper notion of stability that will be applied to these deviation phenomena.

3. Introducing a proper statistical estimator that will be able to quantify the stability.

In this paragraph we focus on the first point. Let us consider the definition of the total phase $\Phi(t)$ (Eq.5.5) and normalize it by the factor $2\pi\nu_0$ to obtain:

$$\frac{\Phi(t)}{2\pi\nu_0} = t + \frac{\phi}{2\pi\nu_0}. \tag{5.6}$$

At this point, we can introduce the first variable, namely the *time deviation* or simply the *bias* $x(t)$, defined as:

$$x(t) = \frac{\phi(t)}{2\pi\nu_0}, \quad x(t) = t_{\text{measured}} - t_{\text{nominal}}. \tag{5.7}$$

Therefore, $x(t)$ measures the difference between the actual clock time reading and the nominal clock time reading (the time reading in the absence of perturbation). In some cases, the bias $x(t)$ is also written as Δt and can be both positive and negative depending on the perturbation sign. In the first case, the clock precedes the nominal condition, while in the second case, it is delayed.

The simplest way to theoretically model the bias is by introducing two types of deviations. The first type consists of constant systematics, namely time offset x_0, frequency offset y_0, and a frequency drift D. The second type consists of time-dependent random variations $\epsilon(t)$, which are not deterministic. Therefore, we have:

$$x(t) \sim x_0 + y_0 t + \frac{1}{2} D t^2 + \epsilon(t). \tag{5.8}$$

However, this model is just an approximation and is valid in a number of scenarios but does not apply in all cases. Now, let us derive a proper quantity to parameterize the behaviour of the frequency deviations. We start again from the total phase definition and take the first-order derivative with respect to time:

$$\Phi(t) = 2\pi\nu_0 t + \phi(t) \quad \rightarrow \quad \frac{d\Phi(t)}{dt} = 2\pi\nu_0 + \frac{d\phi(t)}{dt}. \tag{5.9}$$

We then normalize both members of the expression by 2π and define the total frequency as the sum of the nominal frequency and the perturbation given by the $\phi(t)$:

$$\nu(t) = \nu_0 + \frac{1}{2\pi}\frac{d\phi(t)}{dt}\,. \tag{5.10}$$

At first glance, we can stop here and just consider the difference $\nu - \nu_0$ as the reference quantity. However, it is more convenient to introduce the dimensionless fractional or relative frequency:

$$y(t) = \frac{1}{2\pi\nu_0}\frac{d\phi(t)}{dt}, \quad y(t) = \frac{\Delta\nu(t)}{\nu_0}\,. \tag{5.11}$$

Then, we can conclude that the fractional frequency and bias are undeniably related:

$$y(t) = \frac{dx(t)}{dt} \tag{5.12}$$

where the rate of change of the fractional frequency, *i.e.*, its time derivative, is given by the second-order derivative of the bias:

$$\frac{dy(t)}{dt} = \frac{d^2x(t)}{dt^2} \tag{5.13}$$

The bias-fractional frequency relation is highly interesting. It indicates that the presence of a non-trivial time-dependent bias naturally generates frequency deviations. Simultaneously, the presence of frequency evolution *updates* the intrinsic clock-bias value. The expression for the resulting bias can be obtained by inverting Eq.5.12 via an integration over a given time interval:

$$\int_{x_a}^{x_b} dx = \int_{y_a}^{y_b} dt\; y(t) \quad \rightarrow \quad \Delta x(a,b) = \int_{y_a}^{y_b} dt\; y(t) \tag{5.14}$$

This relation tells us that if we have $x_a = 0$, then an effective bias will be generated. On the contrary, if we have $x_a \neq 0$ then an accumulated bias (or accumulated time) will be developed. In general, we can also compute the average value of the fractional frequency over an arbitrarily long period T:

$$\bar{y}(T) = \frac{1}{T}\int_0^T dt\; y(t)\,. \tag{5.15}$$

This quantity is a scalar that can be considered as a function of the period T. It is important to note that this point is highly non-trivial, as interesting phenomena can appear or disappear by varying the duration of the observation time T, providing a change of $\bar{y}$. For example, $\bar{y}(T)$ can remain approximately constant or slowly varying for small timescales, indicating an almost stationary evolution. However, for large timescales, $\bar{y}(T)$ can exhibit a rapid evolution, or vice versa. In common practice, it is widely known that we cannot measure instantaneous quantities directly and therefore we do not deal with continuum time-dependent functions. Instead, we acquire sampled values at specific time points. In this respect, we will end up with discrete time-dependent functions namely a time-series usually characterised by the observation time T, *i.e.* the time difference between the first and the last sample, the default sampling interval τ_0 and the relative (integer) multiples $\tau = n\tau_0$ often called as averaging times or integration times. In particular, for bias and fractional frequency we get

$$S_{x_i} = (x(t_1), x(t_2), ...), \quad x(t_i) = \frac{\phi(t_i)}{2\pi\nu_0}, \quad S_{y_i} = (y(t_1), y(t_2), ...), \quad y(t_i) = \frac{\Delta\nu(t_i)}{\nu_0}, \tag{5.16}$$

where $\tau_0 = t_{i+1} - t_i$ is the time interval between two samplings. The relation between bias and fractional frequency is given by a first order difference, *i.e.*

$$y(t_i) = \frac{x(t_{i+1}) - x(t_i)}{\tau_0} \tag{5.17}$$

and the first-order derivative of the fractional frequency is then given by a second order difference, *i.e.*

$$\begin{aligned} z(t_i) &= \frac{y(t_{i+1}) - y(t_i)}{\tau_0} \\ &= \frac{1}{\tau_0}\left[\frac{x(t_{i+2}) - x(t_{i+1})}{\tau_0} - \frac{x(t_{i+1}) - x(t_i)}{\tau_0}\right] \\ &= \frac{x(t_{i+2}) - 2x(t_{i+1}) + x(t_i)}{\tau_0^2} \end{aligned} \tag{5.18}$$

Eventually, the average value of the fractional frequency over a certain number n of sample is just:

$$\bar{y}_n = \frac{1}{n}\sum_{i=1}^{N} y(t_i)\,. \tag{5.19}$$

It is important to note that we can construct the fractional frequency (as well as its derivative or the average value) by considering a sampling time that do not align with the chosen standard τ_0, but rather with multiples of it, $\tau_n = n\tau_0$, for instance. This approach provides an overview on the behaviour of the fractional frequency on nonstandard time interval. This discussion allowed to derive the reliable tools describing the clock evolution over long time periods: bias $x(t)$ and fractional frequency $y(t)$ time-series.

5.3 Clock-noise, stability and Allan variance

Now we need to introduce the concept of *stability* of the (clock) time-series. In simple words, we can state that a time-series is stable if its values fluctuate around some nominal constant value and there is no divergent process.

The first approach to quantify the stability condition, is using the well-known standard deviation that measure the spread of the time-series values around the average. Let us suppose that the time-series consists of N fractional frequency samples $y(t_i)$ that cover an observation time of length T and with a sampling period τ_0. Then the common expression of the variance is

$$\sigma^2 = \frac{1}{N-1}\sum_{i=1}^{N}(y_i - \bar{y})^2 \tag{5.20}$$

where $\bar{y}$ is the average value of the fractional frequency. However, the average value of the fractional frequency is 0 by construction and the standard variance reduces to the average of the squared values

$$\sigma^2 =< y_i^2 > \ . \tag{5.21}$$

However, in the presence of common noises such as pink noise or random walk, the standard variance tends to diverge as the data set size increases. Thus, the standard variance is not a reliable statistical estimator of the fractional frequency stability of the clock.

The oldest, simplest and most commonly time-domain measure of frequency stability is the *Allan variance* [130]. Similar to the standard variance, it is a measure of the fractional frequency fluctuations but has the advantage of being convergent for most types of clock noise. There are several versions of the Allan variance that provide better statistical confidence, can distinguish between white and flicker phase noise and can describe time stability. The original *non-overlapping Allan*, or *two-sample variance*, AVAR, is the standard time-domain measure of frequency stability and is defined as [129]:

$$\sigma_y^2(\tau) = \frac{1}{2(M-1)}\sum_{i=1}^{M-1}\left[y_{i+1} - y_i\right]^2\ , \tag{5.22}$$

where τ indicates the sampling interval for constructing the AVAR. In particular, if the sampling interval is τ_0, then we construct the Allan variance considering the difference between two natural consecutive time-series values y_i. On the contrary, if the sampling interval is a given integer of

τ_0, *e.g.* $n\tau_0$, then we consider the difference between time-series values separated by n sampling, instead of one sampling (*i.e.* $M-1 \to M-2n-1$ in Eq.5.22). In addition, we can replace the difference between the fractional frequency values y_i with the bias values x_i to obtain

$$\sigma_y^2(\tau) = \frac{1}{2(N-2)\tau^2} \sum_{i=1}^{N-2} \left[x_{i+2} - 2x_{i+1} + x_i\right]^2 , \tag{5.23}$$

where the prefactor changes in accordance with a different number of sum entries. Therefore, we can take a fractional frequency time-series or a bias time-series, chose a given sampling interval and then compute the corresponding AVAR, which is a simple scalar quantity.

The Allan variance has been revisited and improved over the years. For example, a more accurate description of stability, than that provided by AVAR, is given by the so-called *Overlapping Allan variance* which is constructed by using overlapped samples, thus using all possible combinations of the dataset. It is worth noting that today the concept of Allan variance refers to a whole class of statistical estimators developed for a variety of purposes.

5.4 Allan stability analysis in a nutshell

Oscillator systems are highly sensitive and susceptible to various systematic effects due to specific oscillator characteristics such as technical imperfections and ageing, as well as to environmental factors like temperature, pressure, humidity, and dynamics. These effects manifest as *noise*, which refers to the almost inevitable background fluctuations around the value of the instrument's nominal variable. The noise therefore contributes to what is known as the background noise time-series. As a result, a clock will show background fluctuations around its nominal operating frequency. It is evident that if the noise contribution were significant, the data time-series would exhibit noticeable random spikes or dips, indicating a noisy signal.

In this context, the problem of characterising the noise performance arises, which can also be seen as the problem of estimating the stability of these instruments over short, medium, or long periods, depending on the circumstances. By performing an *Allan analysis*, *i.e.* following the evolution of the AVAR for different sampling intervals or averaging times, it is possible to derive the evolution of clock stability over the time. In Fig.5.2 we show schematically the Allan analysis of a single ideal clock and how a specific component dominates over the other contributions for a given range of averaging times. We also show the resulting, ideal sum. In Fig.5.3, we plot the schematic global evolution of the ideal sum, highlighting the scaling-laws for each epoch. In this scenario, the violet/blue components dominates until 10 seconds, then white noise dominates until 10^2 seconds, then we have the plateau of the pink/flicker components and as $\tau \sim 10^3$ seconds, brown/random walk begins to become relevant. It is important to outline how each noise component maintain the same scaling-law over time.

The application of the Allan analysis to the main atomic clocks lead to the results of Tab.5.1 where are shown the range of validity of the power-law τ^n and f^m for the various Frequency Modulated (FM)/Phase Modulated (PM) noise. The σ_y^2 of the white noise FM can be described with the power law τ^{-1} beyond 10 s for the Cs atomic clock while for the H-passive the description can be adopted since $\sim$ 1 s. At the same time, such power-law model holds at very large timescales in the case of an H-active clock. The σ_y^2 of the brown/random walk noise FM can be adopted on timescales of the order of some days in the case of the Rb clock, while weeks are required to adopt the same model for the Cs, or H-Maser.

Noise Type	Time	Freq	Cs	AHM	PHM	Qu	RAFS
White PM	τ^{-3}	f^2		≤ 100 s		≤ 1 ms	
Pink PM	τ^{-2}	f^1				≤ 1 s	
White FM	τ^{-1}	f^0	≥ 10 s	$100 - 10^4$ s	≥ 1 s		≥ 1 s
Pink FM	τ^0	f^{-1}	$\geq$ days	$\geq 10^4$ s	$\geq$ days	≥ 1 s	$\geq 10^4$ s
RW FM	τ^1	f^{-2}	$\geq$ weeks	$\geq$ weeks	$\geq$ weeks	$\geq$ h	$\geq$ days

Table 5.1. *Nominal range of applicability of the power laws for the standard noises in the case of some common atomic clocks.*

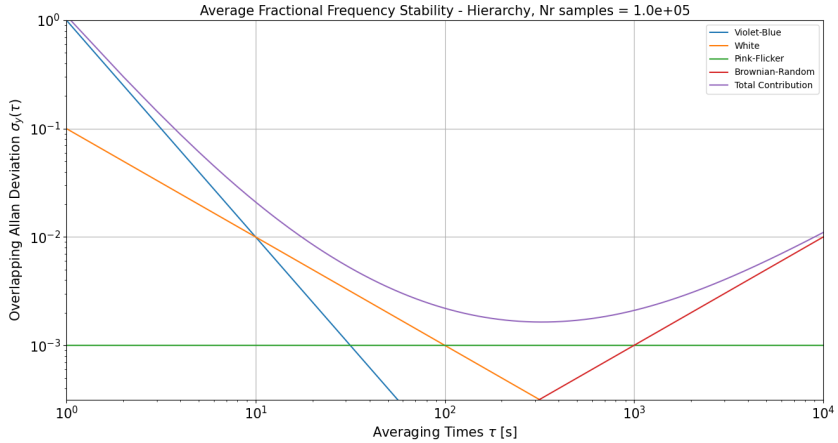

Figure 5.2. *Allan variance $\sigma_y^2(\tau)$ versus averaging time τ for an ideal clock. Blue, orange, green and red lines are the violet-blue, white, flicker and random walk frequency noise contributions, respectively. The purple line is the sum of these noise-components.*

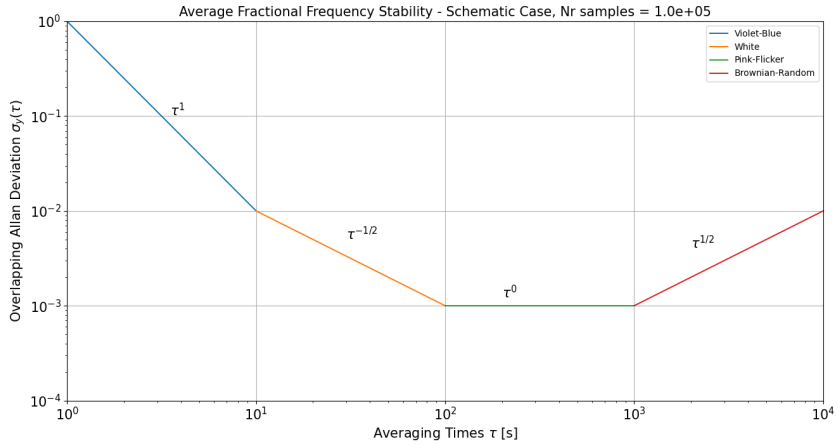

Figure 5.3. *The figure shows the ideal sum of the noise components in Fig.5.2, highlighting the dominant component at each epoch and its associated scaling law.*

An example of the Allan analysis on the PHM-A of the Galileo-FOC satellites GSAT0201 (E18) is shown in Fig.5.4.

5.5 Fundamental physics with atomic clocks

Beyond timekeeping and its applications, the GNSS on-board atomic clocks provide a scientific opportunity to investigate some aspects in Fundamental Physics.

For example, as already mentioned in Chap.1, in 2018 the European GREAT project used the atomic clocks data on GSAT201 and GSAT202 of the Galileo FOC constellation, to perform a sensitive test of the Local Position Invariance (LPI) [19] [18]. In fact, the structure of the orbit induces a periodic modulation of the gravitational potential that turns into a periodic modulation of the on-board atomic clock frequency f with respect to frequency of the terrestrial reference clock [17]:

$$\frac{\Delta f}{f} = (1+\alpha)\frac{\Delta U}{c^2} \tag{5.24}$$

where $\alpha = 0$ in GR.

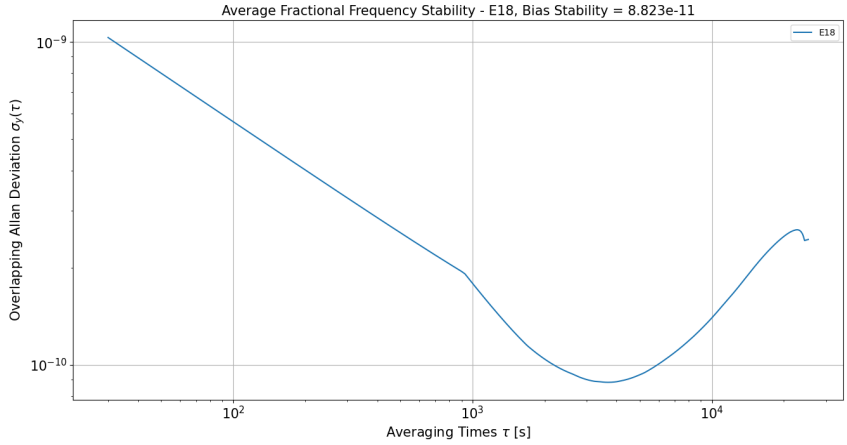

Figure 5.4. *The figure shows the overlapping Allan Deviation for the PHM-A of the satellite GSAT0201 (E18) relative to the operating periods within the GREAT project.*

The clock-data consist in the clock-bias time-series, estimated through the POD, in this case performed by ESOC. The construction of these data need some corrections in order to suppress GR contributions and to properly take into account the eccentricity of the orbits (the so-called Keplerian correction). The estimated clock-bias is then compared with the GR prediction in order to estimate the LPI parameter α. Finally, an accurate analysis on systematic effects must be conducted in order to estimate properly the error-budget. The main systematic effects are [97]:

- *Earth's magnetic field*: atomic clocks are sensitive to magnetic field which can be responsible of frequencies variations. For this reason, it is necessary developing a model that takes into account the orientation of the local magnetic field with respect to the satellite, in order to estimate the effect on frequencies.

- *Temperature variation* due to the change of the satellite orientation with respect to the Sun. We assume that the effect of temperature is minimum when the clock is exactly opposite to the Sun direction, *i.e.* when the Sun direction is aligned with the X-axis of the satellite, while it is maximum when the Sun direction is perpendicular to the X-axis. For this reason, all the onboard clocks are mounted on the shaded side of the spacecraft, to minimise the effect of temperature on performance.

- *Orbit and clocks solution*: SLR data allow to improve the orbit modelling and the evaluation of the clock-bias error, as radial systematic errors correlate one-to-one with the on-board clock solution.

Moreover, atomic clocks can be treated as a Dark Matter detector to search for such objects in the form of Domain Walls or new physical fields that interact with ordinary matter leading to frequency variation. This approach was followed in [22] by exploiting the GPS on-board atomic clocks. The result is a constraint on the quadratic interaction between the Domain Wall scalar field and the main fields of the Standard Model. The G4S_2.0 project also aims to do the same with the Galileo-FOC atomic clocks and this will be fully explained in Chap.6.

Chapter 6

Searching for Domain-Wall Dark Matter with the Galileo FOC constellation

Among the objectives of the G4S_2.0 project, there is the possibility of exploiting the Galileo FOC constellation to detect the possible presence of a particular candidate for Dark Matter, the Domain Walls.

In this Chapter, we present a qualitative discussion of the cosmological context, *i.e.*, the Big Bang theory, the related ΛCDM model and the various scenarios for Dark Matter. In particular, we focus on the one related to Domain Walls, eventually produced in the very early Universe by ultra-light scalar field(s). As Dark Matter is a very broad and controversial subject, we will not go into detail on all the models, observations and experiments, but refer to the specific references for more explanation.

The aim of our activities is to study the detection efficiency of the Galileo FOC constellation in order to evaluate the probability of detecting a Domain Wall signal in the atomic clock data. This requires the pre-processing of clock-data and the development of a pipeline that simulates the interaction between the Domain Wall and the satellite constellation.

6.1 Big Bang Theory and Dark Matter

The cosmological investigations of the first fifty years of the twentieth century have led to the development of the so-called *Big Bang theory*. This theory generally states that the early Universe finds itself in an extreme phase characterised by high temperature, density and pressure and by a nonzero curvature. This is followed by a thermal, adiabatic evolution which provides three main predictions or "pillars": the expansion of the Universe, the nucleosynthesis of the light elements and the presence of the cosmic microwave background (CMB) [131–136]. The Big Bang evolution can be realised through a number of models usually given specifying two sectors: a gravitational sector and a particle sector.

The simplest model in reproducing observational data emerged and consolidated between the '80s and '90s is known as the *curvature-flat ΛCDM model*, see Fig.6.1. This model is based on i) a gravitational sector described by the Einstein's General Relativity applied to a very simple Universe respecting the Cosmological Principle and ii) a field and particle sector divided into two contributions.

The first contribution to the field-and-particle sector is just the Standard Model (SM) of particle physics, describing the ordinary matter while the second contribution is known as the *dark sector*, characterised by a couple of components. The first is the so-called *Dark Energy* (DE) sector that (in this case) is realised via the Cosmological Constant (CC) Λ. This quantity should be responsible for the late-time accelerated expansion of the Universe discovered in the late '90s [137, 138]. In general, it is typically associated with the (some) fundamental vacuum energy and its very small value represents the most significant problem in current Fundamental Physics [139–143].

The second component is *Dark Matter* (DM), specifically the "particle" Cold Dark Matter

(CDM) hypothesis. This scenario should be justified both from a fundamental physics perspective, and phenomenologically, as it can explain some astronomical observations ranging from galactic and extragalactic dynamics to the formation of large-scale structures [144,145] or the physics of the CMB [146]. Specifically, these observations are explainable if this extra degree of freedom satisfies simple properties: massive, non-relativistic, non-baryonic, with suppressed electromagnetic properties and (eventually) feeble interaction with the Standard Model. If this assumption is true, we can wonder what the nature of this new particle would be.

The so-called *Weakly Interacting Massive Particles* or WIMPs, have always been considered the best candidate to DM since the '90s. They are thought of as heavy cold particles motivated by Grand Unified Theory (GUT) considerations or supersymmetric scenarios [147–153]. Many research lines were proposed in order to detect WIMPs or eventually to put bounds on their possible cross sections and masses: underground experiments, telescopes or collider physics [151–153]. However, most of the WIMPs experiments have not yielded very encouraging results so far.

The ΛCDM model fits the observational data well, as anticipated above, but it lies on three fundamental points (Cosmological Principle, Cold Dark Matter, Cosmological Constant) which are the subject of an intense debate. In addition, the model also presents a number of potential anomalies and tensions, see [154] for a complete survey. From this point of view, the current lack of detection of WIMPs (despite efforts) would be an indication of further destabilisation of such a realisation of the big bang theory. In light of these general difficulties, the cosmological community has begun to explore various alternatives to explain the corresponding astronomical observations, whether within or beyond the ΛCDM.

The first type of alternative is related to the gravitational field. For example, one can assume the existence of a *modified gravity theory* that is a generalisation of Einstein's theory of gravity. This theory should provide the known predictions of general relativity for some length scales and then correctly describe the observed phenomena on larger scales [8,9]. It is interesting that it seems possible to explain some of the astronomical observations, especially those concerning galactic dynamics, just by relying on more general solutions of GR itself. This has recently been shown by data from the GAIA experiment [10].

The second type of alternative concerns the particle sector. In particular, it is possible that cold dark matter is not made up of WIMPs, but of superheavy particles or primordial black holes [155–158], or that the CDM scenario is wrong, so we need mixed scenarios with lighter particles.

In the last 10-15 years, another particle alternative has emerged: light and ultra-light scalar fields and light or ultra-light pseudoscalar fields. This scenario is generically referred to as ultralight dark matter (ULDM). Ultralight scalars emerge ubiquitously in theories beyond the SM, they have extremely small masses, below 10^{-10} GeV, and they seem to be capable of easily explaining additional astronomical observations, such as galactic density profile. The direct detection of these extremely light particles does require alternative approaches, such as the use of resonant cavities and highly sophisticated atomic and interferometric techniques. In recent years, research in this area has experienced significant expansion, and for a comprehensive review on the topic, see [159]. However, these ultra-light fields can also contribute to the cold dark matter budget in the Universe or in the galactic halos via the formation of *topological defects*. In the next sections, we will explore this aspect into details, focusing on the Domain Wall scenario.

6.2 Dark Matter Topological defects

A scalar or ultralight scalar field often emerges in those scenarios that aim to describe the physics of the early Universe, above the electroweak scale. The field is typically described through a (cosmological) lagrangian equipped with a global or local symmetry (*e.g.*, a given gauge symmetry described by some gauge group) and can be characterised by a finite-temperature scalar potential, *i.e.*, with a shape that naturally changes as the Universe expands and cools. As a consequence, at some early epoch such a scalar field undergoes a generally (first-order or second-order) phase transition accompanied by a spontaneous breaking of the model symmetry. In particular, if the scalar potential and the field satisfy simple *requirements* and if one considers that the Universe could be characterised by causally disconnected regions, then the field does not experience a "homogeneous" symmetry breaking across the Universe, but rather takes different values in different causally disconnected regions. This triggers a process of spatial confinement

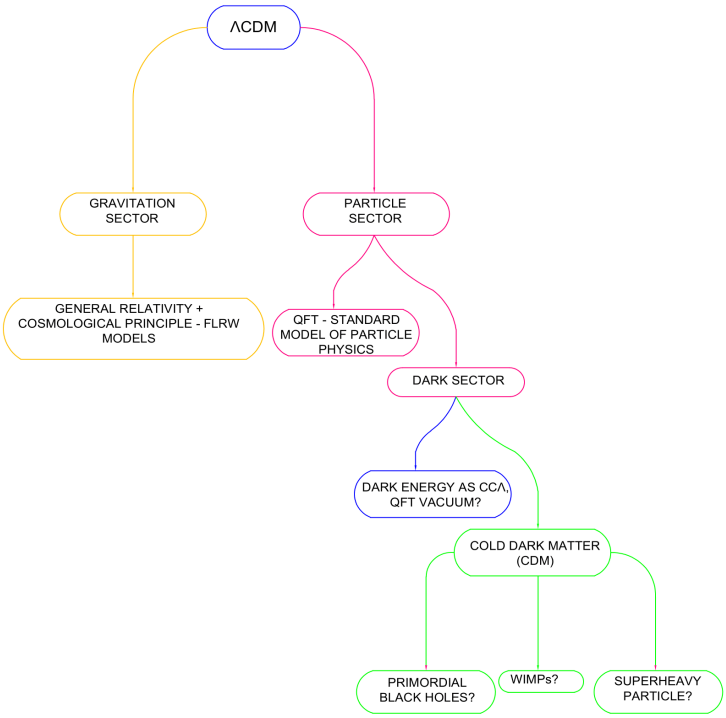

Figure 6.1. *Structure of the ΛCDM model.*

of the field known as the *Kibble–Zurek mechanism* [161–163]: the result is a (quasi) *solitonic* solution, namely, a field configurations with a localised and static energy, usually called *topological defects*.

In a Universe in $(3+1)$ dimensions, three types of topological defects can form depending on the broken symmetry and the number of spatial dimensions involved during the phase transitions:

- magnetic monopoles,
- cosmic strings,
- domain walls.

In general, the mathematical treatment behind solitonic solutions and topological defects depends, as mentioned, on the original underlying symmetries and the dimensionality, making it highly articulated and complex. Nevertheless, it is possible to provide a simplified treatment for pedagogical purposes to illustrate the spatial structure of a topological defect and the corresponding behaviour or distribution of the field [164].

In this context, consider a simple Lorentz-invariant effective Lagrangian for a neutral scalar field defined in a $(1+1)$-dimensional spacetime

$$\mathcal{L} = \frac{1}{2}\partial_\mu\phi\partial^\mu\phi - V(\phi) \tag{6.1}$$

with Hamiltonian density

$$\mathcal{H} = \frac{1}{2}\dot{\phi}^2 + \frac{1}{2}\left(\nabla\phi\right)^2 + V(\phi) \tag{6.2}$$

To obtain a topological solitonic solution, three conditions must be satisfied. The first condition is that the (positive) potential $V(\phi)$ must have multiple equivalent minima, or in other words, it must possess a *degenerate vacuum state*. The second condition is that the total energy of the system must be finite. This translates mathematically by requiring that at the boundaries of the spatial region ν where the system is defined, the kinetic, gradient, and potential terms

must vanish. This statement is then equivalent to demanding that the field reaches vacuum values at the boundaries of the region, typically at $(-\infty, +\infty)$. These boundary conditions are referred to as *topological conditions*. The third and final condition is that the energy must also be independent of time; therefore, the kinetic term is suppressed. The combination of these three conditions allows obtaining a field solution that is not confined to a single minima but rather connects, for example, two different minima of the vacuum state.

Let us enter in the mathematical detail. The condition on the staticity of the energy allows to write a simple Euler-Lagrange field equation, which is independent of time

$$\frac{\partial^2 \phi}{\partial x^2} - V'(\phi) = 0 \tag{6.3}$$

If one multiplies both sides of the equation for the spatial derivative of the scalar field, one can recover the so-called *Bogomolny equation*

$$\frac{1}{2}\left(\frac{d\phi}{dx}\right)^2 - V(\phi) = const \tag{6.4}$$

The requirement of a finite energy allows to set the integration constant to zero and thus obtaining

$$\frac{1}{2}\left(\frac{d\phi}{dx}\right)^2 - V(\phi) = 0, \tag{6.5}$$

from which

$$dx = \pm \frac{d\phi}{\sqrt{2V(\phi)}}, \quad \Delta x = \pm \int d\phi \frac{1}{\sqrt{2V(\phi)}} \tag{6.6}$$

Once a suitable potential $V(\phi)$ is assigned, it can be integrated to find a function $x(\phi)$. Then, one can invert to obtain the field solution $\phi(x)$. The corresponding energy is defined as the integral over the entire (Euclidean) space ν where the system is defined,

$$E = \int_\nu dx \left[\frac{1}{2}\left(\frac{d\phi}{dx}\right)^2 + V(\phi)\right] = \int_\nu dx \left(\frac{d\phi}{dx}\right)^2 \tag{6.7}$$

Naturally, it is not always possible to obtain an analytical solution. However, there are two very simple and instructive cases to study topological solutions: the $\lambda\phi^4$ model and the Sine-Gordon model, which are symmetric under the Z_2 group [164].

In the $\lambda\phi^4$ model, the potential has the form of a *double well*,

$$V(\phi) = \frac{\lambda}{4}\left(\phi^2 - v^2\right)^2 \tag{6.8}$$

and it is very similar to those studied in the simplest Higgs-inspired contexts. In particular, the degenerate vacuum state is characterised by two minima at positions $-v$ and $+v$ separated by a potential barrier $\lambda v^4/4$. Using the equation of motion Eq.(6.6) and setting $x_0 = 0$ for simplicity, we obtain the following double solution for the behaviour of the field

$$\phi(x) = \pm v \tanh\left(\sqrt{\frac{\lambda}{2}} v x\right) \tag{6.9}$$

The increasing solution is called a *kink*, while the decreasing one is called *antikink*. Note how the interpolation occurs near the value $x_0 = 0$ and exhibits a rapid growth of the curve, which, for an appropriate combination of model parameters, can approximate a step function. The energy density of the field can be calculated from the time-independent Hamiltonian density.

$$\rho(x) = \frac{\lambda v^4}{2\cosh^4\left(\frac{\lambda}{2} v x\right)} \tag{6.10}$$

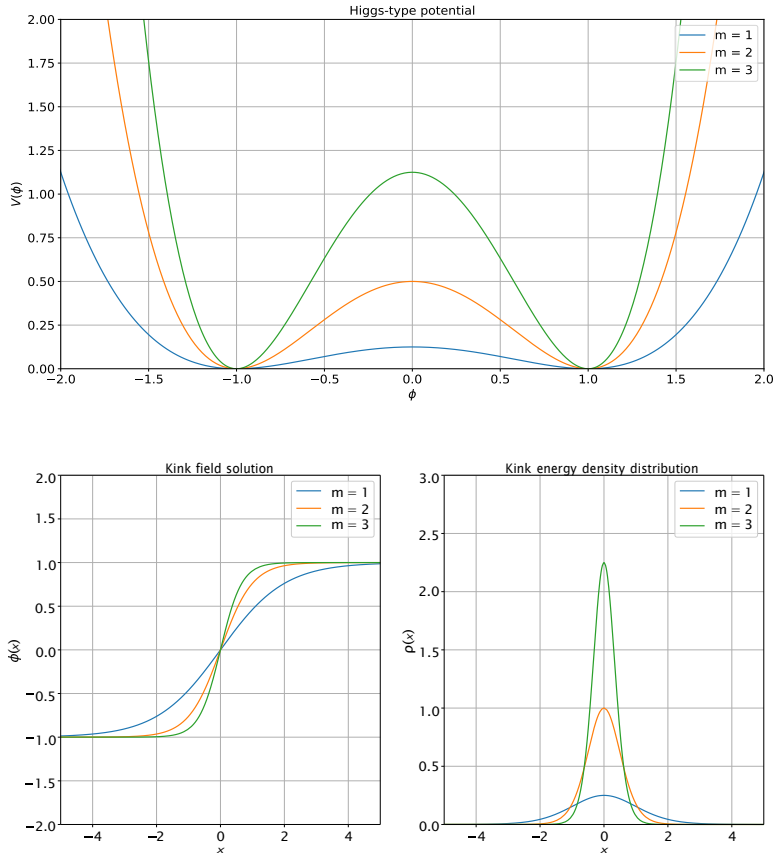

Figure 6.2. *First panel: $\lambda\phi^4$ model potential. Second panel: Kink solution and energy density distribution.*

and it is quite evident that it is strongly localised around $x_0 = 0$, precisely where the field curve grows rapidly. The integration of the energy density leads to the total, finite, and static energy of the system:

$$E = \frac{2}{3}\sqrt{2\lambda}v^2 \tag{6.11}$$

In general, we can expand the potential around one of the minima, for example v, to understand the local physics of small oscillations. This allows us to derive the fundamental mass of the field in the minimum, which results in $m_\phi = \sqrt{2\lambda}v$. The above results can be reformulated in terms of the fundamental mass of the field as follows:

$$\phi(x) = \pm v \tanh\left(\frac{m_\phi}{2}vx\right), \quad \rho(x) = \frac{m_\phi^2 v^2}{4\cosh^4\left(\frac{m_\phi v}{2}x\right)}, \quad E = \frac{2m_\phi}{3}v^2 \tag{6.12}$$

The form of the scalar potential, the increasing kink solution and the related energy densitie as function of the field mass m_ϕ are shown Fig. 6.2. These plots tell that as the field mass becomes larger, the potential barrier that separates the two minima becomes larger and this produces more localised and peaked topological solutions around $x_0 = 0$.

In the Sine-Gordon model, one has a periodic scalar potential

$$V(\phi) = \frac{\alpha^2}{\beta^2}\left(1 - \cos\beta\phi\right) \tag{6.13}$$

and it is the prototype potential that appears in pseudoscalar models like axions or axion-inspired. In this case, the degenerate vacuum state is characterised by an infinite number of minima, all

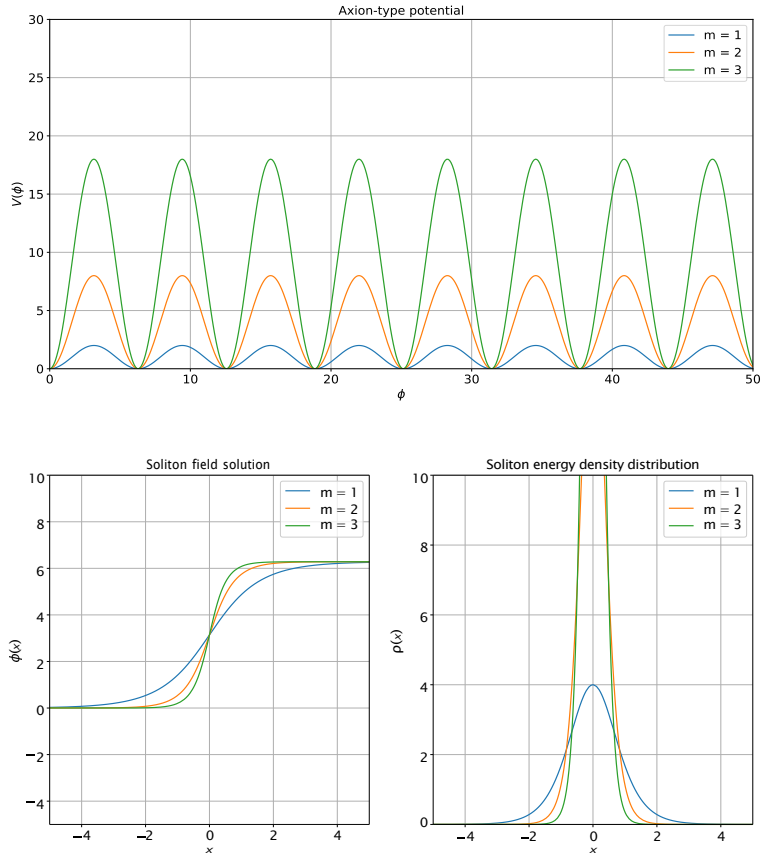

Figure 6.3. *First panel: Sine-Gordon model potential. Second panel: Soliton solution and energy density distribution.*

equivalent and equally spaced at $2n\pi/\beta$, where n is an integer. In this case, the double solution of the equation for $x_0 = 0$ takes the form:

$$\phi(x) = \frac{4}{\beta} \arctan\left(e^{\pm\alpha x}\right) \tag{6.14}$$

In this case, the increasing solution is called *soliton*, while the decreasing one is called *antisoliton*, and they exhibit a behaviour similar to what was observed in the case of kinks and antikinks. The calculation of the energy density reveals the strong localisation of the solution

$$\rho(x) = \frac{4\alpha^2}{\beta^2} \frac{1}{\cosh^2 \alpha x} \tag{6.15}$$

and the total energy reads

$$E = \frac{8\alpha}{\beta^2} \tag{6.16}$$

In particular, by performing an expansion around one of the minima, for example, $\phi = 0$, it is evident that the parameter α corresponds to the fundamental mass of the axion-like field, $\alpha = m_\phi$.

The scalar potential, the soliton solutions and the energy density distributions as function of the mass m_ϕ are reported in Fig.6.3. Thanks to the treatment carried out in this section, one can easily conclude that for topological solution in $(1+1)$ dimensions, the energy E is localised in the vicinity of a spatial point, producing a monopole solution or quasi-particle solution. On the other hand, moving to the case in $(1+2)$ dimensions, the system's energy E will be localised along an axis, resulting in a string solution. In the case of $(1+3)$ dimensions, the energy E

is localised on a plane, and we will have a Domain Wall (DW) solution. This last case is of particular interest. Indeed, a DW is a spatial structure that separates two regions of the Universe, *i.e.* the *domains* where the fundamental field has two different values, v_1 and v_2. Inside the wall, the field varies continuously with a non-zero derivative, interpolating between the two values v_1 and v_2. The model parameters, and in particular, the mass of the scalar field comprinsing the DW, determine the transverse dimension of the DW (via the usual Compton relation) *i.e.*, the region of space where the energy density is pronounced and interpolation occurs. In general, a *thick domain* appears in the case of a very low mass while a *thin domain* appears for a larger mass, as discussed above. In the next section, we will see what could happen if a thick DW interacts with an "ordinary" region of space.

6.3 Domain-Wall and ordinary matter interaction

An ultralight dark matter scalar that comprises a DW could manifest a non-trivial interaction with the ordinary matter, *i.e.* with particles and fields of the SM. The interaction can be modeled by introducing an effective low energy lagrangian (density) that contains the dark matter-standard model couplings or *portals*. In the simplest case, the ULDM field ϕ of the DW could interact with just one component of the SM, for example with the electron. In this scenario, the effective lagrangian can be written as the sum of the SM Dirac lagrangian for the electron field plus the portal term

$$\mathcal{L} = \bar{\psi} i\gamma^\mu \partial_\mu \psi - m_e \bar{\psi}\psi - \frac{\phi^n}{\Lambda_e^n} m_e \bar{\psi}\psi, \quad \Gamma_e = \Lambda_e^{-n} \tag{6.17}$$

where ψ is the electron field, $\bar{\psi}$ its adjoint, γ^μ the Dirac matrices, m_e the electron mass, Λ_e is the effective scale that describes the interaction, Γ_e is the corresponding field strength of the interaction while n is the generic field power. The result is a transient variation of the fundamental electron mass that occurs during the (Domain Wall-standard matter) time-of-interaction and can be computed as

$$m_{\mathrm{eff},e} = m_e + \frac{\phi^n}{\Lambda^n} m_e, \quad \frac{\Delta m_e}{m_e} = \Gamma_e \phi^n \,. \tag{6.18}$$

Basically, such variation depends on the coupling strength and the value of the scalar field inside the topological defect. However, we can expect additional interactions of the scalar field with the SM sector, *e.g.* interactions with photon, electron as well as nucleons (proton and neutron). Therefore a more general model could be [22]

$$\begin{aligned} \mathcal{L} &= \mathcal{L}_{\mathrm{SM}} + \mathcal{L}_{int} \\ &= \mathcal{L}_{\mathrm{SM}} + \frac{1}{4}\left(\frac{\phi}{\Lambda_\alpha}\right)^n F_{\mu\nu}F^{\mu\nu} - \left(\frac{\phi}{\Lambda_e}\right)^n m_e \bar{\psi}_e \psi_e - \left(\frac{\phi}{\Lambda_N}\right)^n m_N \bar{\psi}_N \psi_N, \end{aligned} \tag{6.19}$$

where $\Gamma_X \sim \Lambda_X^{-n}$. In this case we assume that the each portal X is described by a specific Λ_X or Γ_X parameter and the dark matter scalar appears with the same power n, in order to envisage a homogeneous interaction. In this case we would like to focus on the $n = 2$ scenario, along the lines of other recent studies [159]. Under this condition it is straightforward to show that if a dark matter Domain Wall interacts with a region of ordinary matter, then, during the interaction time, it will produce a re-definition for the fine structure constant, the electron mass, the proton mass [22]

$$\alpha^{eff} = \alpha(1 + \Gamma_\alpha \phi^2) \tag{6.20}$$

$$m_e^{eff} = m_e(1 + \Gamma_{m_e} \phi^2) \tag{6.21}$$

$$m_p^{eff} = m_p(1 + \Gamma_{m_p} \phi^2) \tag{6.22}$$

and the general QCD (Quantum chromodynamics) sector

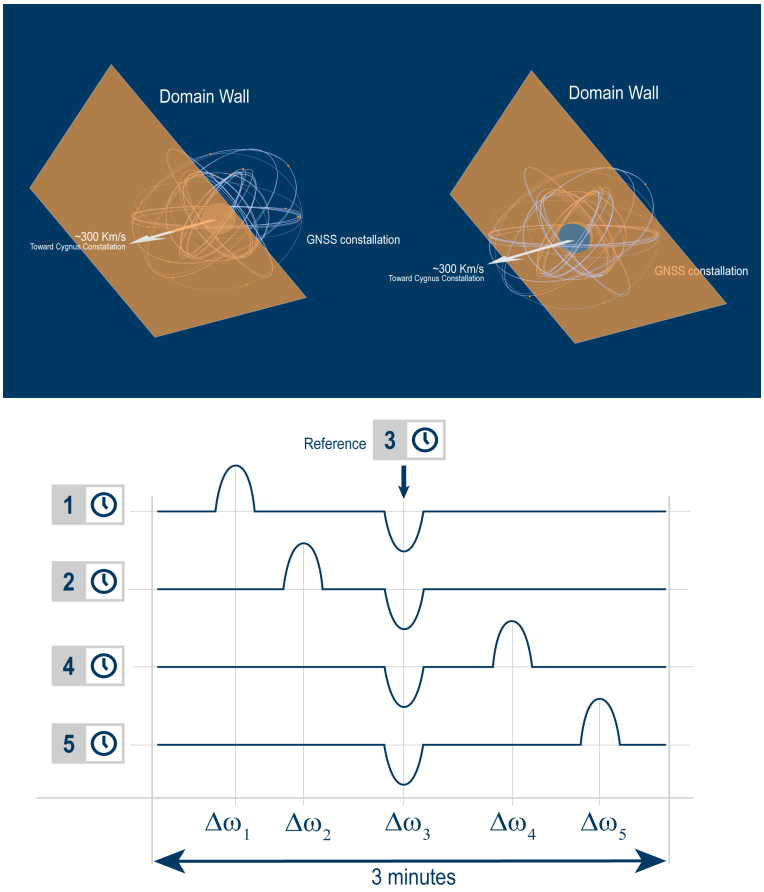

Figure 6.4. *A sketch of the Earth, moving towards the Cygnus constellation (left), crossing a Domain Wall (right). The interaction between the Domain Wall and the constellation of GNSS satellites arises and it appears in the clock-data (bottom). A simplified plot of the pseudo-derivative of the clock-bias is shown for only 5 clocks of the constellation. In this case, clock 1 and clock 2 are the first to interact with the DW, then the ground reference clock and finally clock 4 and 5.*

$$\left(\frac{m_q}{\Lambda_{qcd}}\right)^{eff} = \left(\frac{m_q}{\Lambda_{qcd}}\right)(1+\Gamma_{m_q/\Lambda_{qcd}}\phi^2). \tag{6.23}$$

The variation on a given fundamental constant X can be written as

$$\frac{\delta X}{X} = \Gamma_X \phi^2, \quad X = \alpha, m_e, m_p, m_q/\Lambda_{qcd}. \tag{6.24}$$

Therefore the transient variation is proportional to *i)* the scalar field value and *ii)* the coupling strength. It is important to outline that the value of the scalar field inside the DW typically varies with the space coordinate, as we have seen in the previous section.

6.3.1 Domain-Wall Dark Matter and GNSS Atomic Clock

In principle, a transient shift in fundamental constants could be indirectly detected using geospatial satellites. Indeed, a geospatial satellite is typically equipped with an atomic clock, crucial for communications and positioning purposes.

This atomic clock can be considered an environment of ordinary matter, and operate at some specific, nominal angular frequency ω_0. The nominal angular frequency depends on the clock type and is a certain function of the values of the fundamental constants of Nature, like the fine structure constant or the electron mass.

In this regard, suppose that a large-scale Domain Wall crosses the geospace at a certain epoch and interacts with the onboard clock of a given (constellation) satellite (see Fig.6.4). The

interaction with the standard model fields will induce a transient variation or transient shift in the fundamental constants, as we have seen above, and as a consequence also a transient frequency shift with respect to the fundamental working frequency ω_0 of the clock. The frequency shift can be computed as

$$\frac{\delta\omega}{\omega_0} = \sum_X K_X \frac{\delta X}{X} = \sum_X K_X \Gamma_X \phi^2 = \Gamma_{\text{eff}} \phi^2, \quad \Gamma_{\text{eff}} = \Lambda_{\text{eff}}^{-2} \tag{6.25}$$

and this is just a linear expansion in the fundamental transient shifts with proper weights K_X. Therefore, the total frequency variation depends on the total effective coupling Γ_{eff} which is a "function" of the clock type. Indeed some clocks could be more sensitive to variation in the fine structure constant while other clocks can also receive non negligible contribution from other sectors.

As an example, clocks operating in the optical range (10^{14} Hz), are basically sensitive to fine-structure constant α sector while more commercial clock operating in the microwave range (10^9 Hz), also manifest non-negligible contribution from the electron or nuclear sector. For example, for the clocks onboard of the GPS (Cs and Rb) and Galileo (H and Rb) constellations we have [160]

$$\Gamma_{\text{eff}}(^{87}\text{Rb}) = 4.34\Gamma_\alpha - 0.069\Gamma_{m_q} + 2\Gamma_{m_e} \tag{6.26}$$

$$\Gamma_{\text{eff}}(^{133}\text{Cs}) = 4.83\Gamma_\alpha - 0.048\Gamma_{m_q} + 2\Gamma_{m_e} \tag{6.27}$$

$$\Gamma_{\text{eff}}(^{1}\text{H}) = 4\Gamma_\alpha - 0.150\Gamma_{m_q} + 2\Gamma_{m_e} \tag{6.28}$$

Therefore, if the Domain Wall does not stop at the first clock but reasonably continues and crosses the entire constellation (or a large part of it), this transient frequency shift will propagate, generating a propagation pattern.

In general, the amplitude of the signal and the properties of the pattern will depend on the properties of the Domain Wall, which we will see in the next section. It is important to emphasize that the transient frequency shift is, in principle, time-dependent because the individual variations of the fundamental constants are time-dependent. Indeed, the single clock should interact with the field profile $\phi(x)$ as the Domain Wall moves and this simulates a variation of the field parameter value over time: $\phi = \phi(t)$. Therefore, rigorously:

$$\frac{\delta\omega(t)}{\omega_0} = \sum_X K_X \frac{\delta X}{X}(t) \tag{6.29}$$

In the next section, we will see the typical properties of a Domain Wall and the properties of a more general distribution of DWs potentially present in the halo of our galaxy.

6.4 Domain-Wall Dark Matter in the Milky Way

A typical ultralight dark matter scalar field possess a very low mass, much smaller than the mass of the electron neutrino $m_\phi < m_{\nu_e}$, for instance. As a result, the corresponding generated Domain Wall will be characterised by a relatively small or *thin* transverse dimension d, compatible with the Earth's radius $R_\oplus$

$$m_\phi \sim \ 10^{-14} \text{ eV}, \quad d \sim m_\phi^{-1}, \quad d \sim R_\oplus \tag{6.30}$$

Furthermore, we can model the scalar field space distribution as

$$\phi(x) \sim \begin{cases} 0 \text{ for } x \notin \text{DW} \\ f(x) \neq 0 \text{ for } x \in \text{DW} \end{cases}, \tag{6.31}$$

where $f(x)$ is the profile function inside the Domain Wall. In literature, there exist a number of scenarios for the function $f(x)$, *e.g.* flat or gaussian.

The Domain Wall is also equipped with an energy density that scales as the inverse of its size d [22]

$$\rho^{\rm DW}_{\rm inside} \sim \phi^2/d^2 \tag{6.32}$$

In the early universe the Domain Wall can be copiously produced via the Kibble-Zurek mechanism therefore one can expect an entire distribution or clouds. In order to model such distribution, it would be useful to introduce an average distance between the DWs, we call L that should be order of magnitude larger than the transverse dimension d of the single object $L >> d$. In light of this, the total energy density of the DW distribution can be easily computed as [22]

$$\rho_{\rm DW} = \rho^{\rm DW}_{\rm inside} d/L \tag{6.33}$$

This quantity can saturate the total Milky Way (halo) dark matter density, usually estimated as $\rho_{\rm DM} \sim 0.3$ or just represent a fraction.

The kinematics of a Domain Wall dark matter cloud can be modeled following the standard halo model. The incoming direction of a given Domain Wall would be that of the Cygnus constellation while the propagation velocity should be of the order of the galactic velocity

$$v_g \sim 300 \text{ km/s} \tag{6.34}$$

or even larger, in some cases. The quantity v_g also allows to define two crucial type of timescales. The first one is the average *encounter time*

$$T = \frac{L}{v_g} \tag{6.35}$$

that should be smaller than the observation time window one can use to put constraints on a Domain Wall passage $T_{\rm obs} > T$.

The second type of time timescale regards the Domain Wall interaction with the constellation. In particular we can define the *gnss-crossing time* as the time necessary for the Domain Wall to cross an entire GNSS constellation

$$t_{\text{gnss-cross}} = l_{gnss}/v_g \sim 170 - 180 \quad \text{s} \tag{6.36}$$

as well as the *clock-crossing (or interaction) time* as the time a given satellite or clock spends inside the Domain Wall environment

$$t_{\text{clock-cross}} = d/v_g < 30 \quad \text{s} \tag{6.37}$$

It is important to outline that $\rho_{\rm DW}$, v_g e T allow to reword the transient frequency shift as

$$\frac{\delta\omega}{\omega_0} = \Gamma_{\rm eff}\rho_{\rm DW} v_g T d \tag{6.38}$$

This is a crucial result since now the amplitude of the frequency shift is completely related to pure particle and astronomical parameters. In addition, this expression also allows to constrain the hypothetical Domain Wall properties like d (or m_ϕ) or $\Gamma_{\rm eff}$ or the related effective energy scale $\Lambda_{\rm eff}$, once an experimental bound on the frequency excursion is provided.

6.5 Domain-Wall search with GNSS atomic clocks

The fundamental question is if it is possible to detect a Domain Wall-induced propagating frequency glitch. In this respect, one should stress two points.

The first point is that one can eventually deal with some other physical mechanisms able to reproduce or mimick a similar propagating signal. Indeed, this would provide a sort of degeneration. In the geospatial context, the only systematic effect that can occur with similar propagation velocities is the solar wind. However, one should be able to recognize it because the position of the Sun is known and the particles of the wind do not impact on satellites in the Earth's shadow.

The second point is more subtle and concerns the elaboration of a recipe in order to effectively search for a Domain Wall event. The recipe has been developed by Roberts *et al.* [22] and is based on the analysis of the bias of the atomic clocks onboard the GNSS satellites. In the previous chapter, the bias has been defined as the difference between the effective time reading of the clock and (what should be) the nominal time reading of the clock. In this context, the clock-bias is labelled as $S^{(0)}$ and represents the difference between the effective time reading and a *nominal time reading* which is given by a terrestrial reference clock, that is

$$S^{(0)} = \text{time reading onboard clock} \; - \; \text{time reading reference clock} \tag{6.39}$$

The corresponding bias timeseries is provided with some sampling epoch τ which is 30 seconds for constellation like GPS or Galileo and is naturally characterised by a background noise. Consider a thin Domain Wall that approaches the geospace and interacts with a given onboard clock. In the continuous limit, the interaction should have and effective duration $\Sigma_t = t_{\text{clock-cross}} \ll \tau$ and should induce a frequency glitch that provides a positive *accumulated* bias, via the integral conversion (see previous Chapter)

$$\Delta t = \int_{\Sigma_t} dt' \frac{\delta\nu(t')}{\nu_0} \, . \tag{6.40}$$

This nontrivial bias excursion should then appear in the "pseudo-derivative[1] of the bias, *i.e*

$$S^{(1)}(t_k) = S^{(0)}(t_k) - S^{(0)}(t_{k-1}) \tag{6.41}$$

At the same time, as the Domain Wall passes the clock and impacts on the terrestrial reference clock, it induces a negative accumulated bias on the board clock. In the next subsection, a concrete example will be discussed.

6.5.1 Domain-Wall detection method application

As an example, let us consider an onboard target clock and a ground reference clock. $S^{(0)}$ is the sampled relative bias and $S^{(1)}$ the corresponding pseudo-derivative with a sampling epoch of 30 s. To simplify the discussion, one can assume that the nominal value of the bias is zero, *i.e. perfectly aligned clocks* and neglect the background noise. Then consider a thin Domain Wall that approaches the geospatial environment and in particular the first clock. The Fig.6.5 shows the interactions at level of the clock-bias.

If one considers the sampling time t_0, t_1, t_2, t_3 one can deduce no interaction is still occured: the bias is constant and pseudoderivative is also zero

$$S^{(1)}(t_2) = S^{(0)}(t_2) - S^{(0)}(t_1) = 0 \tag{6.42}$$

Assuming that the Domain Wall interacts with the clock between t_3 and t_4 it generates a transient shift and a corresponding accumulated bias that can be detected in the subsequent sampling time t_4. Indeed, the bias shows a non-standard amplitude h and the pseudoderivative reads

$$S^{(1)}(t_4) = S^{(0)}(t_4) - S^{(0)}(t_3) = h - 0 = h \tag{6.43}$$

As the Domain Wall leaves the target clock and moves further, it can be seen that the bias remains h, while the pseuderivative becomes zero at t_5 and remains zero until the Domain Wall reaches the ground clock.

[1] As stated in §5.2, we deal with discrete time-dependent functions (time-series). Therefore, their derivatives are not continuum time-dependent functions. In this context, we call the (discrete) "pseudo-derivative" of the bias the difference between two bias values without the relative time-normalization.

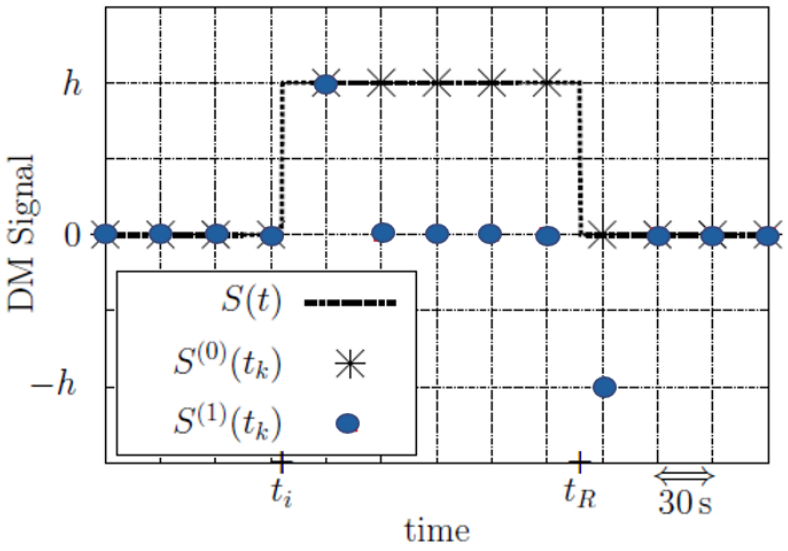

Figure 6.5. *Example of an ideal thin DW signal for a pair of identical clocks separated by a distance $l = v\,(t_R - t_i)$, where the DW crosses the first clock at time t_i and the second (reference) clock at time t_R. $S(t)$ is the ideal clock-bias signal, $S^{(0)}(t)$ is the real clock-bias signal sampled every 30 s, $S^{(1)}(t)$ is its sampled pseudo-derivative.*

$$\begin{aligned} S^{(1)}(t_5) &= S^{(0)}(t_5) - S^{(0)}(t_4) = 0 \\ S^{(1)}(t_6) &= S^{(0)}(t_6) - S^{(0)}(t_5) = 0 \\ S^{(1)}(t_7) &= S^{(0)}(t_7) - S^{(0)}(t_6) = 0 \\ S^{(1)}(t_8) &= S^{(0)}(t_8) - S^{(0)}(t_7) = 0 \end{aligned} \tag{6.44}$$

This simple computation shows that at the time t_4 one can observe an *anomalies* or a *spike* which represents the moment when the two clocks become disaligned. In the following, say between t_8 e t_9 the Domain Wall reaches the ground clock, giving the same frequency excursion and a positive accumulated bias. As a result, at the sampling time t_9 it is possible to observe a negative pseudoderivative

$$S^{(1)}(t_9) = S^{(0)}(t_9) - S^{(0)}(t_8) = 0 - h = -h \tag{6.45}$$

Then for $t > t_9$, the bias is completely re-aligned and the pseudoderivative comes back to zero via a negative spike.

The same happens for the other clocks of the constellation. We can therefore observe a spike that propagates throughout the entire network with a velocity compatible with that of the Domain Wall. In general a constellation of N satellites can exhibit a very complicated pattern. This pattern will be characterised by a couple of features. First of all, there will be a negative spike common for all the clocks and can be considered the *trigger event*. Then, there will be a distribution of positive spikes around the trigger. The positive spikes before the trigger, indicate that the corresponding clock have been reached by the Domain Wall before the ground clock while the positive spikes after the trigger, indicates that the remaining clock have been reached after the passage of the Domain Wall on the ground clock.

In light of this, the detection strategy is very simple: one should collect the bias time-series of the constellation clocks, search for trigger events and study the corresponding spikes distribution in order to reveal possible candidate events, *i.e.* plausible patterns.

In the following we will enter into details about the spike amplitude and the preliminary activities carried out to perform a reliable measure.

6.5.2 Signal amplitude expectation

The signal amplitude induced by a Domain Wall on the onboard clock can be compute by solving the integral equation for Δt Eq.(6.40). In order to do that, one should take into account both reliable time-dependency of the relative frequency and a proper interaction time. However, if one supposes that the relative frequency is almost constant during the interaction time (*i.e.* the effective coupling) and the interaction time one can be safety approximated by the ratio d/v_g, then a reasonable roughly estimates can be written as

$$S^{(1)}(t_k) \sim \delta\nu(t_k)/\nu \times t_{\text{clock-cross}}. \tag{6.46}$$

This expression allows to write an *average* value for the signal, that comes out as [22]

$$S^{(1)}_{avg} \sim \Gamma_{\text{eff}}\rho_{\text{DW}}d^2T, \tag{6.47}$$

which is almost independent from the profile of the thin Domain Wall [22].

Eq.6.47 relates the Domain Wall characteristics to the signal properties. This is interesting because, in the case of a Domain Wall detection, through this relation it is possible to deduce the properties of the detected Domain Wall. Otherwise, it allows to place un upper limits on these properties, defining which are the Domain Wall signals that we can exclude (as in the case of [22]).

6.5.3 Domain-Wall search within G4S_2.0

The current constellation of the Galileo FOC satellites may allow an improvement in DM constraints by exploiting the higher sensitivity of the on-board atomic clocks compared to the current GPS constellation [22]. The G4S_2.0 project aims to provide such constraints by using the time-series of the clock-bias related to the Galileo FOC atomic clocks.

Let us consider a very simple case: we assume that the scalar field inside the DW interacts only with the electron (Eq.6.17). In this case, there is no need to distinguish between the PHM and Rb clocks onboard of the Galileo FOC satellites, since the effective coupling strength is the same (see Eq.6.26). Therefore, this assumption ensures a homogeneous response from the clock network.

A description of the type of data we deal with and the pre-processing required for the analysis is given in the following section, §6.5.3.1.

Our goal is to look for a possible DW pattern through the Galileo FOC atomic clocks network. As previously discussed, it is characterised by:

1. a time-coincidences of negative delta-like signals in the clock-data, *i.e.* the trigger event.

2. a correlated sequence of positive delta-like signals around the trigger.

In order to provide a reliable statistical result for each possible crossing pattern, we need to study the statistics of our atomic clock-network. First, we performed a preliminary *false-alarm* analysis to evaluate the frequency of no-physical trigger events (see §6.5.3.2). A second aspect to analyse is the *detection efficiency* for DW signals of different amplitudes, *i.e.*, the probability to detect with our network a spike amplitude ($S^{(1)}$) induced by a DW in the clock-data. In order to do that, we developed a `Matlab` simulation code to describe a realistic interaction of the DW with the six selected Galileo FOC satellites (see §6.5.3.3). The simulation will allow us also to choose and fine-tune, a priori, the analysis parameters (*e.g.*, amplitude-threshold, time-window) required to reveal a possible DW signal in the data. If a DW pattern is found with a certain amplitude then, once estimated the false alarm and the detection efficiency, we would estimate a certain probability of detection. Finally, through Eq.6.47, it will be possible to reconstruct the DW properties. The absence of detection related to a certain DW amplitude, can also help us to give an upper limit, *i.e.*, which signals we can exclude and with what probability.

All these aspects will be deeply explained in the following sections.

6.5.3.1 Clock-data and pre-processing

The basic data we consider for our analysis are the time-series of the clock-bias produced by ESOC with the `NAPEOS` software. These data are contained in 1113 `RINEX clk 2.0` daily files, with a sampling rate of 30 s, whose names are given by "`esoc`" followed by the GPS week and the number of the day es. "`esoc18210.clk`". These time-series have been produced in relation to the GREAT project and cover a period of almost three years (30-Nov-2014 to 16-Dec-2017 *i.e.* from GPS week 1821 to 1943).

Two different types of data are included in these files: results from phase/pseudorange data analysis for a network of station/receiver (`AR data`) and satellite (`AS data`) clocks, all relative to a fixed reference clock (or ensemble) adopted in the analysis.

The first step is to gather the information about the satellite we are interested in from the files.`clk`. Until now, we have considered the following Galileo FOC: $E08$, $E11$, $E12$, $E14$, $E18$, $E30$. For each satellite we have created a file containing the time shift of the on-board clock with respect to the ground reference clock as a function of time. As can be seen in Fig.6.6, the original behaviour of these time-series is characterised by a couple of relevant features:

- a long-period linear trend with a slope of 10^{-5} s per day[2];
- discontinuities at the beginning of the day (daily-jumps) and lack of data for a certain time-period.

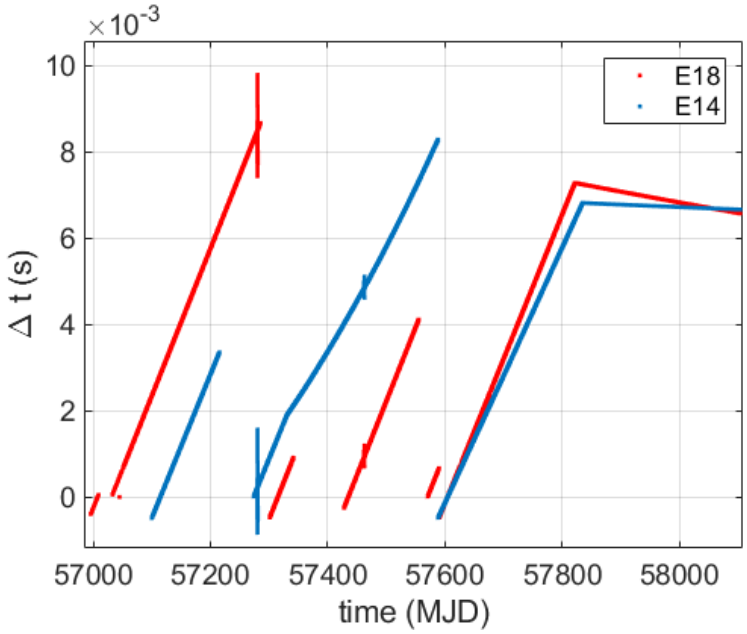

Figure 6.6. *Time shift of the onboard clocks of the satellites GSAT201 (E18) and GSAT202 (E14) according to the ESOC files.*`clk`

To remove these signal discontinuities, we have implemented a dedicated pipeline. First, we decided to divide the dataset into homogeneous periods, *i.e.* where the long-term drift is constant. We then removed the linear trend in each of the identified periods. Secondly, we removed the daily jumps by matching the first sample of a day with the last sample of the previous one. An example of the effect of the cleaning procedure is in Fig.6.7.

We then found the common clock operating periods of these six satellites: we find 37 common periods. A single period is identified by a couple of Modified Julian Dates (MJD): a starting date (`Start_MJD`) and a final date (`Stop_MJD`). Furthermore, we decompose each period in single days (specifying the starting date and the final date both in UTC and in MJD) and produce a

[2]That is the order of magnitude of the shift due to the gravitational potential difference between a clock on ground and a clock at the altitude of the Galileo FOC satellites under consideration.

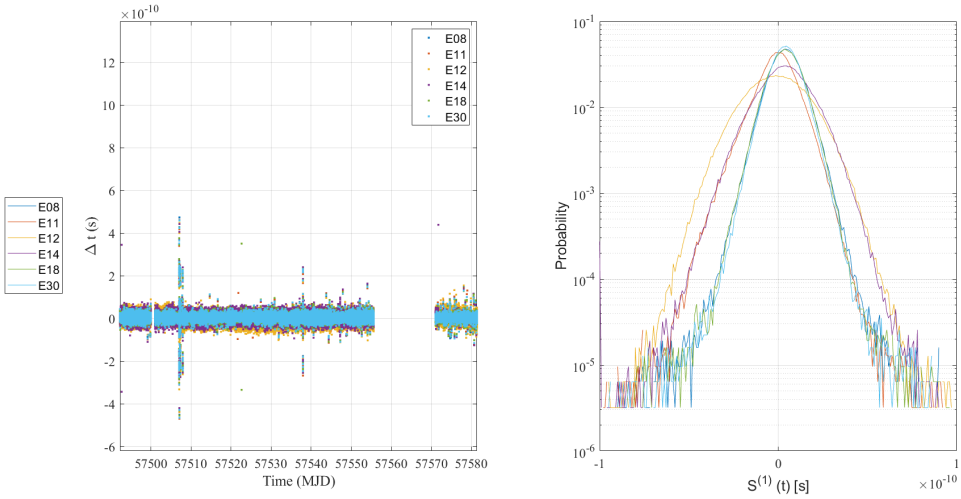

Figure 6.7. *On the left, the time behaviour of the clock-bias data processed according to the procedure described in §6.5.3.1. On the right, the amplitude distribution of the clock-bias pseudoderivative of the six satellites considered.*

Start_day	Stop_day	Start_MJD	Stop_MJD
16-Mar-2016 04:02:00	16-Mar-2016 23:59:59	57463.17	57463.99
17-Mar-2016 00:00:00	17-Mar-2016 23:59:59	57464	57464.99
18-Mar-2016 00:00:00	18-Mar-2016 23:59:59	57465	57465.99
19-Mar-2016 00:00:00	19-Mar-2016 23:59:59	57466	57466.99
...	...	...	...
11-Apr-2016 00:00:00	11-Apr-2016 19:11:30	57489	57489.80

Table 6.1. *Example of one of the common clock operating periods. The subdivisions in MJD are made according to the working time of the reference clock.*

corresponding file of the form shown in Tab.6.1. This operation is required to be compliant with the daily functioning of the reference clock.

It is important to stress that the ground reference clock is not always the same but typically changes every day. In particular, it could be a specific clock or the combination of multiple station clocks. In light of this, it is necessary to establish for each day of the identified common period, which is the reference clock that is working and stored its relevant characteristics (position and operating time).

6.5.3.2 False alarm analysis

The estimation of the background noise is important in order to extract its statistical properties to get an insight about how many accidental events (above a certain threshold of the signal amplitude) occur in given periods.

In this context, we have to evaluate the frequency of no-physical trigger events. As previously explained, the trigger event is a multiple coincidence among negative delta-like events. Due to the sampling time of 30 s we search for multiple coincidences among events at the same sample.

A first evaluation of the false alarm as function of the threshold can be calculated starting from the probability that the chosen threshold is overcome by a single clock. In Fig.6.8 this probability, P_j, *i.e.* the ratio between the number of samples over the threshold and the total number of samples, is reported for the six considered clocks over a period of contemporary operations of 108 days (312710 sample) between the 16-Mar-2016 and 19-Jul-2016.

Using these probabilities P_j one can calculate the probability of n-fold coincidence P_n. For N clocks, it is given by:

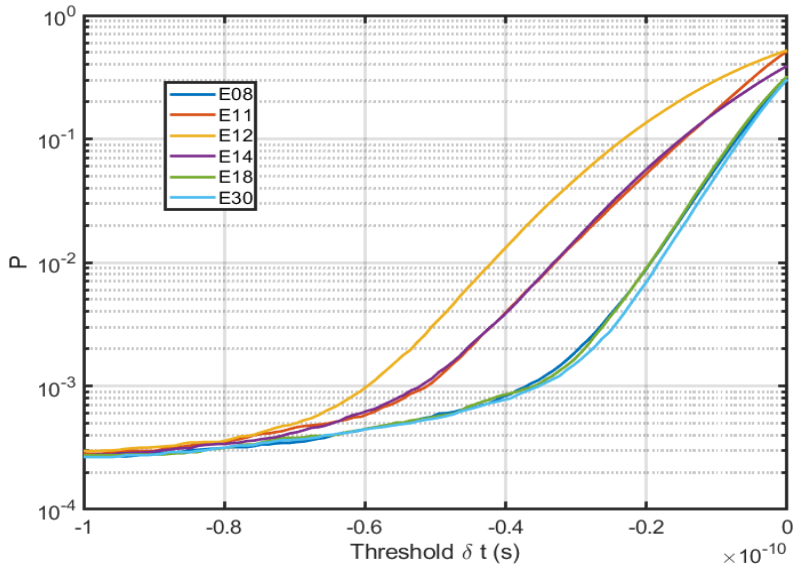

Figure 6.8. *Probability to have accidental coincidences in a single clock as function of the chosen amplitude threshold.*

$$P_n = \sum_{i=1}^{\binom{N}{n}} \prod_{jk} P_j(1-P_k)\,, \tag{6.48}$$

where the index j assumes the values of the n element of i-th combination $\binom{N}{n}$ and k of the remaining $n-N$ elements.

Using the previous formula on the chosen set of data we calculated the expected probability for n-fold coincidences. They are plotted in Fig.6.9 versus the threshold as continuous line.

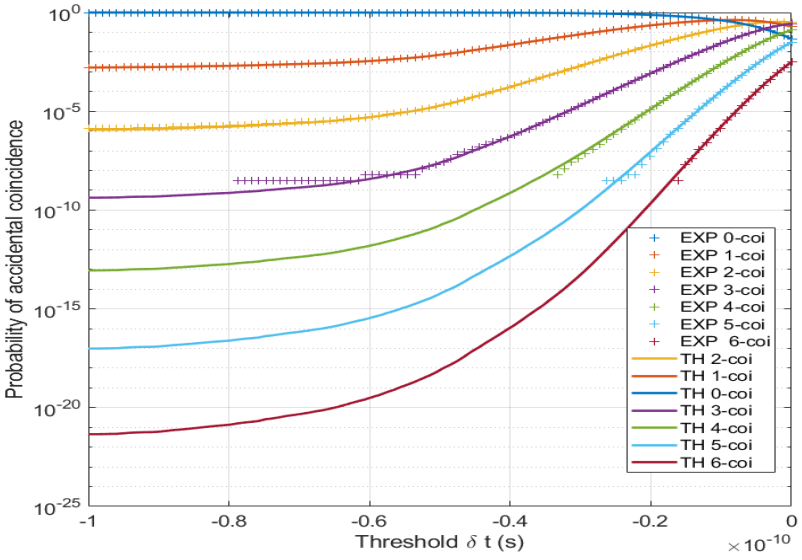

Figure 6.9. *Probability of n-fold coincidences as function of the chosen amplitude threshold. The theoretical simulation (in continuous line) is compared with the result obtained with the shift analysis (crosses).*

From both figure 6.8 and Fig.6.9, we deduce that if we move towards very large signals (in absolute value), we see that the probability of accidental coincidences is low. On the other hand,

if we look at small signals, the probability increases. This tells us that, due to the effect of the background noise, coincidences with large spikes are less likely than coincidences with smaller spikes.

To obtain these results, a random time shift is applied on the pseudo-derivative sequences of the six satellites' clocks. This operation is repeated M time obtaining M independent sequences for the $N = 6$ clocks. These sequences are not physical due to the introduced time shifts, but they have the same statistical properties of the original set of data. We applied 1000×6 shift on the select set of data obtaining the result plotted as crosses in Fig.6.9. As we can see from this figure, the results obtained with the time shifts are totally compatible with the theoretical results.

6.5.3.3 The Matlab DW simulation code

For our purposes, we need to simulate the physics we want to study, *i.e.* the DW Dark Matter interactions with the Galileo FOC atomic clock, taking into account the orbital dynamics. This allows us to:

1. generate and study the DW propagation pattern as function of the DW model parameters (signal amplitudes, DW velocity, DW direction arrival).

2. generate a large number of events per day to add to the experimental background in order to build a robust statistical description of the detection efficiency as function of the amplitude and other characteristics of the signal. This information is crucial for the final measurements.

In the following we describe the details of the simulation developed with `Matlab`, as well as the two aspects mentioned above.

To start the simulation, four different types of data are required as input:

- ESA Galileo Metadata: orbital/Keplerian parameters and their rates in the ECI (Earth Centred Inertial) reference system,

- ground reference clocks data: positions and operating time periods,

- atomic clock data for the six selected satellites. In particular, we consider clock-bias time-series referred to the common working periods of the six satellites,

- files of the common working periods (as described in §6.5.3.1).

The `Matlab` code imports the input data and the user selects the physical parameters of the DW along with the number of simulated DW crossings for each day.

For each of these DW simulations, the dynamics of the satellites, as well as the one of the reference clock, is reconstructed thanks to their corresponding metadata. In particular, the evolution of the orbital parameters[3] over the simulation period is computed in the ECI reference system according to the prescription[4] reported in the ESA Galileo Metadata. Then, the ground reference clock operating on the day of the simulation is found and its evolution is calculated by transforming its position-coordinates from the terrestrial to the celestial reference system, *i.e.* from ECEF (Earth Centered Earth Fixed) to ECI reference system. The DW dynamics is generated as well. In particular, the DW is approximated as a plane wave approaching the satellites constellation. The simulated impact time of the DW with each satellite and with the current reference clock is recorded. The impact times are reported in a dedicated file similar to Tab.6.2.

It is possible to exploit a given run and the related list of impact times to show the trigger and the distribution of positive spikes on the pseudo-derivative time-series.

In order to suppress a hypothetical real signal and to provide a reliable simulated result, we performed a circular random shift of the time-series. We report a couple of examples for two

[3]Specifically, the right ascension of the ascending node and the mean anomaly in the case of the satellites in elliptical orbits otherwise also the evolution of the argument of pericenter is calculated.

[4]https://www.gsc-europa.eu/system-service-status/orbital-and-technical-parameters

N_sim	$E08$	$E11$	$E12$	$E14$	$E18$	$E30$	REF_CLK
1	t_E08_1	t_E11_1	t_E12_1	t_E14_1	t_E18_1	t_E30_1	t_REF1_1
2	t_E08_2	t_E11_2	t_E12_2	t_E14_2	t_E18_2	t_E30_2	t_REF1_2
3	t_E08_3	t_E11_3	t_E12_3	t_E14_3	t_E18_3	t_E30_3	t_REF1_3

Table 6.2. *Example table of the Matlab DW simulation code output file. The simulations are labelled within the file by means of progressive integers.*

different signal amplitudes in order to show the importance of the background noise: in Fig.6.10 we show a case in which the DW signal clearly emerges from the background noise while in Fig.6.11 the DW signal results to be hidden.

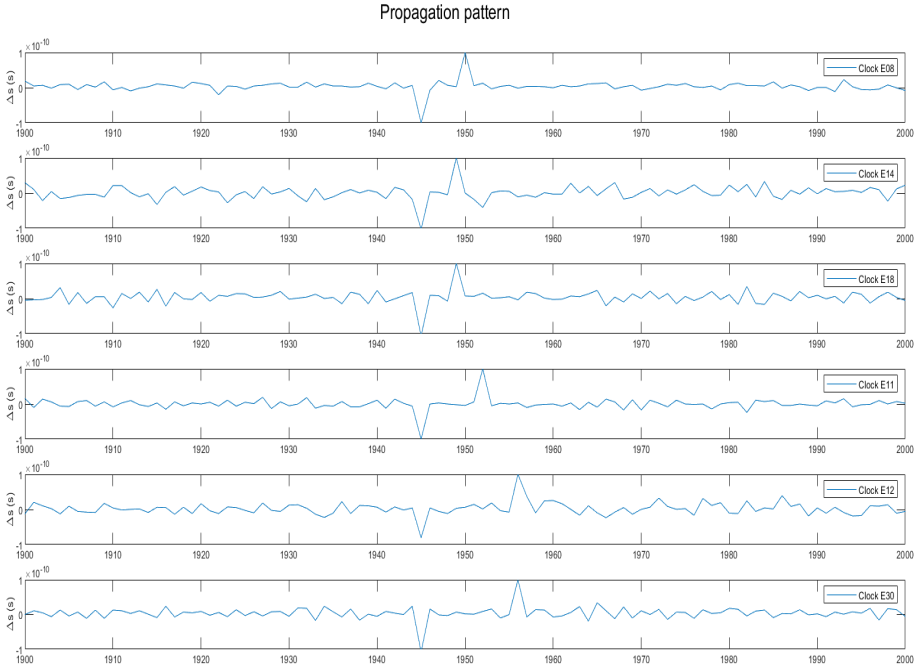

Figure 6.10. *Simulation of a DW signal (amplitude* $= 10^{-10}$ *s) in clock-data. The negative spike in coincidence with the six clock indicates the DW interaction with the reference clock. Positive spikes indicate the progressive interaction of DW with satellites clocks. The signal is clearly distinguishable from the background noise.*

The output file of the `Matlab` simulation allows not only to plot the impact of the DW on the pseudo-derivative time-series but also to perform a statistical description of the detection efficiency by using the simulated events added to the real background. We refer to the next section to address this aspect.

6.5.3.4 Events generations and the detection efficiency analysis

In the previous sections, it has been shown that the simulation code allows to generate an arbitrarily large number of DW events located at different times (along the considered common clock operating period) and with different kinematical properties of the DW *i.e.* velocity and incoming directions. In this context, we have created a first *ensamble* of ~ 500 events with $v_g = 270$ km/s and with random incoming direction. These events have been allocated in a proper database with the form previously discussed (see Tab.6.2). Each row represents an event and it is characterised by the impact times of the DW with the considered clocks and the impact time of the DW with the corresponding terrestrial clock operating in that day. The database can be used to perform a simple and preliminary statistical analysis: time-distance expected

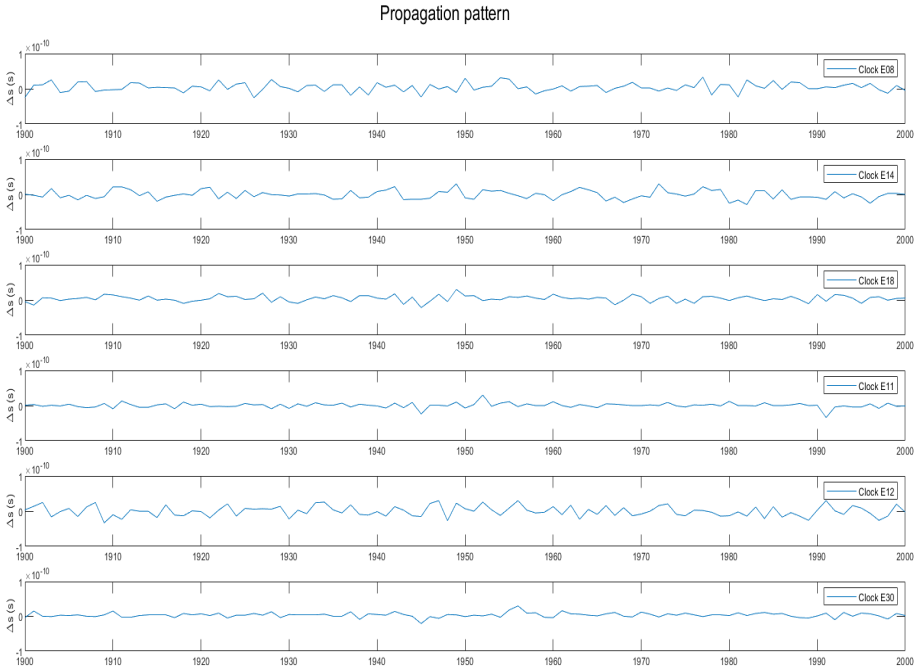

Figure 6.11. *Simulation of a DW signal (amplitude* $= 0.3 \times 10^{-10}$ *s) in clock-data. In this case we cannot distinguish the signal from the background noise.*

between a positive spike and its relative trigger. This preliminary analysis is necessary because the current the sampling time of the ESA-ESOC data is 30 s so, if the negative trigger and the positive spikes are within the same sample epoch, they should cancel each other. In Fig.6.12 we report the distribution of these time differences for each clock.

The plot tells us a couple of interesting results. For many of the simulated events the time distance between the on-board clock time impact and the station clock time impact is smaller than the standard sampling time. Therefore, it is likely to find both the signals in the simulated data. Second, this result should be sensible to the DW velocity: a fast-moving object could produce much more alignments considering the sampling time ~ 30 s. However, if one assumes that DW distribution can be described via the standard halo model (for DM), it is unlikely that the propagation velocity is much larger than the considered one. In order to explore such cases, it would be useful to consider small GNSS sampling time, for example $\tau \sim 1$ s.

The next fundamental step regards a preliminary detection efficiency analysis, *i.e.* the *statistical characterisation* of the network (capability) to exhibit possible and physical DW signals (trigger events) as function of a reasonable set of signal amplitude thresholds. The complementary false-alarm analysis (§6.5.3.2) provides an estimation of the threshold(s) that keep the occurrence of noise accidental coincidences to a very rare rate. In principle, different threshold values can be used for different n-fold coincidences scenarios. Once the required false alarm has been established (see Fig.6.9), the threshold can be lower for sixfold coincidences than for analyses based on fivefold or fourfold coincidences.

In order to perform the detection efficiency analysis, we have used the example database discussed in the previous section. In fact, the list of events can be used to produce a concrete set of table clock (bias pseudoderivative) time-series, once a physical-motivated spike amplitude is chosen. These tables are basically $n \times m$ matrix pattern, where n is the number of clocks and m is the number of sampling times. The extraction of the (column) trigger events from the generated pattern allows to construct a global record of the form shown in Tab.6.3.

For a preliminary analysis, a collection that span just over three orders of magnitude appears to be mathematically consistent, as shown in the following. The final step just consists in setting a threshold and looking for a given *clock coincidence* in each row. Then repeat the operation for the whole threshold spectra. Here, we define a clock coincidence by the number of clocks that (at

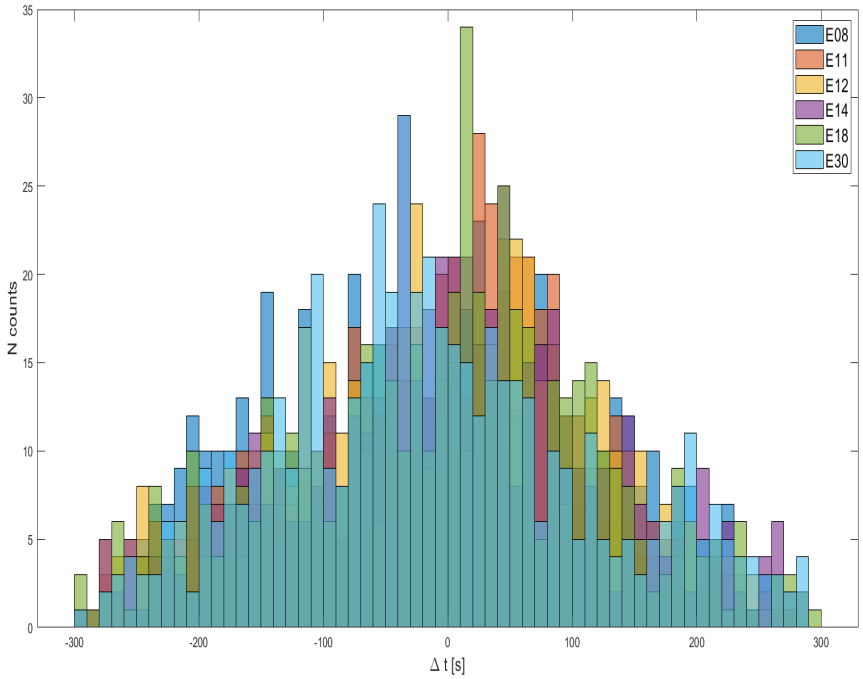

Figure 6.12. *The distribution of the time differences between clock and station time-impacts for the six satellites considered. The binning width is* 10 *s.*

Event_Trigger_time	*E*08	*E*11	*E*12	*E*14	*E*18	*E*30
t1	v_E08_1	v_E11_1	v_E12_1	v_E14_1	v_E18_1	v_E30_1
t2	v_E08_2	v_E11_2	v_E12_2	v_E14_2	v_E18_2	v_E30_2
t3	v_E08_3	v_E11_3	v_E12_3	v_E14_3	v_E18_3	v_E30_3

Table 6.3. *Example table of the clock-signal at the trigger epoch for the six satellites considered.*

the trigger time) experience a trigger value that exceeds the (current) threshold. For example, a sixfold coincidence requires that all the six clock values exceed the threshold while a fivefold coincidence requires that at least five clocks goes beyond the threshold. In our case, we consider a set of 10^3 thresholds spanning from $[-5 \times 10^{-13}$ to $-5 \times 10^{-10}]$ s, we also consider all possible clock coincidences of our case (twofold, threefold, fourfold, fivefold and sixfold) and suppose a DW that imprints a very large spike amplitude $\sim 10^{-8}$ s. The result of the corresponding detection efficiency analysis is reported in Fig.6.13.

The plot shows that the detection efficiency curves are characterised by an initial growth (upper panel), followed by an almost plateau region and a final growth (bottom panel). The initial increasing becomes effective around the injected DW amplitude. The plateau region is influenced by the fact that the positive and the negative spikes are not always resolved so they cancel each other. As a result, the pseudoderivative clock values at the trigger epoch tend to reduce to the background noise. The final growth is due to the background noise, that is able to generate casual or spurious clock coincidences.

The analysis was repeated for different group of coincidences. As one can expect, each of the n-coincidences curves has a specific efficiency of detection level (the height of the plateau). The sixfold scenario saturates at a probability of $\sim 50\%$, that means half of the time, at least one clock per event does not display the trigger spike. The fivefold scenario presents a much larger probability just above 80% while for the fourfold case one has a probability just below 90%. This piece of evidence clearly suggests that, in the case of not adequate sampling time, fivefold or fourfold combination guarantee a general, much larger efficiency.

We note that for such large signals considered, in the more favourable cases of fourfold, threefold and twofold coincidence analysis, the efficiency is maximum around 90%. The DW

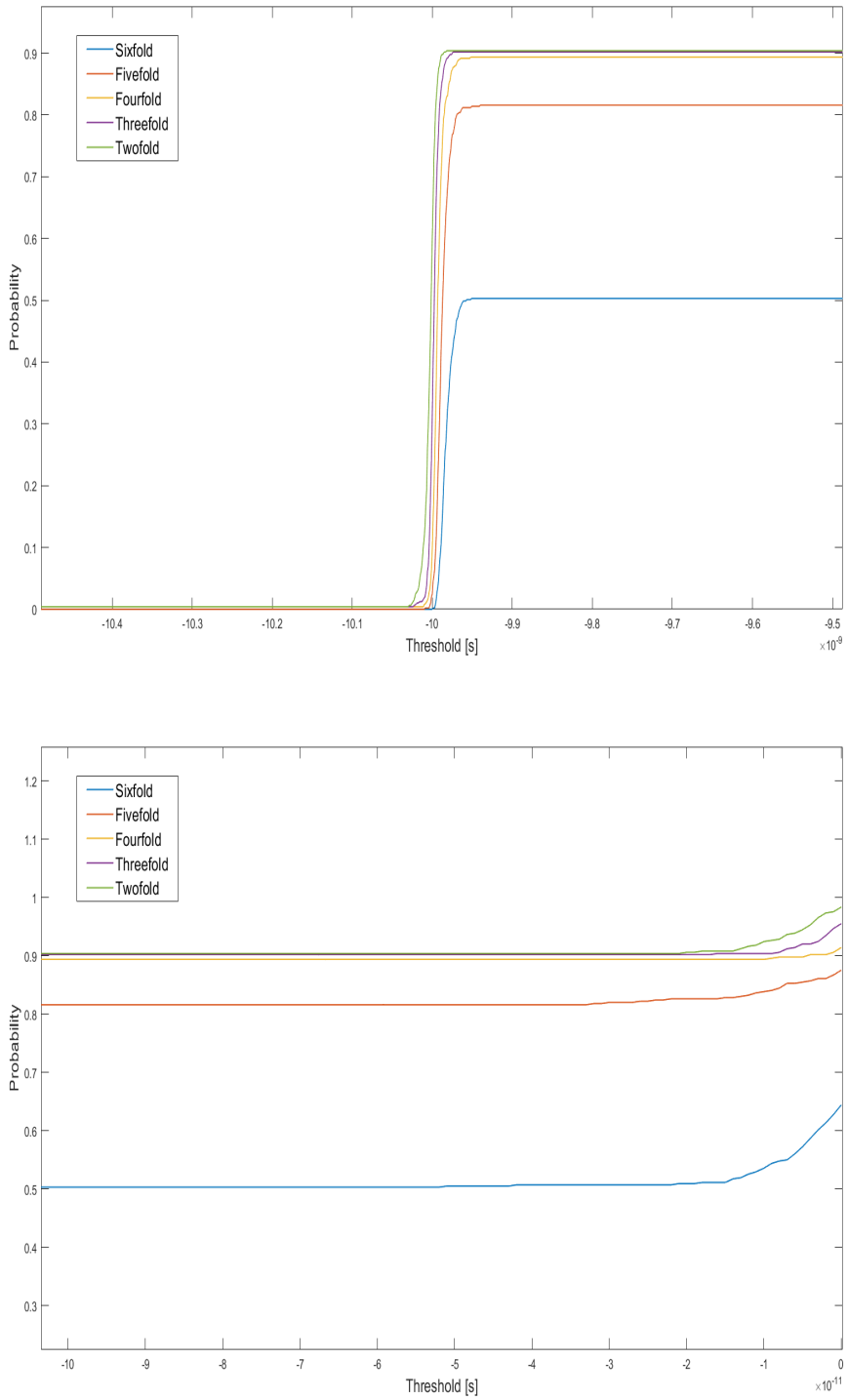

Figure 6.13. *Detection efficiency for a DW signal with an amplitude of* 10^{-8}.

are rare events and therefore a great effort must be made to reduce the sampling time to a shorter time, for example $\tau \sim 1$ s. This could have two advantages, the possibility to significantly increase the detection efficiency and also to observe the shape of the signals in the clocks. As the available data of ESA-ESOC do not have a reasonable sampling time for our purposes, our future activities are directed towards estimating the clock-bias with a shorter sampling time ($\tau \sim 1$ s) by exploiting the potential of the `Bernese` software.

Chapter 7

Conclusions

In this Thesis, we have presented the Galileo for Science project (G4S_2.0) and the ongoing activities related to the Fundamental Physics measurements. As we have seen, the project has a wide range of objectives, from measuring relativistic precessions and gravitational redshift to constraining galactic Dark Matter using the European Space Agency's Galileo FOC constellation.

In Chap.2 we have given an overview on the Galileo infrastructure (§2.1) and the Galileo FOC constellation (§2.2.1). In particular, the orbits of the satellites and the complex structure of a Galileo FOC spacecraft were explained, highlighting the lack, in the ESA documentation, of a complete and detailed data on its physical characteristics (§2.2.2). The constellation is currently characterised by 24 satellites, two of them accidentally placed in elliptical orbits, GSAT0201 and GSAT0202. The orbits and the atomic clock data of these two satellites will be exploited to measure the gravitational redshift and the relativistic precessions. The clock-data of the entire Galileo FOC constellation will be instead used to place bounds on the local Dark Matter (DM), in form of Domain Walls (DWs).

The measurements of the gravitational redshift and of the relativistic precessions are strictly dependent on the satellites dynamics and on the precise determination of their orbits. As explained in Chap.1, §3.1, there are several perturbations that influence the satellite's motion both of gravitational and non-gravitational origin (a detailed description of these perturbations has been given in Chap.3, §3.3. Improving the modelling of the orbital effects due to the direct solar radiation pressure, the largest non-gravitational perturbation, will significantly improve the accuracy of the precise orbit determination and, as a consequence, the accuracy of these measurements. Particularly, the improvement of the dynamical model would allow to properly model also the subtle effects of the non-conservative forces over long-periods enabling to extract the signature of the relativistic effects of the secular type (relativistic precessions) from the orbital residuals.

Indeed, the activities concerned, on the one hand, the development of new models to take into account the non-gravitational forces acting on the Galileo FOC satellites and, on the other, the determination of the orbits of the satellites by means of a least-squares fit of the laser-ranged data (of each spacecraft) provided by the ILRS.

In terms of models, in Chap.3, §3.4 we have evaluated the state of the art of the main models developed in the literature regarding the effects produced by the direct solar radiation pressure and by other (much smaller) non-conservative forces acting on the Galileo FOC satellites and, in general, on the GNSS satellites. This is useful for presenting the types and peculiarities of the different models, highlighting their advantages and disadvantages. We are interested in developing a model for the satellite as close as possible to a Finite Element Model (FEM). Although the FEM has been developed by several authors in the literature, it does not seem to be used by the various GNSS analysis centres. There are two reasons for this: firstly, there are difficulties in incorporating the satellite FEM into POD processes, with subsequent application of Ray-Tracing techniques to it, and secondly, there is a real lack of accurate knowledge of the satellite structure, starting with its optical properties and how they evolve over time.

As a precursor to the FEM of the satellite, we have implemented a Box-Wing model based on the metadata provided by ESA (Chap.3, §3.5) that we call Simplified Box-Wing (S-BW). The model has been applied to take into account the perturbation produced by direct solar radiation pressure. The model differs in part from those reported in the literature of GNSS

satellites in not modelling the visible solar radiation absorbed by the various surfaces making up the satellite, in terms of its instantaneous re-emission. This effect will in fact be treated more properly under the perturbations linked to the effects of thermal thrust. Moreover, in contrast to the models reported in the literature, the complete law of the complex attitude of the satellite was implemented on the basis of the information provided by ESA in its twofold form: "nominal" and "modified" (Chap.2, §2.5). This law was designed for satellites in nominal orbit or almost circular orbit but it is applied in the same way to satellites in elliptical orbits. We have highlighted some differences that arise in applying the attitude law to both cases, on GSAT0208 and on GSAT0201, respectively.

The S-BW model was used to calculate the accelerations produced by solar radiation on the various surfaces of the satellites. The accelerations have been provided in the Sun-Satellite-Earth and in the Gauss reference frames (Chap.3, §3.5.1). Subsequently, the accelerations in the Gauss reference system were exploited to determine, for the first time, the corresponding effects on the Keplerian elements by means of the so-called Gauss perturbation equations (Chap.3, §3.5.2). All these results have been obtained for the two Galileo FOC in elliptical orbit and will be relevant for the relativistic precessions measurements.

As regards the determination of the orbits of the satellites, a series of preliminary PODs were performed with the `GEODYN II` software (Chap.4, §4.1.1.1) using the SLR data of the GSAT0201 and GSAT0208 satellites (Chap.4, §4.2). In this context, for various reasons explained in §4.2, a crude model was intentionally chosen for the satellites: a cannonball with an area to mass ratio equal to the average one of the Galileo FOC satellites. From the results of the POD, it is clear that the scientific community does not always have a sufficient number of normal points, especially for satellites in elliptical orbits. In this context, we have officially asked the ILRS Central Bureau for an observation campaign dedicated to the G4S_2.0 project, as was done in the recent past for the GREAT and GASTON projects. The SLR campaign was approved and started on 20th January 2024.

As a check, we compared the orbits obtained with `GEODYN II`, again for the GSAT0201 and GSAT0208 satellites, with those that can be obtained from the precise orbits determined by the IGS analysis centres (Chap.4, §4.2). In particular, the orbits obtained by ESOC during the two years of the GREAT project were taken into consideration. The verification was positive: it has been shown that even a cannonball model is sufficient to reproduce the correct long-term behaviour of the orbits. We then proceeded to compute the orbital residuals from the orbits obtained in the case of GSAT0201.

From the analysis of reliable orbital residuals, it is possible to extract the signature of the relativistic effects we are interested in, such as the relativistic precessions predicted by General Relativity (Chap.4, §4.2.1). The residuals we obtained clearly show the limitations of the dynamical model used, in particular the presence of long-term effects with a periodicity of about 365 days, therefore attributable to an inadequate modelling of the direct solar radiation pressure. In order to verify this conclusion, we have directly compared the residuals in the orbital elements with the predictions of our S-BW model on the same elements. Indeed, the S-BW represents for us a first basic model in order to construct better performing models, until we hopefully reach the FEM of the spacecraft. The comparison was not only positive, but remarkable, as almost all observed and unmodelled effects are reproduced by the S-BW model. These results are important because they enable us to give the accelerations obtained from our S-BW model as an input to `GEODYN II`, as well as those we will obtain in the future, from the spacecraft models we are gradually building. This will lead to a significant improvement in the reduction of the tracking data in the POD, as the satellite dynamic is better characterised. In this respect, a POD with our S-BW has been performed obtaining a relevant reduction of the orbital residuals (Chap.4, §4.2.1).

All the satellites are equipped with atomic clocks whose signal and characteristics are explained in detail in Chap.5. In particular, the time-series of the clock-bias, *i.e.* the difference between the time measured by the onboard clocks and the time measured by a ground reference clock, are the data we use for Dark Matter (DM) constraints analysis as well as for the gravitational redshift. Currently, we mainly worked on DM constraints since for the gravitational redshift we have not yet obtained the information on the so-called relativistic correction applied to the clock-data which is necessary for the measurement.

The cosmological context, with the various current scenarios for DM, has been discussed in

Chap.6, §6.1. In G4S_2.0, we want to constrain the galactic DM density due to Domain Walls. These objects are stable and localised solutions of ultra-light scalar fields eventually produced in the early Universe (Chap.6, §6.2). Domain Walls could cross Earth's orbit and interact with Galileo onboard atomic-clocks. Assuming a quadratic scalar interaction between DM and clock atoms, we assist to a transient relative variation in the fundamental constants (Chap.6, §6.3). This leads to a delta-like transient shift in the atomic clock frequency that can be visualised in the pseudo-derivative of the clock-bias (Chap.6, §6.5). Such signal depends both on the nature of the clock and the characteristic of the ultralight scalar comprising the DW. In Chap.6, §6.5.3 we explain our strategy which differs from what has already been done in literature in the following aspects: i) the characterisation of the background noise to evaluate the false-alarm, *i.e.* the non-physical signal; ii) the evaluation of the detection efficiency with a `Matlab` simulation code to study how many DW events of a certain amplitude, we expect to detect for a set of amplitude-thresholds; iii) the future apriori choice of the parameters of the time-coincidences analysis in order to identify the DW pattern in the clock-data.

We have currently built a realistic simulation code (Chap.6, §6.5.3.3) which, to our knowledge, has not yet been developed in the literature. It takes into account: i) all the features of the satellites orbits and their dynamic, distinguishing between elliptical and nominal orbits, ii) the fact that the ground reference clock changes every day and iii) the fact that not all the onboard atomic clocks work simultaneously. The detection efficiency analysis (Chap.6, §6.5.3.4) has shown that also for very large signal, the signal detection results to be limited, mainly due to the current standard sampling time, $\tau \sim 30$ s. The introduction of a small τ, *e.g.* $\tau \sim 1$ s should naturally provides stronger and more reliable conclusions.

However, some aspects should be highlighted. In our analysis so far, we have considered the simple case where the scalar field inside the DW interacts only with the electron. If we assumed further couplings with other components of the Standard Model (Chap.6, §6.3), we would have to consider different types of clocks. Indeed, we know that the Galileo satellites are equipped with a couple of Passive Hydrogen Maser (PHM) and a couple of Rubidium clocks (RAFS). Therefore, it should be desirable to divide the whole clock network into two subnetworks: a PHM subnetwork and a RAFS subnetwork. This would provide the chance to: i) derive the statistical properties of the background noise for a specific subnetwork; ii) perform more suitable simulations by focusing on a specific type of clock; iii) put constraints on Domain Wall DM exploiting two different atomic-detectors with a different response to a DW perturbation. In this direction, and in agreement with the ASI-CGS, we are planning to contact the Galileo Control Centre (GCC-I) located in Fucino Space Centre in order to acquire the necessary information about the onboard clocks. Moreover, as previously anticipated, the ground reference clock is not always the same but typically changes every day. Therefore, it would be desirable to have clock-data referred to a single ground clock for a long time. This would allow for a homogenous dataset and a simplification of the simulations.

Appendix A

Perturbing Equations

A.1 Gauss equations

In the following the Gauss equations for the osculating ellipse are shown [48]:

$$\frac{da}{dt} = \frac{2}{n\sqrt{1-e^2}}[T + e(T\cos f + R\sin f)]\,, \tag{A.1}$$

$$\frac{de}{dt} = \frac{\sqrt{1-e^2}}{na}[R\sin f + T(\cos f + \cos E)]\,, \tag{A.2}$$

$$\frac{dI}{dt} = \frac{W}{H}r\cos(\omega + f)\,, \tag{A.3}$$

$$\frac{d\Omega}{dt} = \frac{W}{H\sin I}r\sin(\omega + f)\,, \tag{A.4}$$

$$\frac{d\omega}{dt} = \frac{\sqrt{1-e^2}}{nae}\left[-R\cos f + T(\sin f + \frac{1}{\sqrt{1-e^2}}\sin E)\right] - \frac{d\Omega}{dt}\cos I\,. \tag{A.5}$$

where H represents the orbital angular momentum per reduced mass of the two body problem, while R, T and W are the components of the acceleration in the Gauss reference frame along the radial, transversal and out of plane directions, respectively. In these equations the quantities a, e, I, Ω and ω are, respectively, the satellite's semimajor axis, eccentricity, inclination, longitude of the ascending node and argument of perigee. The fast angular variables f and E are the satellite's true anomaly and eccentric anomaly, finally n represents the satellite mean motion. The essence of the method is to write the time derivatives of the parameters characterising the perturbed satellite orbit and to integrate them numerically in order to find the effects in the elements.

Concerning the Gauss equation for a fast variable, such as the mean anomaly M, we have to consider two perturbing equations in general. If $M(t) = \eta + \rho$ represents the osculating mean anomaly at time t with $\dot{\rho} = n$ we finally obtain:

$$\begin{aligned}\frac{d\eta}{dt} = {} & R\left[\frac{\cos E}{nae(1-e^2)} - \frac{\sqrt{1-e^2}\sin f\sin E}{na} + \frac{2r}{na^2}\right] + \\ & + T\left[\frac{\sqrt{1-e^2}\sin E}{nae}\left(\frac{a}{r} - 1\right) + \frac{\sqrt{1-e^2}}{na}\sin E(\cos f + \cos E)\right]\end{aligned} \tag{A.6}$$

and

$$\frac{d^2\rho}{dt^2} = \dot{n} = -\frac{3}{a\sqrt{1-e^2}}[T + e(T\cos f + R\sin f)]\,. \tag{A.7}$$

This approach, as explained in [48], has the advantage of introducing an element that changes "slowly", *i.e.* with a time derivative that goes to zero with the perturbing acceleration.

A.2 Lagrange equations

In the following, the Lagrange perturbation equations are given [61]:

$$\frac{da}{dt} = \frac{2}{na}\frac{\partial \mathcal{R}}{\partial M}\,, \tag{A.8}$$

$$\frac{de}{dt} = \frac{1-e^2}{na^2 e}\frac{\partial \mathcal{R}}{\partial M} - \frac{\sqrt{1-e^2}}{na^2 e}\frac{\partial \mathcal{R}}{\partial \omega}\,, \tag{A.9}$$

$$\frac{dI}{dt} = \frac{1}{na^2\sqrt{1-e^2}\sin I}\left(\cos I\frac{\partial \mathcal{R}}{\partial \omega} - \frac{\partial \mathcal{R}}{\partial \Omega}\right)\,, \tag{A.10}$$

$$\frac{d\Omega}{dt} = \frac{1}{na^2\sqrt{1-e^2}\sin I}\frac{\partial \mathcal{R}}{\partial I}\,, \tag{A.11}$$

$$\frac{d\omega}{dt} = \frac{\cos I}{na^2\sqrt{1-e^2}\sin I}\frac{\partial \mathcal{R}}{\partial I} + \frac{\sqrt{1-e^2}}{na^2 e}\frac{\partial \mathcal{R}}{\partial e}\,, \tag{A.12}$$

$$\frac{dM}{dt} = n - \frac{1-e^2}{na^2 e}\frac{\partial \mathcal{R}}{\partial e} - \frac{2}{na}\frac{\partial \mathcal{R}}{\partial a}\,, \tag{A.13}$$

where a, e, I, Ω and ω are the Keplerian elements and n is the mean motion, already introduced in the previous section. M is the mean anomaly and $\mathcal{R}$ is the perturbing function.

List of Figures

List of Tables

Bibliography

[1] A. Einstein, *Die Grundlage der allgemeinen Relativitätstheorie*, Annalen der Physik 354, 769 (1916).

[2] L. I. Schiff, *On Experimental Tests of the General Theory of Relativity*, Am. J. Phys. 28, 340–343 (1960).

[3] C. M. Will, *Theory and Experiment in Gravitational Physics*, Cambridge University Press (1993).

[4] C. M. Will, *The Confrontation between General Relativity and Experiment.*, Living Rev. Relativ. 17, 4 (2014).

[5] B.P. Abbott et al. (LIGO Scientific Collaboration and Virgo Collaboration), *Observation of Gravitational Waves from a Binary Black Hole Merger*, Phys. Rev. Lett. 116, 061102 (2016).

[6] The Event Horizon Telescope Collaboration et al., *First M87 Event Horizon Telescope Results. IV. Imaging the Central Supermassive Black Hole* ApJL 875, L4 (2019).

[7] Event Horizon Telescope Collaboration et al., *First Sagittarius A* Event Horizon Telescope Results. I. The Shadow of the Supermassive Black Hole in the Center of the Milky Way.*, ApJL 930, L12 (2022)

[8] S. Capozziello & M. De Laurentis, *Extended Theories of Gravity*, Phys. Rept. 509, 167 (2011).

[9] T. Clifton, P. G. Ferreira, A. Padilla, and C. Skordis, *Modified gravity and cosmology*, Phys. Rept. 513, 1 (2012).

[10] M. Crosta, M. Giammaria, M. G. Lattanzi, and E. Poggio, *On testing CDM and geometry-driven Milky Way rotation curve models with Gaia DR2*, Mon. Not. Roy. Astron. Soc. 496, 2107 (2020).

[11] A. Einstein, *Uber das Relativit¨atsprinzip und die aus semselben gezogenen Forlerungen*, Jahr. d. Rad. u. Elek. 4, 411–462, (1907). Translated in The Collected Works of Albert Einstein 2, 252 - 311: Princeton, 1989.

[12] R. V. Pound & G. A. Rebka, *Gravitational Red-Shift in Nuclear Resonance*, Phys. Rev. Lett. 3, 439 (1959).

[13] R. V. Pound & J. L. Snider, *Effect of Gravity on Nuclear Resonance*, Phys. Rev., 140, B788 (1965).

[14] R. F. C. Vessot & M. W. Levine, *A Test of the Equivalence Principle Using a Space-Borne Clock*, Gen. Rel. Grav 10, 181 (1979).

[15] R. F. C. Vessot et al., *Test of Relativistic Gravitation with a Space-Borne Hydrogen Maser*, Phys. Rev. Lett. 45, 2081 (1980).

[16] F. Sapio, D. M. Lucchesi, M. Visco, S. Benedetti, E. Fiorenza, C. Lefevre, M. Lucente, C. Magnafico, R. Peron and F. Santoli, *The Galileo for Science (G4S_2.0) project: Fundamental Physics experiments with Galileo satellites DORESA and MILENA*, Nuovo Cimento C 45, 152 (2022).

[17] A. Di Marco, F. Sapio, M. Cinelli, E. Fiorenza, C. Lefevre, P. Loffredo, D. M. Lucchesi, M. Lucente, C. Magnafico, R. Peron, F. Santoli, M. Visco, *The Galileo for Science (G4S 2.0) project: Measurement of the Gravitational Redshift with the Galileo satellites DORESA and MILENA*, Nuovo Cimento 46 C, 116 (2023).

[18] S. Herrmann, F. Finke, M. Lülf, O. Kichakova, D. Puetzfeld, D. Knickmann, M. List, B. Rievers, G. Giorgi, C. Günther, H. Dittus, R. Prieto-Cerdeira, F. Dilssner, F. Gonzalez, E. Schönemann, J. Ventura-Traveset, and C. Lämmerzahl, *Test of the gravitational redshift with Galileo satellites in an eccentric orbit*, Phys. Rev. Lett. 121, 231102 (2018).

[19] P. Delva, N. Puchades, E. Schönemann, F. Dilssner, C. Courde, S. Bertone, F. Gonzalez, A. Hees, C. Le Poncin-Lafitte, F. Meynadier, R. Prieto-Cerdeira, B. Sohet, J. Ventura-Traveset, and P.Wolf, *Gravitational redshift test using eccentric galileo satellites*, Phys. Rev. Lett. 121, 231101 (2018).

[20] F. Vespe, D. Lucchesi, A. Tartaglia, G. Delle Monache, R. Peron, E. Rosciano, F. Santoli, and M. Visco, *GALILEO for Science project (G4S): An Opportunity to Perform New Measurements in Fundamental Physics.*, in Scientific and Fundamental Aspects of GNSS in Galileo, 6th International Colloquium, Valencia (Spain) (2017).

[21] A. Derevianko & M. Pospelov, *Hunting for topological dark matter with atomic clocks*, Nature Phys. 10, 933, (2014).

[22] B.M. Roberts, G. Blewitt, C. Dailey et al. *Search for domain wall dark matter with atomic clocks on board global positioning system satellites.* Nat Commun 8, 1195 (2017).

[23] T. Springer, *NAPEOS mathematical models, and algorithms*, Tech. Rep. No. DOPS-SYS-TN-OlOO-OPSGN, European Space Operations Center (ESA/ESOC), (2009).

[24] R. Dach, S. Lutz, P. Walser, P. Fridez, *Bernese GNSS Software User Manual 5.2*, University of Bern, (2015).

[25] D. M. Lucchesi & R. Peron, *Accurate Measurement in the Field of the Earth of the General-Relativistic Precession of the LAGEOS II Pericenter and New Constraints on Non-Newtonian Gravity*, Phys. Rev. Lett. 105, 231103 (2010).

[26] D. M. Lucchesi & R. Peron, *LAGEOS II pericenter general relativistic precession (1993-2005): Error budget and constraints in gravitational physics*, Phys. Rev. D 89, 082002 (2014).

[27] I. Ciufolini, A. Paolozzi, E. C. Pavlis et al., *An improved test of the general relativistic effect of frame-dragging using the LARES and LAGEOS satellites*, Eur. Phys. J. C 79, 872 (2019).

[28] D. Lucchesi, M. Visco, R. Peron, M. Bassan, G. Pucacco, C. Pardini, L. Anselmo, and C. Magnafico, *A 1% Measurement of the Gravitomagnetic Field of the Earth with Laser-Tracked Satellites*, Universe 6, 139 (2020).

[29] D. E. Pavlis et al., *GEODYN II Operations Manual*, NASA GSFC (1998).

[30] D. Lucchesi, M. Visco, C. Lefevre, M. Lucente, F. Santoli, F. Sapio, M. Cinelli, A. Di Marco, E. Fiorenza, P. Loffredo, C. Magnafico, R. Peron and F. Vespe, *Fundamental Physics measurements with Galileo FOC satellites and the Galileo for Science project. Part I: a 3D-CAD and a Box Wing for modeling the effects of Non-Conservative Forces*, Phys. Rev. D., 109, 062004 (2024).

[31] F. Sapio, D. Lucchesi, M. Visco, R. Peron, M. Lucente, C. Lefevre, M. Cinelli, A. Di Marco, E. Fiorenza, P. Loffredo, C. Magnafico, F. Santoli and F. Vespe: *Fundamental Physics measurements with Galileo FOC satellites and the Galileo for Science project. Part II: a Box Wing for modeling Direct Solar Radiation Pressure and preliminaries Orbit Determinations*, Phys. Rev. D., 109, 062005 (2024).

[32] J. Sanz Subirana, J. M. Juan Zornoza and M. Hernández-Pajares, *GNSS Data Processing, Vol. 1: Fundamentals and Algorithms* Production Editor: K.Fletcher, Publisher: ESA Communications.

[33] O. Montenbruck and E. Gill, *Satellite Orbits - models, methods and application* (Springer, Berlin, 2005).

[34] J. J. Degnan, *Satellite Laser Ranging: Status and Future Prospects*, IEEE Trans. Geosci. and Rem. Sens., Vol. GE-23, pp. 398-413, 1985.

[35] M. R. Pearlman, J.J. Degnan and J. M. Bosworth, Adv. Space Res. 30 135–43 (2002)

[36] D.M. Lucchesi, L. Anselmo, M. Bassan, C. Pardini, R. Peron, G. Pucacco and M. Visco *Testing the gravitational interaction in the field of the Earth via satellite laser ranging and the Laser Ranged Satellites Experiment (LARASE)* Class. Quantum Grav. 32 155012, (2015)

[37] L. Carlin, A. Hauschild & O. Montenbruck, *Precise point positioning with GPS and Galileo broadcast ephemerides.* GPS Solut 25, 77 (2021).

[38] P. Teunissen and O. Montenbruck, *Springer Handbook of Global Navigation Satellite Systems* (2017).

[39] Y. Bar-Sever and E. Yoaz, *A new model for GPS yaw attitude*, Journal of Geodesy (1996).

[40] F. Riedel and O. Gulmus, *Observations and Operational Aspects on the Galileo Attitude and Orbit Control Subsystem - Infra-Red Radiance Variations* (2014) p. 3546.

[41] O. Montenbruck, R. Schmid, F. Mercier, P. Steigenberger, C. Noll, R. Fatkulin, S. Kogure, and A. Ganeshan, *Gnss satellite geometry and attitude models*, Advances in Space Research 56, 1015 (2015).

[42] G. Beutler, E. Brockmann, W. Gurtner, U. Hugentobler, L. Mervart, M. Rothacher, and A. Verdun, *Extended orbit modeling techniques at the CODE processing center of the international GPS service for geodynamics (IGS): theory and initial results.*, Manuscr. Geod. 19, 367 (1994).

[43] C. Rodriguez-Solano, U. Hugentobler, and P. Steigenberger, *Adjustable box-wing model for solar radiation pressure impacting gps satellites*, Advances in Space Research 49, 1113 (2012).

[44] D. Arnold, M. Meindl, G. Beutler, R. Dach, S. Schaer, S. Lutz, L. Prange, K. Sośnica, L. Mervart, and A. Jäggi, *CODE's new solar radiation pressure model for GNSS orbit determination.*, Journal of Geodesy 89, 775 (2015).

[45] O. Montenbruck, P. Steigenberger, and U. Hugentobler, *Enhanced solar radiation pressure modeling for Galileo satellites.*, Journal of Geodesy 89, 283 (2015).

[46] G. Bury, K. Sośnica, R. Zajdel, and D. Strugarek, Toward the 1-cm Galileo orbits: challenges in modeling of perturbing forces, Journal of Geodesy 94, 16 (2020).

[47] W. M. Kaula, *Theory of Satellite Geodesy* Blaisdell Publ. Co., Waltham (1966).

[48] A. Milani, A. M. Nobili and P. Farinella, *Non-gravitational perturbations and satellite geodesy* Adam Hilger, Bristol (1987).

[49] B. D. Tapley, F. Flechtner, S. V. Bettadpur, and M. M. Watkins, *The status and future prospect for GRACE after the first decade*, Eos Trans. Fall Meet. Suppl. Abstract G32A-01 (2013).

[50] F. W. Landerer et al., *Extending the Global Mass Change Data Record: GRACE Follow-On Instrument and Science Data Performance*, Geophysical Research Letter, 47, e88306, (2020).

[51] D. P. Rubincam, *Postglacial rebound observed by Lageos and the effective viscosity of the lower mantle*, J. Geophys. Res., 89, 1077.

[52] M. K. Cheng, C. K. Shum, B. D. Tapley, *Determination of long-term changes in the Earth's gravity field from satellite laser ranging observations*, J. Geophys. Res., 102, 22377, (1997).

[53] C. M. Cox & B. F. Chao, *Detection of a Large-Scale Mass Redistribution in the Terrestrial System Since 1998*, Science 297, 831 (2002).

[54] M. Cheng, B. D. Tapley, and J. C. Ries, *Deceleration in the Earth's oblateness*, Journal of Geophysical Research: Solid Earth 118, 740 (2013).

[55] M. Cheng & J. C. Ries, *Decadal variation in Earth's oblateness (J_2) from satellite laser ranging data*, Geophysical Journal International 212, 1218 (2018).

[56] D. Lucchesi, L. Anselmo, M. Bassan, M. Lucente, C. Magnafico, C. Pardini, R. Peron, G. Pucacco and M. Visco, *Testing Gravitational Theories in the Field of the Earth with the SaToR-G Experiment*, Universe 7, 192 (2021).

[57] P. Melchior, *The Tides of the Planet Earth*. Pergamon Press, New York (1981).

[58] J. M. Wahr, *Ocean tides, part I: Global ocean tidal equations.*, Geophys. J. R. Astron. Soc., 64, 651 (1981).

[59] J. M. Wahr, *Ocean tides, part II: A hydrodynamical interpolation model.*, Geophys. J. R. Astron. Soc. 64, 677 (1981).

[60] B. V., Sanchez, *Rotational Dynamics of Mathematical Models of the Nonrigid Earth*, AMRL 1066, (1974).

[61] G. Pucacco & D. M. Lucchesi, *Tidal effects on the LAGEOS–LARES satellites and the LARASE program.* Celest Mech Dyn Astr 130, 66 (2018).

[62] W. M. Kaula, *Analysis of gravitational and geometric aspects of geodetic utilisation of satellites.*, Geophys. J. 5, 104 (1961).

[63] W. M. Kaula, *Tidal dissipation by solid friction and the resulting orbital evolution.*, Rev. Geophys. 2, 661 (1964).

[64] F. Roosbeek, *RATGP95: a harmonic development of the tide-generating potential using an analytical method.*, Geophys. J. Int. 126, 197 (1996).

[65] C. Huang, J. C. Ries, B. D. Tapley, and M. M. Watkins, *Relativistic effects for near-earth satellite orbit determination*, Celest. Mech. Dyn. Astron. 48, 167 (1990).

[66] I. Ciufolini & J. A. Wheeler, *Gravitation and inertia*, Princeton University Press (1995).

[67] J. Lense and H. Thirring, *Über den Einfluß der Eigenrotation der Zentralkörper auf die Bewegung der Planeten und Monde nach der Einsteinschen Gravitationstheorie*, Physikalische Zeitschrift 19 (1918).

[68] W. de Sitter, *On Einstein's theory of gravitation and its astronomical consequences.* Second paper, Mon. Not. R. Astron. Soc. 77, 155 (1916).

[69] D. P. Rubincam, *On the secular decrease in the semimajor axis of Lageos's orbit*, Celestial mechanics 26, 361 (1982).

[70] D. M. Lucchesi, *Reassessment of the error modelling of non-gravitational perturbations on LAGEOS II and their impact in the Lense-Thirring derivation-Part II*, Plan. Space Sci. 50, 1067 (2002), presented at OCA/CERGA Observatory, Grasse, France, December 18, 2001.

[71] D. P. Rubincam, P. Knocke, V. R. Taylor, and S. Blackwell, *Earth anisotropic reflection and the orbit of LAGEOS*, J. Geophys. Res. 92, 11662 (1987).

[72] D. M. Lucchesi, *LAGEOS Satellites Germanium Cube-Corner-Retroreflectors and the Asymmetric Reflectivity Effect*, Celestial Mechanics and Dynamical Astronomy 88, 269 (2004).

[73] D. Vokrouhlický and P. Farinella, *Thermal force effects on slowly rotating, spherical artificial satellites - II. Earth infrared heating*, Plan. Space Sci. 45, 419 (1997).

[74] J. I. Andrés de la Fuente, *Enhanced Modelling of LAGEOS Non-Gravitational Perturbations*, Ph.D. thesis, Delft University Press, Sieca Repro, Turbineweg 20, 2627 BP Delft, The Netherlands (2007).

[75] B. Rievers & C. Lämmerzahl, *High precision thermal modeling of complex systems with application to the flyby and Pioneer anomaly*, Annalen der Physik, 523, 439 (2011).

[76] B. Rievers, *High precision modelling of thermal perturbations with application to Pioneer 10 and Rosetta*, Ph.D. Thesis, Universität Bremen (2012).

[77] M. List, S. Bremer, B. Rievers, H. Selig, *Modelling of Solar Radiation Pressure Effects: Parameter Analysis for the MICROSCOPE Mission*, International Journal of Aerospace Engineering, 2015, 928206, (2015).

[78] Y. E. Bar-Sever, *New and improved solar radiation pressure models for GPS satellites based on flight data*, Tech. Rep. TR 80-4193 (JPL-CA, Jet Propulsion Lab., California Inst. of Technology, 1997).

[79] T. A. Springer, G. Beutler, and M. Rothacher, *A new solar radiation pressure model for GPS*, Advances in Space Research 23, 673 (1999).

[80] Y. Bar-Sever and D. Kuang, New Empirically Derived Solar Radiation Pressure Model for Global Positioning System Satellites During Eclipse Seasons, Interplanetary Network Progress Report 42-160, 1 (2005).

[81] M. Meindl, G. Beutler, D. Thaller, R. Dach, and A. Jäggi, *Geocenter coordinates estimated from GNSS data as viewed by perturbation theory*, Advances in Space Research 51, 1047 (2013).

[82] G. Bury, R. Zajdel, and K. Sośnica, *Accounting for perturbing forces acting on Galileo using a box-wing model*, GPS Solutions 23, 10.1007/s10291-019-0860-0 (2019).

[83] B. Fritsche, I. M., K. A., and et al., *Radiation pressure forces on complex spacecraft*, Tech. Rep. TN (HTG,Germany and ITAM,Russian,ESOC contract 11908/96/D/IM, 1998).

[84] H. Klinkrad and B. Fritsche, *Orbit and attitude perturbations due to aerodynamics and radiation pressure*, Tech. Rep. TN (Technical Report December, ESTEC, 1998).

[85] H. Klinkrad, C. Koeck, and P. Renard, *Precise satellite skin-force modelling by means of Monte-Carlo ray tracing*, ESA Journal 14, 409 (1990).

[86] H. Klinkrad, C. Koeck, and P. Renard, *Key features of a satellite skin force modelling technique by means of Monte-Carlo ray tracing*, Advances in Space Research 11, 147 (1991).

[87] Y. Vigue, P. A. M. Abusali, and B. E. Schutz, *Thermal force modeling for Global Positioning System using the Finite element method*, Journal of Spacecraft and Rockets 31, 855 (1994).

[88] H. F. Fliegel and T. E. Gallini, *Solar force modeling of block IIR Global Positioning System satellites*, Journal of Spacecraft and Rockets 33, 863 (1996).

[89] M. Ziebart, *Analytical SRP Model for GLONASS: Initial Results*, Tech. Rep. (Applied Geodesy Research Unit, School of Surveying, University of East London), (1998).

[90] M. Ziebart, *High precision analytical solar radiation pressure modelling for GNSS spacecraft*, Ph.D. thesis, University of East London (2001).

[91] M. Ziebart and P. Dare, *Analytical solar radiation pressure modelling for GLONASS using a pixel array*, Journal of Geodesy 75, 587 (2001).

[92] M. Ziebart, *Generalized Analytical Solar Radiation Pressure Modeling Algorithm for Spacecraft of Complex Shape*, Journal of Spacecraft and Rockets 41, 840 (2004).

[93] B. Rievers, C. Lämmerzahl, M. List, S. Bremer, and H. Dittus, *New powerful thermal modelling for highprecision gravity missions with application to Pioneer 10/11*, New Journal of Physics 11, 113032 (2009).

[94] F. Daraguna, *SOLAR RADIATION PRESSURE MODELING FOR THE QZS-1 SATELLITE* (2017).

[95] Z. Li, *Space vehicle radiation pressure modelling: A demonstration on Galileo satellites in GNSS*, Ph.D. thesis, Department of Civil, Environmental and Geomagnetic Engineering. Univ. College London (2018).

[96] Z. Li, M. Ziebart, S. Bhattarai, D. Harrison, and S. Grey, *Fast solar radiation pressure modelling with ray tracing and multiple refections*, Advances in Space Research 61, 2352 (2018).

[97] P. Delva, N. Puchades, E. Schönemann, F. Dilssner, C. Courde, S. Bertone, F. Gonzalez, A. Hees, C. Le Poncin-Lafitte, F. Meynadier, R. Prieto-Cerdeira, B. Sohet, J. Ventura-Traveset, and P.Wolf, *Gravitational redshift test using eccentric galileo satellites- Supplemental material*, Phys. Rev. Lett. 121, 231101 (2018).

[98] Felix Finke *Test of General Relativity with GALILEO Satellites*, Ph.D. thesis, Universität Bremen (2023).

[99] Biovia, dassault systémes, solidworks, version 2017, San Diego (CA): Dassault Systémes (2017).

[100] Comsol multiphysics® reference manual, version 5.5, COMSOL Multiphysics, Burlington, MA (1998-2019).

[101] D.M. Lucchesi, L. Anselmo, M. Bassan, C. Magnafico, C. Pardini, R. Peron, G. Pucacco and M. Visco *General Relativity Measurements in the Field of Earth with Laser-Ranged Satellites: State of the Art and Perspectives.* Universe, 5, 141, (2019).

[102] B. Putney, R. Kolenkiewicz, D. Smith, P. Dunn, M. H. Torrence, *Precision orbit determination at the NASA Goddard Space Flight Center*, Adv. Space Res. 10, 197 (1990).

[103] M. Soffel, S. A. Klioner, G. Petit, P. Wolf, S. M. Kopeikin, P. Bretagnon, V. A. Brumberg, N. Capitaine, T. Damour, T. Fukushima, B. Guinot, T.-Y. Huang, L. Lindegren, C. Ma, K. Nordtvedt, J. C. Ries, P. K. Seidelmann, D. Vokrouhlický, C. M. Will, and C. Xu, *The IAU 2000 Resolutions for Astrometry, Celestial Mechanics, and Metrology in the Relativistic Framework*

[104] G. Petit and B. Luzum, *IERS Conventions (2010)*, IERS Technical Note 36 (IERS, Frankfurt am Main: Verlag des Bundesamts für Kartographie und Geodäsie, 2010).

[105] C. Reigber, R. Schmidt, F. Flechtner, R. König, U. Meyer, K.-H. Neumayer, P. Schwintzer, and S. Y. Zhu, *An Earth gravity field model complete to degree and order 150 from GRACE: EIGEN-GRACE02S*, J. Geodyn. 39, 1 (2005).

[106] R. D. Ray, *A Global Ocean Tide Model From TOPEX/POSEIDON Altimetry: GOT99.2*, Technical Paper NASA/TM-1999-209478 Goddard Space Flight Center, Greenbelt, Maryland, (1999).

[107] E. M. Standish, X. X. Newhall, J. G. Williams, and W. M. Folkner, *JPL Planetary and Lunar Ephemerides*, DE403/LE403, Tech. Rep. JPL IOM 314.10-127 (1995).

[108] D. P. Rubincam, *LAGEOS orbit decay due to infrared radiation from Earth*, J.Geophys. Res. 92, 1287 (1987).

[109] D. P. Rubincam, *Yarkovsky thermal drag on LAGEOS*, J. Geophys. Res. 93, 13805 (1988).

[110] D. P. Rubincam, *Drag on the LAGEOS satellite*, J. Geophys.Res. 95, 4881 (1990).

[111] J. O. Cappellari, C. E. Velez, and A. J. Fuchs, *Mathematical theory of the Goddard trajectory determination system*, NASA STI/Recon Technical Report N 76, 24291 (1976).

[112] A. E. Hedin, *MSIS-86 thermospheric model*, J. Geophys. Res. 92, 4649 (1987).

[113] M. Visco & D. M. Lucchesi, *Comprehensive model for the spin evolution of the LAGEOS and LARES satellites*, Phys. Rev. D 98, 044034 (2018).

[114] Z. Altamimi, X. Collilieux, and L. Métivier, *ITRF2008: an improved solution of the international terrestrial reference frame*, J. Geod. 85, 457 (2011).

[115] Z. Altamimi, X. Collilieux, and L. Métivier, ITRF2014: *A new release of the International Terrestrial Reference Frame modeling nonlinear station motions*, Journal of Geophysical Research: Solid Earth 121, 6109 (2016).

[116] International Earth Rotation Service, *EOP Combined Series EOP C04*, Tech. Rep. (IERS).

[117] P. M. Mathews, T. A. Herring, and B. A. Buffett, *Modeling of nutation and precession: New nutation series for nonrigid Earth and insights into the Earth's interior*, J. Geophys. Res. 107, 2068 (2002).

[118] N. Capitaine, P. T. Wallace, and J. Chapront, *Expressions for IAU 2000 precession quantities*, Astron. Astrophys. 412, 567 (2003).

[119] K. Nordtvedt, *Equivalence Principle for Massive Bodies. II. Theory*, Phys. Rev. 169, 1017 (1968).

[120] C. M. Will, *Theoretical Frameworks for Testing Relativistic Gravity. II. Parametrized Post-Newtonian Hydrodynamics, and the Nordtvedt Effect*, Astrophys. J. 163, 611 (1971).

[121] C. M. Will & J. K. Nordtvedt, *Conservation Laws and Preferred Frames in Relativistic Gravity. I. Preferred-Frame Theories and an Extended PPN Formalism*, Astrophys. J. 177, 757 (1972).

[122] M. Visco & D. M. Lucchesi, *Review and critical analysis of mass and moments of inertia of the LAGEOS and LAGEOS II satellites for the LARASE program*, Advances in Space Research 57, 1928, (2016).

[123] C. Pardini, L. Anselmo, D. M. Lucchesi and R. Peron, *On the secular decay of the LARES semi-major axis*, Acta Astronautica 140, 469, (2017).

[124] Y. Kozai, *The motion of a close earth satellite*, Astron. J. 64, 367 (1959).

[125] D. M. Lucchesi and G. Balmino, *The LAGEOS satellites orbital residuals determination and the Lense Thirring effect measurement*, Plan. Space Sci. 54, 581 (2006).

[126] C. W. Johnson, C. A. Lundquist, and J. L. Zurasky, eds., *Anaheim International Astronautical Federation Congress* (1976)

[127] B. Jaduszliwer, J. Camparo, *Past, present and future of atomic clocks for GNSS.* GPS Solut 25, 27 (2021).

[128] F.G. Major, *The quantum beat: the physical principles of atomic clocks.* Springer, New York.

[129] D. W. Allan, *Time and Frequency (Time-Domain) Characterization, Estimation, and Prediction of Precision Clocks and Oscillators*, in IEEE Transactions on Ultrasonics, Ferroelectrics, and Frequency Control, vol. 34, no. 6, pp. 647-654, (1987).

[130] W.J. Riley *Time domain stability. Handbook of frequency stability analysis*, NIST special publication 1065. US Government Printing Office, Washington DC, pp 9–66 (2008).

[131] G. Gamow, *Expanding Universe and the Origin of Elements*, Phys. Rev. 70, 572 (1946).

[132] G. Gamow, *The Origin of Elements and the Separation of Galaxies*, Phys. Rev. 74, 505 (1948).

[133] G. Gamow, *The Evolution of the Universe*, Nature 162, 680 (1948).

[134] R. A. Alpher, H. Bethe, and G. Gamow, *The Origin of Chemical Elements*, Phys. Rev. 73, 803 (1948).

[135] R. A. Alpher and R. C. Herman, *Theory of the Origin and Relative Abundance Distribution of the Elements*, Rev. Mod. Phys. 22, 153 (1950).

[136] R. A. Alpher, J. W. Follin, and R. C. Herman, *Physical Conditions in the Initial Stages of the Expanding Universe*, Phys. Rev. 92, 1347, (1953).

[137] A. G. Riess et al. (Supernova Search Team), *Observational Evidence from Supernovae for an Accelerating Universe and a Cosmological Constant*, Astron. J. 116, 1009 (1998).

[138] S. Perlmutter et al. (Supernova Cosmology Project), *Measurements of* Ω *and* Λ *from 42 High-Redshift Supernovae*, Astrophys. J. 517, 565 (1999).

[139] S. Weinberg, *The cosmological constant problem*, Rev. Mod. Phys. 61, 1 (1989).

[140] S. M. Carroll, W. H. Press, and E. L. Turner, *The Cosmological Constant*, Ann. Rev. Astron. Astrophys. 30, 499 (1992).

[141] S. M. Carroll, *The Cosmological Constant*, Living Rev. Rel. 4, 1 (2001).

[142] T. Padmanabhan, *Cosmological Constant-the weight of the vacuum*, Phys. Rept. 380, 235 (2003).

[143] J. Martin, *Everything you always wanted to know about the cosmological constant problem (but were afraid to ask)*, Comptes Rendus Physique 13, 566 (2012).

[144] F. Zwicky, *The redshift of extragalactic nebulae*, Helv. Phys. Acta 6, 110 (1933).

[145] V. C. Rubin, W. K. Ford, Jr., and N. Thonnard, *Extended rotation curves of high-luminosity spiral galaxies. IV. Systematic dynamical properties,* $S_a \rightarrow S_c$, Astrophys. J. Lett. 225, L107 (1978).

[146] K. Freese, *Review of Observational Evidence for Dark Matter in the Universe and in upcoming searches for Dark Stars*, EAS Publ. Ser. 36, 113 (2009).

[147] S. Profumo, *An Introduction to Particle Dark Matter*, (World Scientific, 2017).

[148] L. Roszkowski, E. M. Sessolo, and S. Trojanowski, *WIMP dark matter candidates and searches—current status and future prospects*, Rept. Prog. Phys. 81, 066201 (2018).

[149] G. Bertone and D. Hooper, *History of dark matter*, Rev. Mod. Phys. 90, 045002 (2018).

[150] G. Bertone and T. Tait, *A new era in the search for dark matter*, M. P., Nature 562, 51 (2018).

[151] G. Arcadi, M. Dutra, P. Ghosh, M. Lindner, Y. Mambrini, M. Pierre, S. Profumo, and F. S. Queiroz, *The waning of the WIMP? A review of models, searches, and constraints*, Eur. Phys. J. C 78, 203 (2018).

[152] A. Arbey and F. Mahmoudi, *Dark Matter and the Early Universe: A review*, Prog. Part. Nucl. Phys. 119, 103865 (2021).

[153] S. Cebrián, *Review on dark matter searches*, J. Phys. Conf. Ser. 2502, 012004 (2023).

[154] E. Abdalla et al., *Cosmology Intertwined: A Review of the Particle Physics, Astrophysics, and Cosmology Associated with the Cosmological Tensions and Anomalies*, JHEAp 34, 49 (2022).

[155] B. Carr, F. Kuhnel, and M. Sandstad, *Primordial black holes as dark matter*, Phys. Rev. D 94, 083504 (2016).

[156] B. Carr & F. Kuhnel, *Primordial Black Holes as Dark Matter: Recent Developments*, Ann. Rev. Nucl. Part. Sci. 70, 355 (2020).

[157] B. Carr, K. Kohri, Y. Sendouda, and J. Yokoyama, *Constraints on primordial black holes*, Rept. Prog. Phys. 84, 116902 (2021).

[158] A. M. Green and B. J. Kavanagh, *Primordial black holes as a dark matter candidate*, J. Phys. G 48, 043001 (2021).

[159] D. F. J. Kimball and K. van Bibber, eds., *The Search for Ultralight Bosonic Dark Matter*, (2023).

[160] B. M. Roberts, G. Blewitt, C. Dailey, M. Murphy, M. Pospelov, A. Rollings, J. Sherman, W. Williams, A. Derevianko, *Search for domain wall dark matter with atomic clocks on board global positioning system satellites*, Nature Communications 8, 1195 (2017).

[161] T. W. B. Kibble, *Topology of cosmic domains and strings*, J. Phys. A 9, 1387 (1976).

[162] T. W. B. Kibble, *Some implications of a cosmological phase transition*, Phys. Rept. 67, 183 (1980).

[163] A. Vilenkin and E. P. S. Shellard, *Cosmic Strings and Other Topological Defects*, (Cambridge University Press, 2000).

[164] T. Vachaspati, Kinks and Domain Walls: *An Introduction to Classical and Quantum Solitons* (Oxford University Press, 2007).